Novel Materials for Nitrite Detection and Phosphate Removal

Tarawee Taweekarn

A Thesis Submitted in Fulfillment of the Requirements for the
Degree of Doctor of Philosophy in
Environmental Management Technology
(International Program)
Prince of Songkla University
2021

Novel Materials for Nitrite Detection and Phosphate Removal

Tarawee Taweekarn

A Thesis Submitted in Fulfillment of the Requirements for the

Degree of Doctor of Philosophy in

Environmental Management Technology

(International Program)

Prince of Songkla University

2021

Thesis Title   Novel Materials for Nitrite Detection and Phosphate Removal
Author   Miss Tarawee Taweekarn
Major Program   Environmental Management Technology (International Program)

Major Advisor   **Examining Committee:**

………………………………   ….....………………………….Chairperson

(Assoc. Prof. Dr. Aree Choodum)   (Assoc. Prof. Dr. Atitaya Siripinyanond)

Co-advisor

                                     ….....………………………Committee

                                       (Assoc. Prof. Dr. Aree Choodum)

………………………………….
(Assoc. Prof. Dr. Worawit Wongniramaikul)   ….....…………………………..Committee

                                       (Dr. Danai Tipmanee)

                                     ….....…………………………..Committee

                                       (Asst. Prof. Dr. Pensiri Akkajit)

                                     ….....…………………………..Committee

                                       (Assoc. Prof. Dr. Worawit Wongniramaikul)

    The Graduate School, Prince of Songkla University, has approved this thesis
as fulfillment of the requirements for the Doctor of Philosophy Degree in
Environmental Management Technology (International Program)

                            ………………………………………
                            (Prof. Dr. Damrongsak Faroongsarng)
                            Dean of Graduate School

This is to certify that the work here submitted is the result of the candidate's own investigations. Due acknowledgement has been made of any assistance received.

……………………..…..……. Signature

(Assoc. Prof. Dr. Aree Choodum)

 Major Advisor

…………………………………. Signature

(Miss Tarawee Taweekarn)

Candidate

I hereby certify that this work has not been accepted in substance for any degree and is not being currently submitted in candidature for any degree.

………………….…..……. Signature

(Miss Tarawee Taweekarn)

Candidate

ชื่อวิทยานิพนธ์	การพัฒนาวัสดุชนิดใหม่สำหรับตัวตรวจวัดไนไตรท์และกำจัดฟอสเฟต
ผู้เขียน	นางสาวธราวี ทวีกาญจน์
สาขาวิชา	เทคโนโลยีการจัดการสิ่งแวดล้อม (หลักสูตรนานาชาติ)
ปีการศึกษา	2564

บทคัดย่อ

วิทยานิพนธ์นี้มุ่งเน้นการพัฒนาวัสดุชนิดใหม่สำหรับประยุกต์ใช้งานด้านสิ่งแวดล้อม ในการวิเคราะห์ปริมาณและกำจัดธาตุอาหารในแหล่งน้ำ เพื่อเฝ้าระวังและลดการเกิดปรากฏการณ์ สาหร่ายสะพรั่ง โดยประกอบด้วยการพัฒนาเซ็นเซอร์แบบตรวจวัดสีสำหรับตรวจวัดไนไตรท์ในน้ำ และการพัฒนาวัสดุดูดซับชนิดใหม่สำหรับกำจัดฟอสเฟตในน้ำ โดยเซ็นเซอร์แบบตรวจวัดสีสำหรับ ตรวจวัดไนไตรท์พัฒนาขึ้น เนื่องจากไนไตรท์เป็นธาตุอาหารสำคัญที่เป็นตัวบ่งชี้คุณภาพน้ำซึ่งสามารถ เร่งการเกิดปรากฏการณ์สาหร่ายสะพรั่ง นำไปสู่ผลกระทบต่อระบบนิเวศทางน้ำได้เป็นอย่างมาก อีกทั้งไนไตรท์ยังก่อให้เกิดกลุ่มอาการของโรคทารกสีน้ำเงินจากการรับสัมผัสไนไตรท์ ซึ่งเป็นสภาวะ ที่ไนไตรท์รวมตัวกับฮีโมโกลบินในเม็ดเลือดแดงและเปลี่ยนเป็นเมทฮีโมโกลบิน ทำให้ความสามารถ ในการลำเลียงออกซิเจนไปยังร่างกายลดลงส่งผลให้เกิดภาวะขาดออกซิเจน นอกจากนี้ไนไตรท์ ยังสามารถทำปฏิกิริยากับสารประกอบเอมีนนำไปสู่การก่อตัวของสารไนโตรซามีน ซึ่งเป็นสารก่อ มะเร็งอีกด้วย การพัฒนาเซ็นเซอร์อาศัยหลักการเกิดปฏิกิริยาการเกิดสีระหว่างไนไตรท์กับสารเคมี ที่สามารถเกิดปฏิกิริยาเคมีอย่างจำเพาะกับไนไตรท์ ได้แก่ รีเอเจนต์เกรส ซึ่งถูกกักเก็บไว้ภายใน รูพรุนของวัสดุขนาดนาโนของเมโซพอรัสซิลิกาที่ถูกทำให้เชื่อมต่อกันเป็นแผ่นบางด้วยสารละลายแป้ง มันสำปะหลัง เซ็นเซอร์แบบตรวจวัดสีนี้สามารถมองเห็นการเปลี่ยนแปลงสีหลังเกิดปฏิกิริยาได้ด้วยตา เปล่า หรือใช้งานร่วมกับโปรแกรมวิเคราะห์ภาพสีเพื่อการวิเคราะห์ไนไตรท์เชิงปริมาณเพื่อหาค่าความ

เข้มแสงของสีพื้นฐาน 3 สี (แดง เขียว น้ำเงิน) ของผลิตภัณฑ์สีที่ได้จากปฏิกิริยาทางเคมี พบว่า ค่าความเข้มของแสงสีเขียว มีความไวในการตรวจวัดไนไตรท์สูงสุด (70 ± 2 a.u./mgL^{-1}) ซึ่งเซ็นเซอร์ ที่ถูกพัฒนาขึ้นมีลักษณะเป็นแผ่นบางมีความหนา ประมาณ 313 ไมโครเมตร จากการศึกษา พบว่า วิธีวิเคราะห์ที่พัฒนาขึ้นมีช่วงความสัมพันธ์ของค่าการตอบสนองจากการตรวจวัดและความเข้มข้นของ สารไนไตรท์เป็นเส้นตรง (Linear range) ตั้งแต่ 0.05 ถึง 2.5 มิลลิกรัมต่อลิตร ($R^2 = 0.9988$) มีขีดจำกัดของการตรวจวัด 15 ไมโครกรัมต่อลิตร ในรูปของไนไตรท์ไอออน หรือ 4.6 ไมโครกรัม ต่อลิตรในรูปไนโตรเจน ทั้งนี้ยังมีความแม่นยำในการวิเคราะห์สูง (2.67 ร้อยละค่าความคลาดเคลื่อน สัมพัทธ์, % relative error) ในขณะที่ผลการทดสอบร้อยละของการได้กลับคืนจากการวิเคราะห์ ตัวอย่างที่เติมสารมาตรฐานไนไตรท์ที่ความเข้มข้น 0.5 และ 1.0 มิลลิกรัมต่อลิตร จำนวน 3 ซ้ำ อยู่ในช่วงร้อยละ 88–114 ซึ่งเซ็นเซอร์ตรวจวัดสีที่พัฒนาขึ้นในลักษณะแผ่นบางนี้มีราคาประหยัดกว่า ชุดทดสอบไนไตรท์ที่จำหน่ายเชิงพาณิชย์ โดยมีราคาเพียง 1.25 บาท ต่อเซ็นเซอร์ การวิเคราะห์ ปริมาณของไนไตรท์ในตัวอย่างจริง จำนวน 8 ตัวอย่าง พบว่า มีความเข้มข้นของไนไตรท์ตั้งแต่ 0.04 ± 0.02 ถึง 4.52 ± 0.79 มิลลิกรัมต่อลิตร โดยผลการวิเคราะห์ที่ได้แตกต่างอย่างไม่มีนัยสำคัญทาง สถิติกับวิธีมาตรฐานที่ระดับความเชื่อมั่นร้อยละ 95 ($p > 0.05$) ในขณะที่งานวิจัยที่สองได้พัฒนา วัสดุดูดซับชนิดใหม่สำหรับกำจัดฟอสเฟตในน้ำผิวดิน เนื่องจากสารฟอสเฟตเป็นธาตุอาหารหลักอีก ชนิดหนึ่งซึ่งมีความสำคัญและเป็นสารมลพิษหลักในระบบนิเวศทางน้ำที่ส่งผลให้คุณภาพน้ำเสื่อม โทรมรวมถึงเป็นสาเหตุหลักของการเกิดสาหร่ายสะพรั่ง โดยวัสดุดูดซับชนิดใหม่อาศัยหลักการ ผสมผสานแคลเซียมซิลิเกตไฮเดรต ซึ่งมีประสิทธิภาพในการกำจัดฟอสเฟตในโครงสร้างของวัสดุ ครัยโอเจลที่สังเคราะห์จากแป้งข้าวเจ้าและแป้งมันสำปะหลังเพื่อลดการสูญหายของอนุภาคขนาด นาโนของแคลเซียมซิลิเกตไฮเดรต และทำให้การจัดการกับวัสดุดูดซับหลังการใช้งานในตัวอย่างจริง ง่าย และสะดวกมากยิ่งขึ้น โดยปริมาณแคลเซียมซิลิเกตไฮเดรตที่เหมาะสมในการเตรียมตัวดูดซับ

ผสมผสานด้วยครัยโอเจล เท่ากับร้อยละ 7.5 (ร้อยละของตัวดูดซับโดยน้ำหนัก) จากการศึกษา พบว่า วัสดุดูดซับที่พัฒนาขึ้นนี้มีประสิทธิภาพในการกำจัดฟอสเฟตมากกว่าร้อยละ 98 ในระยะเวลา 2 ชั่วโมง และมีประสิทธิภาพในการดูดซับฟอสเฟต 65.42 มิลลิกรัมฟอสเฟตต่อกรัมแคลเซียม ซิลิเกตไฮเดรต ทั้งนี้การศึกษาไอโซเทอมของการดูดซับเพื่อใช้ทำนายลักษณะการดูดซับ พบว่า ไอโซเทอมของการดูดซับสอดคล้องกับไอโซเทอมของฟรุนดิช (Freundlich isotherm) มากกว่า ไอโซเทอมของแลงเมียร์ (Langmuir isotherm) แสดงให้เห็นว่าลักษณะการดูดซับฟอสเฟตบนวัสดุ ดูดซับที่พัฒนาขึ้นเป็นการดูดซับแบบหลายชั้นหรือเป็นการดูดซับทางเคมี ในขณะที่จลพนศาสตร์ของ การดูดซับซึ่งศึกษาจากแบบจำลอง Pseudo–first order และ Pseudo–second order พบว่า สอดคล้องกับแบบจำลอง Pseudo–second order ชี้ให้เห็นว่า ขั้นตอนที่จำกัดอัตราการดูดซับของ การดูดซับฟอสเฟตเกิดจากกระบวนการดูดซับทางเคมี และจากการศึกษาเทอร์โมไดนามิกส์การดูดซับ พบว่า ค่าพลังงานกระตุ้น (Ea) มีค่ามากกว่า 40 กิโลจูลต่อโมล แสดงให้เห็นว่ากลไกการดูดซับของ วัสดุที่พัฒนาขึ้นเป็นการดูดซับทางเคมี ในขณะที่พารามิเตอร์อื่น ๆ ประกอบด้วย ค่าการเปลี่ยนแปลง เอนทาลปี ($\Delta H°$) เท่ากับ 19.3 กิโลจูลต่อโมล แสดงให้เห็นว่ากระบวนการดูดซับฟอสเฟตเป็น กระบวนการดูดความร้อน และพบว่ามีความสามารถในการลอยอยู่บนผิวน้ำได้มากถึง 105 วัน โดย ตัวดูดซับที่พัฒนาขึ้นไม่ได้รับความเสียหายในระยะเวลาดังกล่าว ทั้งนี้จากการศึกษาความสามารถใน การย่อยสลายทางชีวภาพของตัวดูดซับที่พัฒนาขึ้น พบว่า ตัวดูดซับที่พัฒนาขึ้นสามารถย่อยสลายทาง ชีวภาพด้วยวิธีการฝังดินตามวิธีมาตรฐานเกิดการย่อยสลายทางชีวภาพในระยะเวลา 10 วัน งานวิจัย ที่ถูกพัฒนาขึ้นนี้จะเป็นประโยชน์ต่อการใช้งานด้านสิ่งแวดล้อม โดยเฉพาะอย่างยิ่งในจังหวัดภูเก็ตที่มี ปริมาณสารอาหารในระบบนิเวศทางน้ำเพิ่มสูงขึ้น อันเนื่องมาจากกิจกรรมของมนุษย์ต่าง ๆ ที่นำไปสู่ การเสื่อมสภาพของระบบนิเวศและก่อให้เกิดปรากฏการณ์ยูโทรฟิเคชั่น

Thesis Title   Novel Materials for Nitrite Detection and Phosphate Removal

Author   Miss Tarawee Taweekarn

Major Program   Environmental Management Technology (International Program)

Academic Year   2021

Abstract

This thesis focuses on the development of materials for environmental applications, especially for the detection and removal of nutrients in water sample. There are two researches including the development of colorimetric sensor based on mesoporous silica nanoparticles for nitrite detection and bio–adsorbent based on calcium silicate hydrate nanoparticles composite bio–cryogel for phosphate removal. For the first part of this work, a novel colorimetric sheet based on Griess reagent–doped mesoporous silica nanoparticles was developed for nitrite detection since nitrite is an important indicator of water quality which can accelerate eutrophication and damage ecosystems. It can cause blue baby syndrome in infants and contribute to the formation of carcinogenic N–nitrosamines. Griess reagent was adsorbed on long–range ordered hexagonal mesoporous silica nanoparticles and developed ink–bottle pores with some disorder. When the modified nanoparticles were bound using starch to fabricate a thin (~313 μm) colorimetric sheet, spherical particles with a rougher surface and some distortion of their mesoporosity were observed. The sheet was used in conjunction with digital image colorimetry (DIC) to provide a wide linear range (0.05 to 2.5 mgL^{-1}) with a low nitrite detection limit (15 $μgL^{-1}$–NO_2^-, equal to 4.5 $μgL^{-1}$ NO_2^-–N), good inter–day precision (1.93 %RSD), and excellent accuracy (2.67% relative error). The colorimetric sensors produced from the sheet costs only 0.04 USD each, while the DIC uses a standard smartphone for photography. It thus offers an easier and cheaper means of conducting rapid on–site analysis of nitrite in water with reliable quantitative results. For the second part of the thesis, a novel calcium silicate hydrate composite cryogel (Cry–CSH) was successfully prepared for phosphate removal and recovery as phosphate is a major pollutant that deteriorates water quality and causes eutrophication. Calcium silicate

hydrate (C–S–H) was mixed with the gel precursor (7.5% w/w) prepared from native starch and limewater (saturated calcium hydroxide solution as the cross–linker). The mixture was frozen and thawed for 3 cycles giving an interconnected macroporous composite. This had C–S–H nanoparticles (75 mg) immobilized on a monolithic floatable cryogel network (2.5 cm diameter×1.0 cm height) enabling an easier recovery and without the losses that occur when using C–S–H nanoparticles. The phosphate adsorption reaches equilibrium at 120 min with adsorption capacity of 2.50 $mgPO_4^{3-}/g_{Cry\text{-}CSH}$ (65.42 $mgPO_4^{3-}/g_{C\text{–}S\text{–}H}$) under optimum conditions. Adsorption equilibrium data were well fit by the Freundlich isotherm model, while kinetic results were well fit by the pseudo second–order model. The calculated activation energy (E_a) of 43.9 kJ/mol indicates chemical adsorption, while a positive change in enthalpy (ΔH^0, 19.3 kJ/mol) indicates the endothermic nature of phosphate adsorption. Cry–CSH can remove phosphate from wastewater and effluent samples with excellent removal efficiency (> 98%). It can float on water surface for at least 105 days without damage, while its phosphate adsorbed form can be biodegraded within 10 days under soil buried conditions. Both colorimetric sensor and bio–adsorbent developed in this research would be benefit for environmental applications, especially for Phuket that nutrients have increased in aquatic ecosystems due to various anthropogenic activities leading to deterioration of the ecosystem and can accelerate eutrophication.

Acknowledgement

This thesis was successfully completed due to the great help and advice from many people. I wish to express my gratitude to those who have contributed.

I would like to express my sincere thanks to my advisors, Associate Professor Dr. Aree Choodum and Associate Professor Dr. Worawit Wongnilamaikul who gave me the opportunity to pursue my Ph.D. with invaluable help, guidance, advice, encouragement, suggestions and support throughout the duration of this work. Their instructions and scientific spirit will be a benefit to my future career and my whole life.

I am indebted to the members of the examination committee for giving their valuable time to consider this thesis. I gratefully acknowledge the lecturers of the faculty Technology and Environment, Prince of Songkla University, Phuket campus or imparting their knowledge which is useful for my thesis and to my future. I also would like to thank the staffs of the faculty of Technology and Environment for their help with some technical aspects of this thesis.

I also would like to thank financial support from the faculty Technology and Environment, Prince of Songkla University, Phuket campus and Graduate School, Prince of Songkla University.

Most importantly, I would like to thank my family and lovely friends for their love, encouragement and support throughout of my life, in particular: my parents for letting me choose my own ways in life.

Tarawee Taweekarn

The Relevance of the Research Work to Thailand

This thesis focuses on the development of materials for environmental applications, especially for the detection and removal of nutrients in water sample. As Phuket and many regions of Thailand are facing with the problem involving the increasing of nutrients in aquatic ecosystems due to various anthropogenic activities leading to deterioration of the ecosystem and can accelerate eutrophication, the development of colorimetric sensor for on–site detection of nitrite would thus be benefit to Thailand as such pollutant would be rapidly detected with simple and accurate colorimetric test kit. That is, anyone can apply the developed test kit for monitoring the environmental pollutant that could help the government officers to look after the environmental situation. The development of bio–adsorbent for removal of nutrients in water samples is also benefit to Thailand to reduce contaminated nutrients in water. Since bio–adsorbent developed in this work could biodegrade in soil, the nutrients adsorbed bio–adsorbent could be further used as fertilizer.

Contents

Contents (Cont.)

List of Figures

List of Figures (Cont.)

List of Figures (Cont.)

List of Tables

List of Abbreviations

Br^-	Bromide ion
Ca^{2+}	Calcium (II) ion
Cl^-	Chloride ion
CO_3^{2-}	Carbonate ion
Cry	Cryogel
Cry–CSH	Calcium silicate hydrate composite cryogel
C–S–H	Calcium silicate hydrate
CTAB	Cetyltrimethylammonium bromide
Cu^{2+}	Copper (II) ion
DIC	Digital image colorimetry
E_a	Activation energy
F^-	Fluoride ion
GMSP	Griess–adsorbed mesoporous silica particles
GMSS	Griess–adsorbed mesoporous silica sheet
IUPAC	The International Union of Pure and Applied Chemistry
LOD	Limit of detection
LOQ	Limit of quantification
Mg^{2+}	Magnesium (II) ion
Na^+	Sodium ion
NED	N–(1–naphthyl) ethylenediamine dihydrochloride
Ni^{2+}	Nickel (II) ion
NO_2^-	Nitrite ion
NO_3^-	Nitrate ion
OH^-	Hydroxide ion
Pb^{2+}	Lead (II) ion
pH_{pzc}	The point of zero charge
PO_4^{3-}	Phosphate ion

List of Abbreviations (Cont.)

SO_4^{2-}	Sulfate ion
TEOS	Tetraethyl orthosilicate
Zn^{2+}	Zinc (II) ion
ΔG^0	Gibbs free energy
ΔH^0	Enthalpy
ΔS^0	Entropy

List of Publications

Paper I   **Taweekarn, T.,** Wongniramaikul, W., Limsakul, W., Sriprom, W., Phawachalotorn C., and Choodum, A. 2020. A novel colorimetric sensor based on modified mesoporous silica nanoparticles for rapid on–site detection of nitrite. Microchimica Acta 187, 643.
(Reprinted with permission of Springer Link)

Paper II   **Taweekarn, T.,** Wongniramaikul W., and Choodum, A. 2022. Removal and recovery of phosphate using a novel calcium silicate hydrate composite starch cryogel. Journal of Environmental Management 301, 113923.
(Reprinted with permission of Elsevier)

Reprints were made with permission from the publishers

Paper I

Reprinted with permission of Springer Link

SPRINGER NATURE LICENSE

TERMS AND CONDITIONS

Jul 31, 2021

This Agreement between Prince of Songkla university -- Tarawee Taweekarn ("You") and Springer Nature ("Springer Nature") consists of your license details and the terms and conditions provided by Springer Nature and Copyright Clearance Center.

License Number	5086371162969
License date	Jun 12, 2021
Licensed Content Publisher	Springer Nature
Licensed Content Publication	Microchimica Acta
Licensed Content Title	A novel colorimetric sensor based on modified mesoporous silica nanoparticles for rapid on–site detection of nitrite
Licensed Content Author	Tarawee Taweekarn et al
Licensed Content Date	Nov 6, 2020
Type of Use	Thesis/Dissertation
Requestor type	academic/university or research institute
Format	print and electronic
Portion	full article/chapter
Will you be	no

translating?

Circulation/distribution 1 - 29

Author of this Springer

Nature content   Yes

Title   Novel material for nitrite detection and phosphate removal

Institution name   Prince of Songkla University

Expected presentation   Sep 2021
date

Requestor Location   Prince of Songkla university

                        Faculty of Technology and Environment, P

                        Kathu, Phuket 83120

                        Thailand

                        Attn: Prince of Songkla university

Total   0.00 USD

Reprints were made with permission from the publishers

Paper II

Reprinted with permission of Elsevier

CCC | RightsLink®

Home | Help ∨ | Live Chat | Sign in | Create Account

Removal and recovery of phosphate using a novel calcium silicate hydrate composite starch cryogel

Author: Tarawee Taweekarn,Worawit Wongniramaikul,Aree Choodum
Publication: Journal of Environmental Management
Publisher: Elsevier
Date: 1 January 2022

© 2021 Elsevier Ltd. All rights reserved.

Journal Author Rights

BACK

CLOSE WINDOW

ELSEVIER

Dear Dr Taweekarn,

Thank you for publishing your article in Journal of Environmental Management . Assoc.Pro... Choodum completed the Rights and Access Form for your article *Removal and recovery of phosphate using a novel calcium silicate hydrate composite starch cryogel* on October 08, 2021.

The Order Summary is attached to this email. A copy of the Order Summary is also sent to all co-authors for whom we have contact details.

If you have any questions, please do not hesitate to contact us. To help us assist you, please quote our article reference YJEMA_113923 in all correspondence.

Now that your article has been accepted, you will want to maximize the impact of your work. Elsevier facilitates and encourages authors to share their article responsibly. To learn about the many ways in which you can share your article whilst respecting copyright, visit: www.elsevier.com/sharing-articles.

Kind regards,
Elsevier Researcher Support

Seven strategies for you to create a brand and promote your research

Learn how to give your research the visibility it deserves with these seven strategies.

> **Access module now**

1. Introduction

1.1 Background and rationale

Water pollution issues are a major challenge that humanity is currently facing. It is the release of substances, e.g., chemicals, nutrients, microorganisms, into body of water leading to unsafe of water for human use and disrupts aquatic ecosystems. Nutrients are the most important chemical elements commonly found in water and the overabundance of them can have many harmful health and environmental effects. Nitrogen and phosphorus are two of the most important and abundant nutrients in water which occur naturally in soil and water, but most of them come from human activities, e.g., fertilizers, wastewater, automobile exhaust, animal waste. Since nitrogen and phosphorus are essential elements for life processes in water bodies, high loads can lead to increased primary production of biomass, oxygen depletion, and toxic algal blooms, namely eutrophication (Almanassra et al., 2020). Eutrophication is a serious environmental problem that has received substantial attention from the scientific community. It can cause the death of mollusks, fish, and other aquatic ecosystem inhabitants (Almanassra et al., 2020; Huong et al., 2019; Seliem et al., 2016). The algal growth in streams and rivers can cause blockages of water pipelines and turbines (Almanassra et al., 2021; Huong et al., 2019), while the presence of toxic red algae and dinoflagellates on the seashore can cause loss of income and economic disruptions (Almanassra et al., 2021; Huong et al., 2019) as well as affect human health (Almanassra et al., 2021).

Nitrogen nutrient is commonly applied for lawn and garden care and crop production. Bacteria convert various forms of nitrogen in the soil to nitrate (NO_3^-) that is absorbed by plants and is converted to organic nitrogen. When organic nitrogen decomposes, it is converted to ammonia–N and then oxidized to nitrite–nitrogen and ultimately nitrate–nitrogen. Nitrite (NO_2^-), a natural nutrient ion is a part of the nitrogen cycle, is derived from the degradation of organic compounds containing nitrogen, such as plant and animal proteins, and plays an important role in

the ecosystem. The concentration of nitrite is an important indicator of water quality and it is generally found in surface water at a low concentration (0.07 mg L^{-1} NO_2^-–N) because it is easily oxidized to nitrate. However, human activities, e.g., the use of synthetic fertilizers in agriculture and the discharge of chemical fertilizer or industrial waste, may increase the contamination of nitrite in water (Indyk and Woollard, 2011). Nitrite is thus dangerous as it can cause methemoglobinemia in aquatic animals (Jensen, 2003) and blue baby syndrome in infants (Bartsch, 1991; Hegesh and Shiloah, 1982; Knobeloch et al., 2000; Lundberg et al., 2004). Further, nitrite can also react with secondary and tertiary amines in the stomach causing carcinogenic N–nitrosamines (Honikel, 2008; Suzuki et al., 2003). Therefore, determination of the presence of nitrite is very important for both environmental protection and public health.

Phosphorus is one of the most essential nutrients and contributes to agricultural and industrial development. However, it may cause water pollution due to the continuous discharge of related pollutants into aquatic environment, leading to the deterioration in the quality of water resources. Phosphates are the most common form of phosphorus nutrients and is considered a major pollutant that deteriorates water quality. Orthophosphates are the most stable kind of phosphates which can exist in variety of species like orthophosphate/phosphate (PO_4^{3-}), hydrogen phosphate (HPO_4^{2-}), dihydrogen phosphate ($H_2PO_4^-$) and phosphoric acid (H_3PO_4) based on different pH values (Rout et al., 2021). Phosphate at concentrations between 25 μgL^{-1} and 0.03 mgL^{-1} (Almanassra et al., 2020) or above 0.02 mgL^{-1} (Seliem et al., 2016) can cause eutrophication leading to loss of income and economic disruptions (Almanassra et al., 2021; Huong et al., 2019) as well as affect human health (Almanassra et al., 2021).

Therefore, the monitoring of nutrient contamination in water is very important. In addition, the removal of these pollutants may require to maintain their concentrations at a low level in water to mitigate and control eutrophication. In the first part of this work, a novel colorimetric sheet based on Griess reagent–doped mesoporous silica was thus developed for nitrite detection. Whereas, a novel starch based monolithic cryogel was composited with calcium silicate hydrate to develop

a floatable bio–adsorbent for phosphate removal and recovery in the second part of the work.

1.2 Objective

This thesis aimed to develop novel materials for environmental applications, especially for the detection and removal of nutrients in water sample. A simple colorimetric sensor based on nanoparticle materials was developed for rapid on–site detection of nitrite for the first part of the work, while calcium silicate hydrate (CSH) was composited with starch cryogel to develop floatable bio–adsorbent for phosphate removal.

2. Result and discussion

2.1 Development of colorimetric sensor for nitrite detection.

Although accurate results for the analysis of nitrite have been reported using instrumental methods, including ion chromatography (IC) (Butt et al., 2001), capillary electrophoresis (CE) (Ishio et al., 2002), chemiluminescence (Lin et al., 2011), and high–performance liquid chromatography (HPLC) (Kodamatani et al., 2009), these methods required expert and complicated sample preparation procedures for analysis (Wang et al., 2017) and also suffer from not being suitable for on–site application. A number of researchers have thus attempted to develop colorimetric sensors to facilitate on–site determination of nitrite. Griess assay seems to be the most widely used colorimetric method in the determination of nitrite as summarized in some reviews (Singh et al., 2019; Tsikas, 2007; Wang et al., 2017) due to its low cost, high sensitivity, high stability and robust performance (Beaton et al., 2011; Choodum et al., 2015). This assay is based on a diazotization reaction of nitrite with sulfanilamide in acidic conditions to produce diazonium cations, which are further

reacted with the aromatic amine, N–(1–naphthyl) ethylenediamine dihydrochloride (NED), giving azo dye products.

In this work, a novel colorimetric sheet based on Griess reagent–doped mesoporous silica was developed for nitrite detection to avoid the use of liquid reagents, making on–site analysis easier and safer. Mesoporous silica is a porous nanomaterial with a pore size in the range of 2–50 nm (Fotoohi et al., 2018). Due to its unique physiochemical properties, i.e., it has a large specific surface area and pore volume, and is highly porous, chemically inert and functionalizable, with tunable pore and particle sizes (Diagboya and Dikio, 2018; Hoang Thi et al., 2019; Jaroniec, 2006; Wang et al., 2015), it has been applied in various roles, including biomedical (Hoang Thi et al., 2019) and environmental (Da'na, 2017; Jaroniec, 2006) applications, and drug delivery (Wang et al., 2015). Because of the highly porosity of mesoporous silica, it is possible to adsorb Griess reagent and use it as a colorimetric sensor for the detection of nitrite in water. The colorimetric sensor developed in this work was used in conjunction with digital image colorimetry (DIC) rather than spectrophotometry to facilitate rapid on–site quantitative analysis. During imaging with a digital camera, the light reflected by the colorimetric product obtained from the colorimetric sensor passes through an RGB filter and splits into three components (i.e., 400–500, 500–580, and 580–700 nm for the blue, green, and red filter, respectively) (Choodum et al., 2013). The separated wavelengths are then detected and recorded on an image sensor located behind each filter and the final color of the digital image is composed from the combined data from the three RGB filters. When the digital image is analyzed by a color analysis program, the individual RGB data recorded are obtained, representing the total photons in each region of the spectrum and can be used as analytical data for quantification.

2.1.1 Preparation and characterization of silica nanoparticles

Mesoporous silica nanoparticles were synthesized by the sol–gel method (Boos et al., 2002; Vazquez et al., 2017) using TEOS as a silica precursor in alcohol solution (ethanol) under basic conditions (NaOH) in the presence of a surfactant (CTAB). CTAB surfactant (1.64 g) was added to sodium hydroxide

solution (0.1 M, 60 mL) under stirring and heated at 60°C for 1 h. After cooling to room temperature, ethanol (13.20 mL) was then added into the solution. Alkoxide precursor, TEOS (5.56 mL), was then added causing the solution to immediately become opaque with the start of the reaction. The solution was further stirred for 24 h allowing the reaction to be completed. The resulting white precipitate was then filtered, washed with ultrapure water, and dried at 110°C overnight. The particles were then calcined at 550°C for 10 h and stored in a desiccator prior to use.

The results from BET analysis using surface area and porosity analyzer (ASAP2460, Micromeritics) showed that the nanoparticles prepared had an average pore size of 2.8 nm with a multipoint specific surface area of 1208 m^2g^{-1} and a pore volume of 0.84 mLg^{-1}. These were very similar to those reported in previous work as having been synthesized using a similar procedure with a surface area of 1200 m^2g^{-1} with a 2.4 nm pore diameter (Boos et al., 2002). In addition, the nanoparticles exhibited a typical type IV adsorption isotherm (Fig. 1a) corresponding to those in previous reports (Boos et al., 2002; Shin et al., 2018; Vazquez et al., 2017; Wei et al., 2013) where the capillary condensation of N_2 within a pore occurred above P/P_0 = 0.3 indicating the presence of ordered hexagonal mesopores (Vazquez et al., 2017; Wei et al., 2013). A parallel H4 hysteresis loop indicated a narrow slit–like pore or hollow spheres with walls composed of ordered mesoporous silica. Moreover, the narrow pore size distribution (Fig. 1b) indicated a significant presence of mesopores with a homogeneous pore size (Shin et al., 2018; Vazquez et al., 2017; Wei et al., 2013) of about 2.44 nm similar to those in a previous report (i.e., 2–3 nm) (Vazquez et al., 2017).
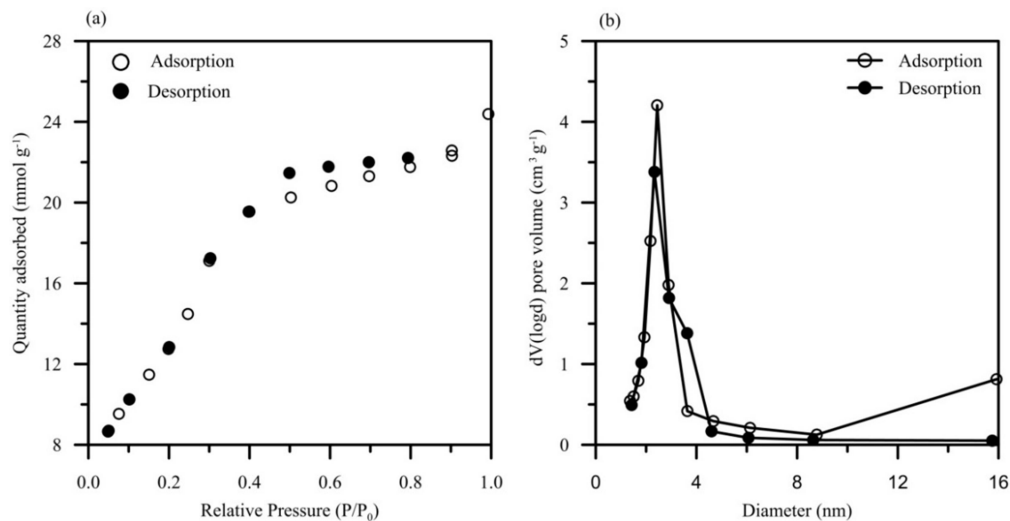
Figure 1   (a) The BJH nitrogen adsorption/desorption isotherm (b) the BJH pore size distribution of prepared silica nanoparticles.

The FESEM images from a field emission scanning electron microscope (FESEM, Apreo, FEI) of the prepared silica nanoparticles showed an agglomeration of spherical nanoparticles with a rough external surface (Fig. 2a). In order to characterize them in more detail, the silica nanoparticles were imaged by TEM as shown in Fig. 3. The micrograph confirmed their spherical shape and demonstrated a variety of particle sizes between 200 and 600 nm (Fig 3a). At high magnification (Fig. 3b) the TEM image also confirmed the presence of a hexagonal array and ordered mesopores with a honeycomb structure.
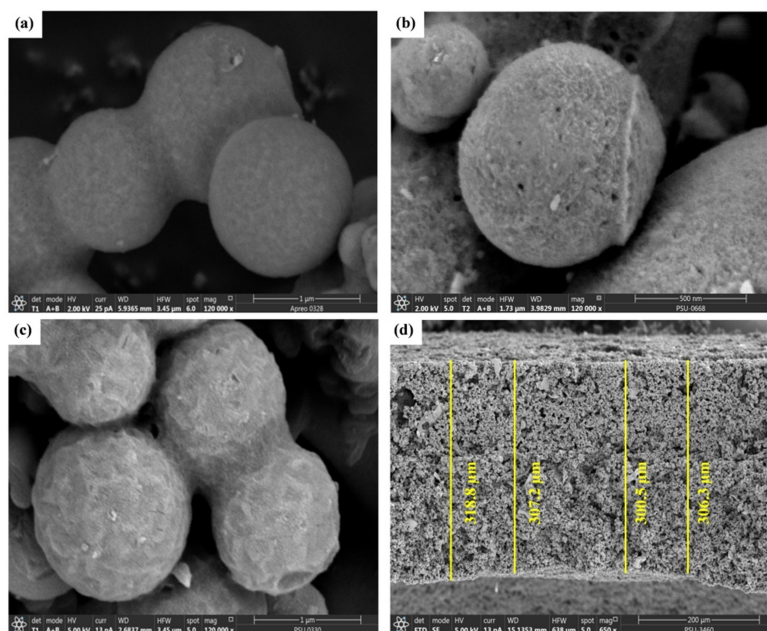
Figure 2 FESEM images of prepared silica nanoparticles (a), GMSP (b), GMSS (c), and crosssection (d) of GMSS showing the thickness of the sheet.
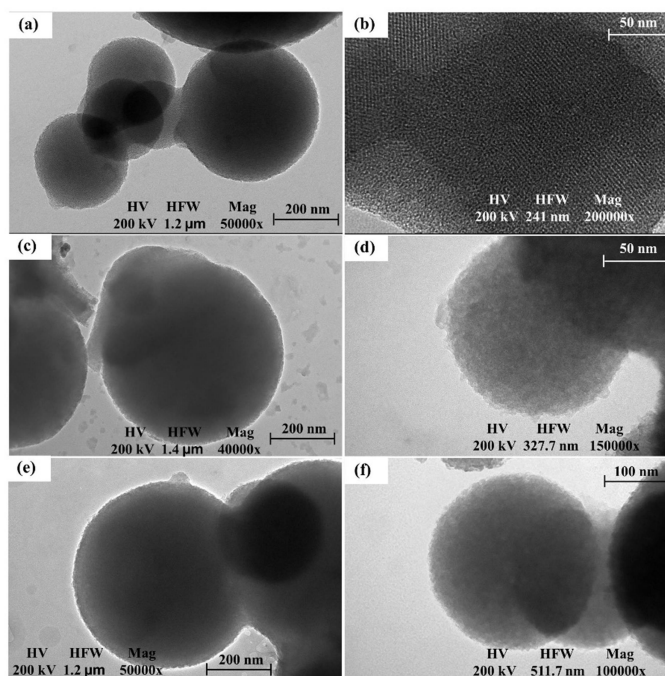
Figure 3 TEM images of prepared silica nanoparticles (a, b), GMSP (c, d), and GMSS (e, f).

In addition, the porous structure of the prepared particles was investigated using XRD (X–ray Diffractometer (Empyrene, PANalytical). The powder's XRD pattern (Fig. 4a) revealed diffraction peaks in lower 2Θ angles indicating the hexagonal structure (Ferreira Soares et al., 2015; Wei et al., 2013; Zhang et al., 2015). Absorption peaks were observed at 2Θ values of 0.60º, 1.80º, and 4.58º (broad peak) with d–spacing of 17.1, 5.29, and 1.96 nm, respectively, which could be indexed to the (100), (110), and (200) planes of the porous structure, respectively, indicating the long–range order of the hexagonal structure (Ferreira Soares et al., 2015; Wei et al., 2013; Zhang et al., 2015).
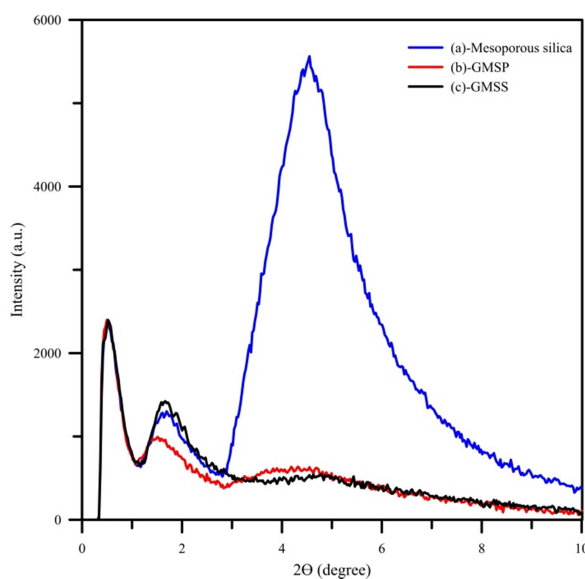
Figure 4   XRD patterns of mesoporous silica nanoparticles, GMSP, and GMSS.

The FTIR spectrum using Fourier transform infrared spectrophotometer (FTIR, Vertex70, Bruker) was used to investigate their functional groups using the KBr pellet method of the prepared silica nanoparticles as shown in Fig. 5a. The large absorption band at 3454 cm^{-1} was attributed to the stretching vibration of the O–H groups of mesoporous silica (Kachbouri et al., 2018), while the small peaks at 2925, 2854, 1462 cm^{-1} were associated with symmetrical and asymmetrical stretching of the CH_2, CH_3, CH_3–(N^+) groups, respectively, of CTAB residues (Boos et al., 2002; Silva et al., 2019). An intense band of asymmetric Si–O–Si stretching was observed at

1085 cm^{-1}, while the peaks at 969 cm^{-1} and 800 cm^{-1} corresponded to the vibration of free Si–OH and Si–O–Si bending, respectively (Boos et al., 2002; Kachbouri et al., 2018; Khan et al., 2020; Nakanishi et al., 2015). Finally, the band at 1637 cm^{-1} was attributed to the bending vibration of O–H groups from water molecules physically absorbed in the silica (Khan et al., 2020).
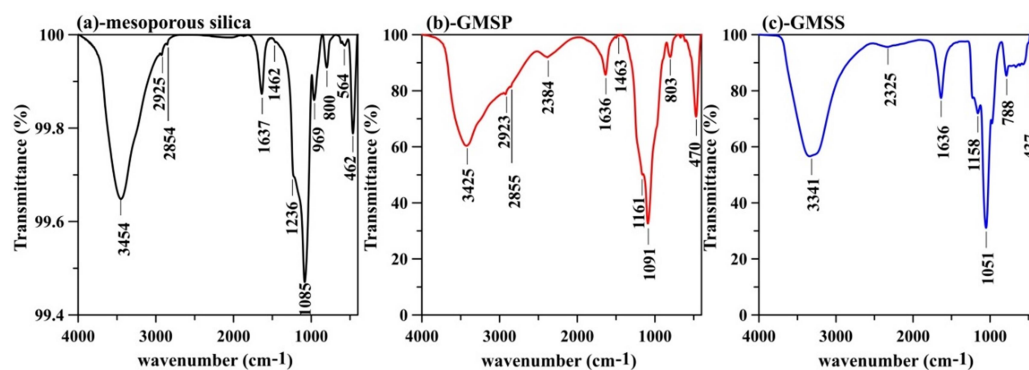
Figure 5 FTIR spectra of prepared silica nanoparticles (a), GMSP (b), and GMSS (c).

2.1.2 Preparation, optimization and characterization of colorimetric sensor

Preparation colorimetric sensor developed in this study was based on the adsorption of Griess reagent on mesoporous silica nanoparticles. The ingredients for fabricating the nitrite sensor were optimized to obtain the formulation that produced the darkest color product from nitrite using the least amount of chemicals. The Griess–adsorbed silica can be used as a colorimetric sensor, in the form of both particles (Griess–adsorbed mesoporous silica particles: GMSP) and as a thin sheet (Griess–adsorbed mesoporous silica sheet: GMSS).

The GMSP were prepared by the adsorption of Griess reagent onto mesoporous silica nanoparticles. The GMSP preparation was optimized by formulating the Griess reagent that could be adsorbed onto the silica nanoparticles and produce the darkest color product when exposed to nitrite, using the least possible amount of chemicals. To that end, the amount of sulfanilamide used in formulating

the Griess reagent was varied between 50 and 500 mg, the amount of NED was varied between 5 and 50 mg, and the volume of   85% phosphoric acid was varied between 1.0–2.0 mL. Increasing the amount of sulfanilamide from 50 to 500 mg produced nanoparticles that provided a slightly darker red–violet product on exposure to nitrite, resulting in slightly decreased image intensities (Fig. 6a), thus 200 mg sulfanilamide was chosen as the optimum value. Meanwhile, increasing the amount of NED from 5 to 10 mg produced nanoparticles that provided a darker, less intense product but the intensity was constant with further increases in the NED content between 20 to 50 mg (Fig. 6b). This indicated that 10 mg NED was sufficient to detect a nitrite solution with a concentration of 1 mgL^{-1}. Decreased intensity was observed with increases in the volume of phosphoric acid from 1.0 to 1.25 mL but thereafter, the intensity increased only slightly with further increases in the volume of phosphoric acid from 1.5 to 2.0 mL (Fig. 6c). Therefore, the optimum formulation for the Griess reagent was determined to be 200 mg sulfanilamide, 10 mg NED, and 1.25 mL 85% phosphoric acid in 10 mL ultrapure water. A 10 mL volume of the reagent was mixed with 0.5 g of the mesoporous silica nanoparticles and stirred for 2 h to allow complete adsorption by the nanoparticles which were then filtered out using a vacuum pump to obtain white nanoparticles of GMSP.
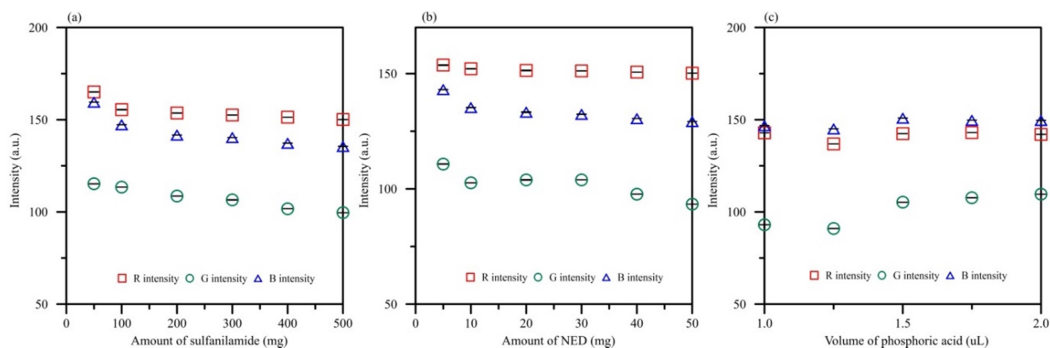
Figure 6　The influence of (a) amount of sulfanilamide (b) amount of NED (c) volume of phosphoric acid on RGB intensities of color product.

The results from BET analysis of the GMSP showed an obvious reduction in the specific surface area to 137 m^2g^{-1} with a lower pore volume of 0.20 mLg^{-1} due to the adsorption of Griess reagent on the surface of the mesoporous silica, which favored pores with a small size. This led to an increase in the average pore size to 5.9 nm compared to 2.4 nm in the parent silica. However, it is to be noted that the temperature used to degas the GMSP before analysis (105°C for 24 h) was less than that used in the parent silica (250°C for 20 h) which may have contributed to physical adsorption of stranger on the GMSP pores. The GMSP exhibited a typical type IV adsorption isotherm of N_2, indicating the remaining of mesopores from the parent silica. However, it revealed a parallel H2 hysteresis loop (Fig. 7a) instead of an H4 hysteresis loop as observed in the parent silica, indicating ink–bottle pores (a pore mouth smaller than the pore body) (Sing and Williams, 2004; Thommes et al., 2006). This result suggested that the Griess reagent was absorbed at the mouth of the silica mesopore. The pore size distribution (Fig. 7b) displayed pores of 1.5, 1.7, 2.9, 3.4, and 5.4 nm implying that the GMSP have a polymodal nanostructure, mainly due to their disordered mesoporous structure (Li et al., 2006). Spherical particles of size 400–1000 nm were observed in the GMSP with a rougher external surface area than that of the parent silica (Fig. 2b). TEM micrographs confirmed that GMSP maintained its spherical shape but the particles were larger at around 800 nm (Fig. 3c), however the ordered structure of the parent silica seemed to be changed by the adsorption of the Griess reagent (Fig. 3d). The strong peak in diffraction intensity observed at 4.58° in the parent silica also clearly reduced, indicating some extent of disorder, although the diffraction peaks of (100) and (110) were still present at 0.51° and 1.42°, respectively (Fig. 4b). This confirmed that the GMSP preserved its mesoporous structural order after the adsorption of Griess reagent, but some disorder also occurred (Taqanaki et al., 2019; Zhang et al., 2015).
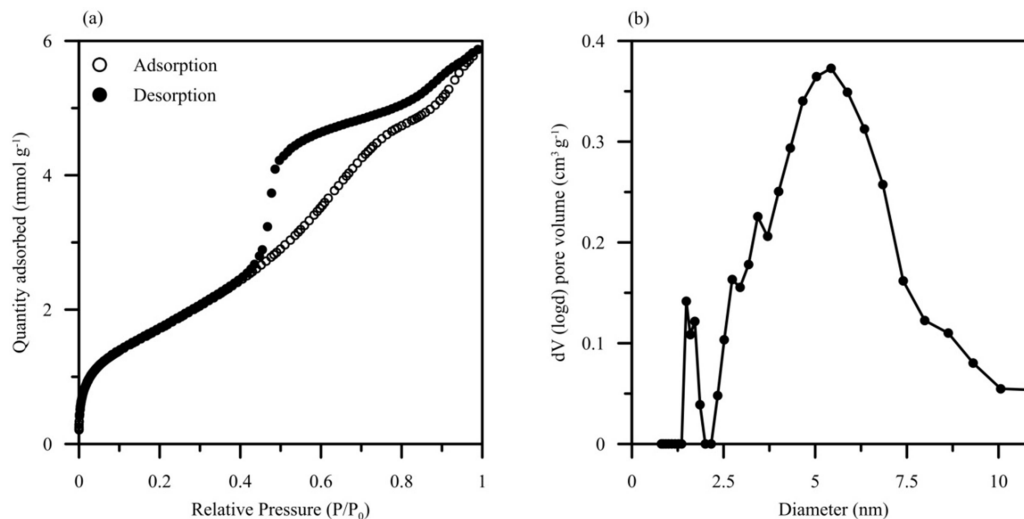
Figure 7 (a) The BJH nitrogen adsorption isotherm (b) pore size distribution of GMSP using the non–local density functional theory (NLDFT) model.

The FTIR spectra of the GMSP showed a shift in the absorption band at 3454 cm^{-1} in the parent silica to 3425 cm^{-1} and it became broader after the adsorption of Griess reagent (Fig. 5b). The O–H groups of the parent silica (Kachbouri et al., 2018) may overlap with the O–H from the phosphoric acid and N–H group from the NED and sulfanilamide (Lahtinen et al., 2014). The small peaks at 2923, 2855, 1463 cm^{-1} of the CTAB residues from the mesoporous silica (Boos et al., 2002; Silva et al., 2019) remained in their positions. Although the vibration band of O–H bending from water molecules which was present in the parent silica at 1637 cm^{-1} (Ls, 2019) seemed to remain in the same position, it may overlap with the C=O stretching (Lahtinen et al., 2014) or NH_2 scissoring (Topacli and Kesimli, 2001b) of the sulfanilamide. Similarly, the intense band of Si–O–Si and Si–OH vibration observed in the parent silica at 1085 cm^{-1} and 969 cm^{-1} (Boos et al., 2002; Kachbouri et al., 2018; Khan et al., 2020; Ls, 2019) may overlap with the SO_2 symmetric stretching of the sulfanilamide (which commonly appears at 1150 ± 15 cm^{-1}) (Topacli and Kesimli, 2001b) and was observed at 1091 and 1161 cm^{-1} in the GMSP. Finally, a band observed at 2384 cm^{-1} was associated with the vibration of the NED functional groups. The GMSS was prepared by binding the GMSP with starch in the presence of acetone. The starch solution was prepared by

gelatinizing cassava starch (1% w/v) in ultrapure water at 90°C under continuous stirring until a clear viscous solution was obtained. Then 0.50g of GMSP was mixed with the starch solution (5 mL) under magnetic stirring to ensure a homogeneous distribution before the addition of acetone solution (2 mL), and the mixture was further stirred for 3–5 min. The slurry (100 μL) was then deposited on the flat cap of a 1.5 mL centrifuge tube and incubated at 100°C for 15 min. After cooling to room temperature, the sensors were immediately vacuum sealed in packs of three in an opaque foil bag and stored in a refrigerator for further use.

Increasing the concentration of starch solution from 1−5% w/v provided a paler red−violet product resulting in an increase in intensity (Fig. 8a). Because a constant volume of 100 μL of the GMSS and starch mixture were used to fabricate the thin film, when the concentration of the starch was increased, the amount of GMSP in the slurry decreased and so reduced the red−violet product. Therefore, a starch solution of 1% w/v was selected as the binder. Similar results were obtained by increasing the amount of the starch solution from 1−5 mL with a paler red−violet product being obtained resulting in increased intensity (Fig. 8b). However, the use of a lower amount of binder made the film more brittle and 5 mL was the lowest volume of starch with which the colorimetric film could be fabricated. Therefore, 0.50 g of the GMSP was homogeneously mixed with 5 mL starch solution (1% w/v) under magnetic stirring before the addition of the acetone solution. The slurry (100 μL) was then deposited on the flat lid of a centrifuge tube and incubated at 100°C for 15 min, to produce a white sheet of GMSS with a thickness of 313 μm (Fig. 2d).
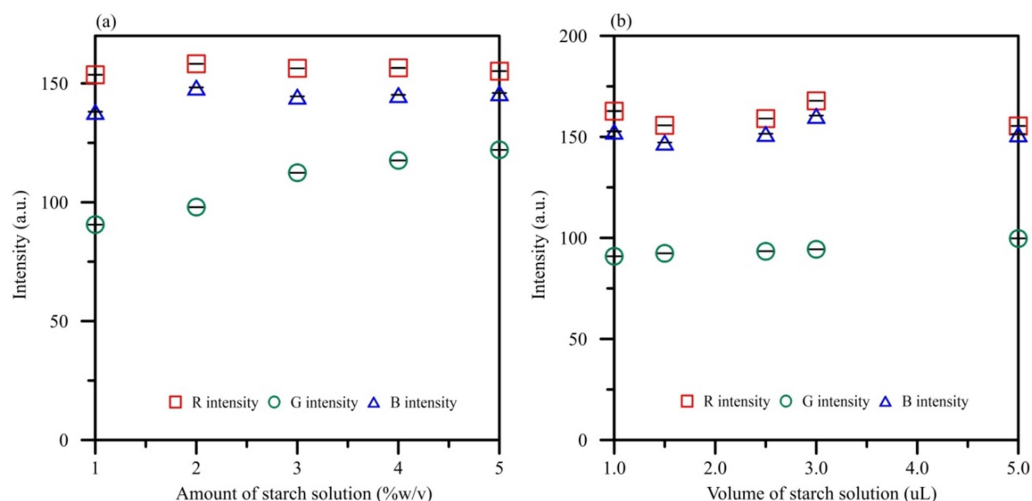
Figure 8 The influence of (a) amount of starch (b) volume of starch on RGB intensities of color product.

The results from the BET analysis of the GMSS showed a lower pore volume of 0.15 mLg^{-1} than the GMSP, as well as the parent silica, due to the binding of the GMSP in a starch film, indicating that the starch may fill the pores of the GMSP. Its specific surface area (168 m^{2}g^{-1}) was less than that of the parent silica (1200 m^{2}g^{-1}), but was slightly higher than that of the GMSP (137 m^{2}g^{-1}). The average pore size of the GMSS (3.7 nm) was bigger than that of the parent silica (2.8 nm), but smaller than that of the GMSP (5.9 nm). It seems that some of the Griess reagent adsorbed on the small pores of the silica in the GMSP may desorb and dissolve in the starch solution before coating the silica particles of the GMSS as a thin film, resulting in a decrease in the average pore size of the GMSS compared to the GMSP. This result corresponded to the maintenance of a type IV adsorption isotherm of N$_2$ on the GMSS with a parallel H4 hysteresis loop (Fig. 9a) as in the parent silica. The pore size distribution of GMSS (Fig. 9b) was narrower than that of GMSP but continued to show a polymodal nanostructure, indicating a disordered mesoporous structure (Li et al., 2006).
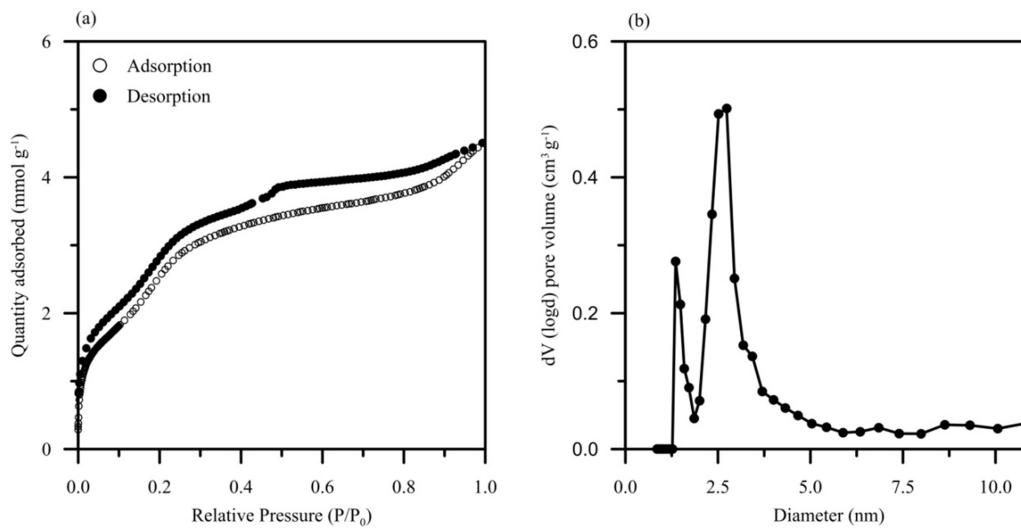
Figure 9　(a) The nitrogen adsorption isotherm (b) pore size distribution of GMSS using the NLDFT model.

The FESEM images of the GMSS showed rougher particles than the GMSP and parent silica, while the particles spherical shapes could still be observed with a size of ~1 μm (Fig. 2c). The TEM micrographs also confirmed the spherical shape of the particles in the GMSS (Fig. 3e) with some distortion of its mesoporosity similar to that of the GMSP (Fig. 3f). The XRD pattern of the GMSS at a low angle was also similar to that of the GMSP (Fig. 4c) confirming its mesoporous silica characteristic with some disorder.

The presence of starch in the GMSS made a large absorption band of O–H stretching at 3425 cm^{-1} in the GMSP become broader and shifted toward a lower frequency (3341 cm^{-1}; Fig. 5c), while it commonly present at 3280 cm^{-1} in starch (Boonkanon et al., 2020). The band of NED functional groups observed at 2384 cm^{-1} in the GMSP had shifted to 2325 cm^{-1} in the GMSS. The intense band of Si–O–Si stretching observed at 1085 cm^{-1} in the silica, which shifted to 1091 cm^{-1} in the GMSP may overlap with the C–O vibration peaks of amylopectin in the starch and had shifted to 1051 cm^{-1} in the GMSS. The SO$_2$ of the sulfanilamide (Topacli and Kesimli, 2001a) present at 1161 cm^{-1} in the GMSP remained in a similar position at 1158 cm^{-1} in the GMSS.

2.1.3 Colorimetric test and DIC for quantification of nitrite

The colorimetric tests of nitrite using GMSP and GMSS were conducted using sodium nitrite as a nitrite standard. A stock solution (100 mgL^{-1}) was prepared by dissolving sodium nitrite in ultrapure water, which was further diluted with ultrapure water to appropriate concentrations (0–1 mgL^{-1}) as standard working solutions. For testing, the GMSP were directly added into the standard solution in a vial (2 mL), while 100 µL of standard solution was dropped on the GMSS and left for an appropriate time to allow the diazotization reaction to take place. Three replications were conducted at each nitrite concentration.

The colorimetric test of the GMSP with nitrite standard solution provided a red–violet product (Fig. 10a) based on the reaction of the Griess reagent adsorbed on the mesoporous silica and the nitrite ions in the sample solutions. Those ions reacted with the sulfanilamide in the acidic conditions, forming diazonium cations, which then reacted with NED to form azo dye (Choodum et al., 2015; Tsikas, 2005). This product occurred within the layers of GMSP at a high concentration of nitrite (> 25 mgL^{-1}), but dissolved out into the solution at a low concentration. This contributed to a gradient concentration and size of the nitrite molecules. The diffusion flux of the nitrite ions from their solution into the GMSP at a high concentration was faster than at a low concentration causing the amount of Griess reagent at a high concentration of nitrite to rapidly reduce when the colorimetric reaction occurred. This caused the concentration gradient of the Griess reagent on the GMSP to be very low, leading to less diffusion to the solution. The colorimetric product thus occurred on the GMSP only. In contrast with a low concentration of nitrite a slower diffusion flux of nitrite occurred, and some of the Griess reagent desorbed from the silica particles and reacted with the nitrite in the solution. However, the red−violet product at a low concentration of 0.25 mgL^{-1}–NO$_2^-$ (0.08 mgL^{-1} NO$_2^-$−N) could be clearly observed with the naked eye, indicating good sensitivity for nitrite detection by the GMSP.
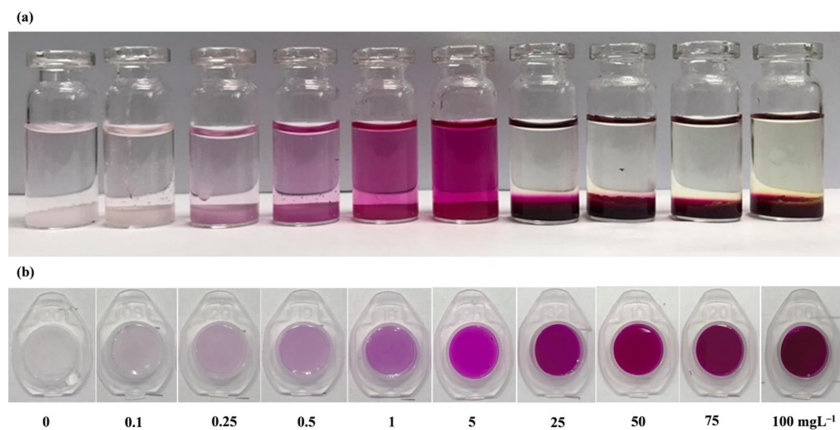
Figure 10 The colorimetric products of (a) GMSP and (b) GMSS from testing with nitrite at various concentrations.

A darker product was also obtained with increasing concentration of nitrite (Fig. 10b) for GMSS. A red–violet product occurred immediately after testing which reached equilibrium after 3 min (Fig. 11a). This was more rapid than the EPA 1686 standard method based on the same reaction (10 min) (WHO,2011) and a previous study based on a nitrosation reaction (30 min) (Aydın et al., 2005).
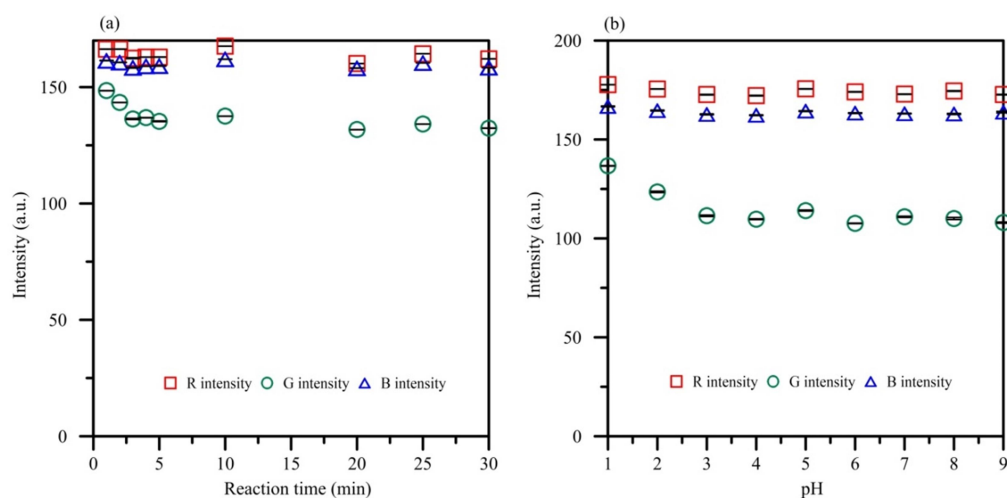
Figure 11 The influence of (a) reaction time (b) pH of nitrite ions on RGB intensities of color product by GMSS sensor.

The influence of pH on the intensities of the colorimetric product was also investigated, since acidic conditions were required for the Griess reaction. Standard solutions of sodium nitrite (1 mgL^{-1}) with pH levels adjusted to between 1 and 9 were tested with the GMSS. The results showed that the intensity of the green light from the digital image of the red–violet product decreased with pH levels of 1 to 3 and thereafter became constant (Fig. 11b), indicating that the reaction is able to occur effectively when the pH of the solution has a pH in the range of 3 to 9. Since the EPA standard method (Topacli and Kesimli, 2001b) recommends a pH of 5 to 9 for the analysis of nitrite, pH 6 was selected in the analysis of nitrite in the sample of seawater, which commonly has a pH of 6 to 7. When the standard or sample adjusted to pH 6 was dropped on the GMSS, the pH reduced to 2 as the GMSS contained phosphoric acid and the reaction thus occurred in acidic conditions. This corresponded to a previous work in which the reaction of a Griess–modified polyethylene glycol hydrogel occurred at pH 2 (Nam et al., 2018).

The GMSS was used to evaluate the performance in quantifying nitrite since it requires only 100 µL of the sample or standard compared to GMSP which requires 2 mL. The DIC was applied after colorimetric testing for quantitative analysis. A custom–built RGB photographic box (8.5×9.5×6.25 inch) modified from previous work (Choodum et al., 2017) was used to eliminate any effects of environmental light. Three GMSS sensors were placed in sample holders inside the box, while an iPhone 7.0 was then positioned above an opening on the top of the box. Six images of the colorimetric products were then taken using the digital camera of the iPhone (12MP, backside illuminated CMOS). The aperture, illumination, and photo settings were fixed as follows: f/1.8 aperture, 1/18 s exposure time, ISO 20, flash off, automatic white balance, HDR off, to achieve reproducible results. The images were saved as JPEG files (24–bits, 1.31 MB, 3024×4032 pixels) to the iPhone's memory before being transfer to a computer for color analysis. A custom–built RGB analysis program (Boonkanon et al., 2020; Choodum et al., 2016; Choodum et al., 2017) was then used to analyze the average intensities of the RGB values of the color products from the six images from each of the three sensors used as a single data point for each standard concentration, from which calibration curves were established.

The relationship between the RGB intensities, IR, IG, IB, and concentrations of nitrite between 0 and 100 mgL^{-1} are shown in Fig. 12a. The results showed that the intensities of IR and IB were higher than that of IG, indicating the appearance of the red–violet product which reflects red and blue light while absorbing green light (500–580 nm). This result corresponded to the spectrophotometric results in which the maximum absorption of the red–violet product was obtained at 543 nm, while the literature has variously reported absorption at 540 nm (Wang et al., 2017), 543 nm (Pasquali et al., 2010), and 548 nm (Nam et al., 2018). The RGB intensities decreased when the concentration of nitrite was increased because darker products were obtained at higher concentrations. The change in IG was much higher than those in IB and IR indicating that most of the green light was absorbed, resulting in the red–violet product. The linear portion of IG and IB observed in the range of 0.05 to 1.0 mgL^{-1} could be applied in the quantitative analysis of nitrite although the use of IG is recommended as higher sensitivity was obtained. The relationship between IG /ITotal (IR+IG+IB) and the concentration of nitrite was also investigated to minimize the influence of the imaging conditions (Li et al., 2016) and a wider linear range of 0.05 to 2.5 mgL^{-1} was observed (Fig. 12b).
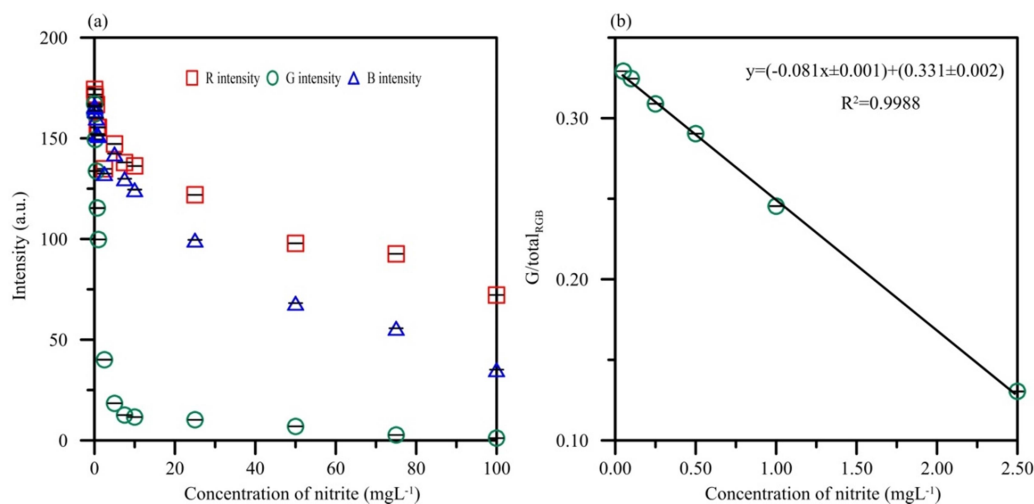
Figure 12 Relationships between (a) the concentration of nitrite and RGB intensities (b) IG/ITotal from color products.

The analytical performance and method validation where the DIC calibration curve for quantitative analysis of nitrite was established by plotting the analyzed RGB intensities of the digital image of the color products against the concentrations of nitrite (0 to 100 mgL^{-1}). The linear portion was selected for quantitative analysis by considering the widest concentration range of nitrite that provided linearity (R^2) > 0.99. Intra–day precision in terms of percentage relative standard deviation (%RSD) was investigated by testing three GMSS sensors in the same day. The same experiments were performed on five consecutive days for inter–day precision. The accuracy in terms of the percentage relative error (%RE) was evaluated by analyzing the nitrite standard at a known concentration (0.75 mgL^{-1}) against the established calibration curve. The detection limit was determined based on the IUPAC guidelines by testing ultrapure water using 12 GMSS sensors. After their digital images were analyzed, the standard deviation of the RGB intensities was used to calculate the LOD as 3SD/slope of the calibration graph (m) (Danzer and Currie, 1998). This result show system performance and method validation of analytical performance of GMSS and DIC for the analysis of nitrite was investigated. Since the red–violet product specifically absorbed the light at 543 nm, the IG presented the highest sensitivity (70 ± 2 $a.u.Lmg^{-1}$) with good linearity (R^2 = 0.9968). The linear range of the IG relationship was in the range of 0.05 to 1.0 mgL^{-1}, while the limit of detection (LOD) and limit of quality (LOQ) were found to be 40 ± 8 μgL^{-1} and 120 ± 30 μgL^{-1}–NO_2^-, respectively (equal to 12.2 and 36.5 μgL^{-1} NO_2^-–N, respectively). These are lower than the concentration limits for drinking water suggested by the US Environmental Protection Agency (1 mgL^{-1}) EPA, 1987 and the World Health Organization (3 mgL^{-1} for short term, and 0.2 mgL^{-1} for long–term exposure) WHO, 2003. A wider linear range was obtained from IG/ITotal (0.05 to 2.5 mgL^{-1}) with a lower LOD of 15 μgL^{-1} and an LOQ of 50 μgL^{-1} (equal to 4.6 and 15.2 μgL^{-1} NO_2^-–N, respectively). The colorimetric test using GMSS also provided good accuracy from quantifying control samples (0.75 mg L^{-1}, n = 3) with a 2.67 % relative error, while the %recovery of spiked water samples (ultrapure, tap, and seawater samples collected from a source far from human activities) were in the range of 88–114 % (Table 1). Good intra–day precision of 1.30%RSD from nine GMSS sensors was obtained while the analysis of nitrite using 15 GMSS sensors

over five days provided 1.93%RSD. When the cost of the GMSS as a nitrite sensor was considered, one sheet costs only 0.75 THB (0.02 USD), while each sensor (thin sheet and flat cap) costs ~1.25 THB (0.04 USD) which is much cheaper than other commercially available test kits, e.g., Nitrite Chemical Test Kit HI3873, (0–1 mgL^{-1}) which costs 36 USD/100 tests and Nitrite Low Range Checker HI707–25 (0–600 µgL^{-1}) which costs 13 USD/25 tests.

Table 1 Recovery test from spiked control samples.

Samples	Nitrite added (mg L^{-1})	Nitrite found (mg L^{-1})	Recovery (%)
Ultrapure water	0	0	-
	0.5	0.57±0.05	114±12
	1.0	0.99±0.01	99±1
Tap water	0	0	-
	0.5	0.44±0.03	88±10
	1.0	1.08±0.05	108±4
Sea water	0	0.005±0.02	-
	0.5	0.57±0.05	113±6
	1.0	0.94±0.09	94±12

2.1.4 Influence of coexisting ions and matrix effect

The feasibility influence of coexisting ions and matrix effect from other substances on nitrite testing using GMSS was investigated. Several possible substances present in sea water which might interfere with the reaction with nitrite were tested with GMSS at concentrations of 10,000 mgL^{-1} with the pH adjusted to 6. These comprised Na^+, Mg^{2+}, Ca^{2+}, Cu^{2+}, Ni^{2+}, Pb^{2+}, Zn^{2+}, F^-, Cl^-, OH^-, NO_3^-, CO_3^{2-}, and SO_4^{2-} (Mehmeti et al., 2016). Red–violet product was observed only from nitrite ions even at a much lower concentration (1 mgL^{-1}), while no color change

was observed from any of the other ions (Fig. 13). A possible coexisting interference effect was also evaluated by adding each ion at a concentration of 10,000 mgL^{-1} to a nitrite standard solution with a concentration of 0.5 mgL^{-1} and adjusting the pH to 6 before testing with GMSS. The IG of the digital images of the products showed changes in the range of 0.01–4.69 % (Table 2), indicating good selectivity of GMSS for nitrite. The influence of the seawater matrix was evaluated using seawater sampled from the Andaman Sea far from human activity (1 km from He Island, 8 km from Chalong Pier, Phuket province, Thailand). The seawater was used to prepare nitrite standard solutions at various concentrations (0–1 mgL^{-1}, adjusted to pH 6) instead of ultrapure water. The sensitivity of the standard graph from using seawater was compared to that using ultrapure water. The effect of the seawater matrix was also evaluated by using seawater which was expected to be a non–nitrite containing sample, to prepare working standard solutions and comparing the results with those from using ultrapure water for both the GMSS and standard methods. The sensitivity of the IG from for nitrite using seawater was different from that using ultrapure water by 3.18% for the GMSS method (Fig.14a) and 0.27 % for the standard method (Fig. 14b).
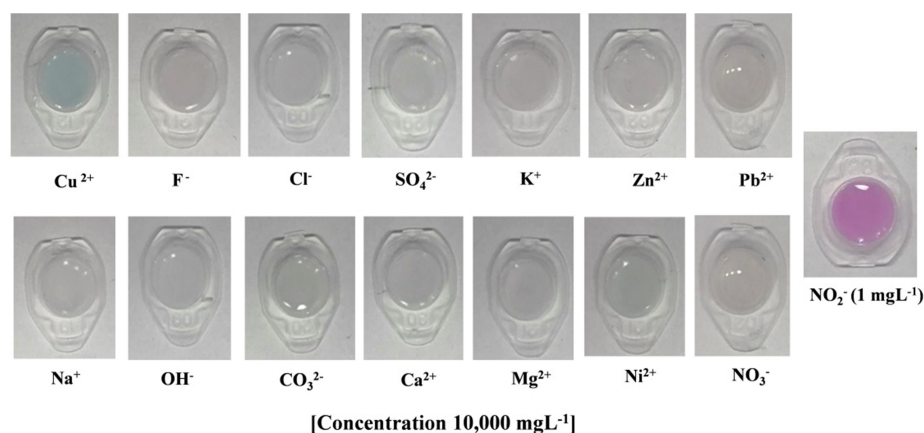
Figure 13 Color products obtained from testing various ions (10,000 mgL^{-1}) and nitrite (1.00 mgL^{-1}) using GMSS.
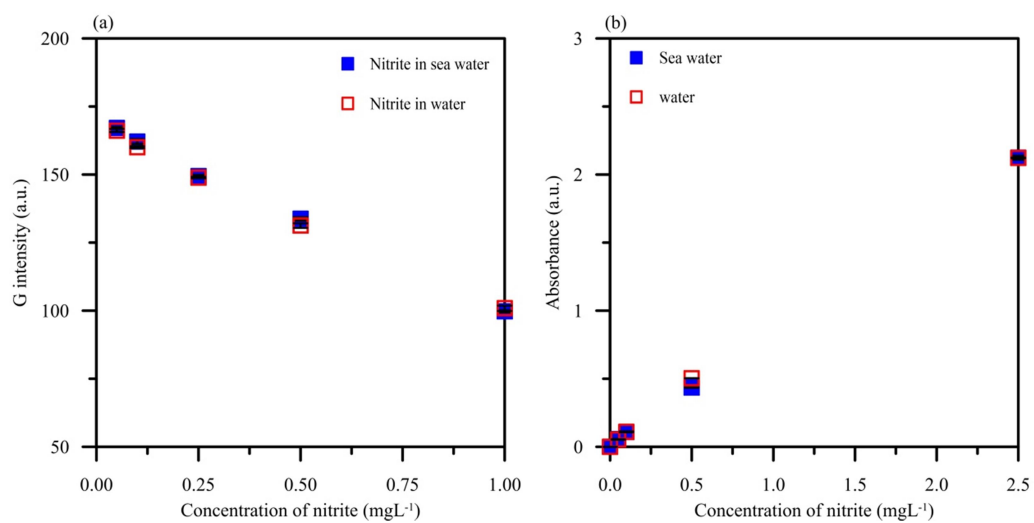
Figure 14 Standard graphs obtained from testing nitrite solution prepared using seawater (a) developed method (b) standard spectrophotometric method.

Table 2 Concentration of coexisting ions and the change of IG response (concentration of nitrite at 0.50 mg L^{-1}).

Ion interference	Concentration interference (mg L^{-1})	% change of I_G
Cu^{2+}	10,000	-4.69
K^+	10,000	-0.78
Zn^+	10,000	2.19
Na^+	10,000	-3.92
Ca^{2+}	10,000	1.71
Mg^{2+}	10,000	-3.52
Ni^{2+}	10,000	-4.29
Pb^{2+}	10,000	-3.22
F^-	10,000	3.78
NO_3^-	10,000	-2.60
Cl^-	10,000	2.87
OH^-	10,000	-0.73
CO_3^{2-}	10,000	-4.19
SO_4^{2-}	10,000	-0.01

2.1.5 Real sample analysis

In this work, colorimetric sensor was applied for monitoring nitrite in water. Therefore, the GMSS and DIC for on–site quantitative analysis was also evaluated. Since the DIC requires a custom–built RGB analysis box to eliminate any effects from environmental light, this box was used outside the laboratory to investigate the influence of environmental light. The results showed that the RGB intensities remained unaffected by external lighting being on or off (Fig. 15), indicating that external light had no measurable effect on the system developed, which can thus be used for on–site quantitative analysis of nitrite.
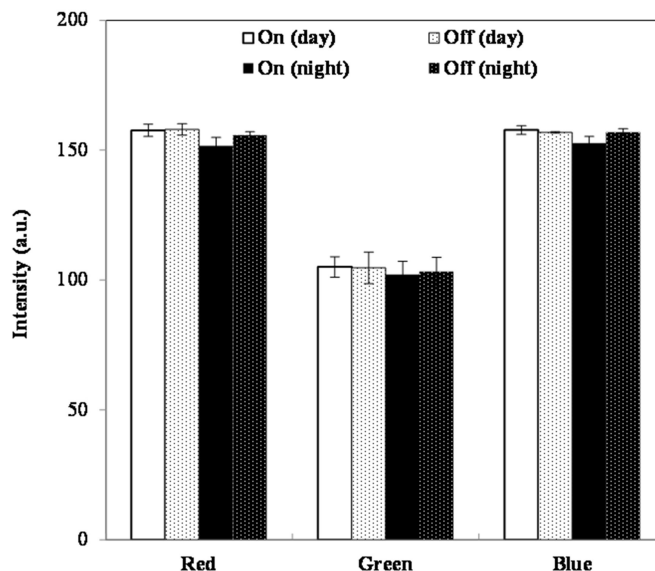
Figure 15 RGB intensities of color product photographed in various external light conditions using a custom–built RGB analysis box.

The real sample analysis of GMSS and DIC were applied to investigate nitrite contamination in seven seawater samples randomly collected from Kalim and Tri Trang Beaches (Phuket, Thailand; Fig. 16) which is often found to suffer from eutrophication, as well as an effluent sample from a hotel treatment plant at Kalim Beach (K1). The samples were kept in polyethylene bottles without airspace HELCOM, 2017 and stored in ice in a styrene foam box. They were then filtered through a 0.20 μm cellulose acetate membrane and the pH adjusted to 6 before being tested with the GMSS/DIC method developed within a few hours. All the samples were also analyzed using the standard method for nitrite detection using a spectrophotometric for comparison EPA, 2001.
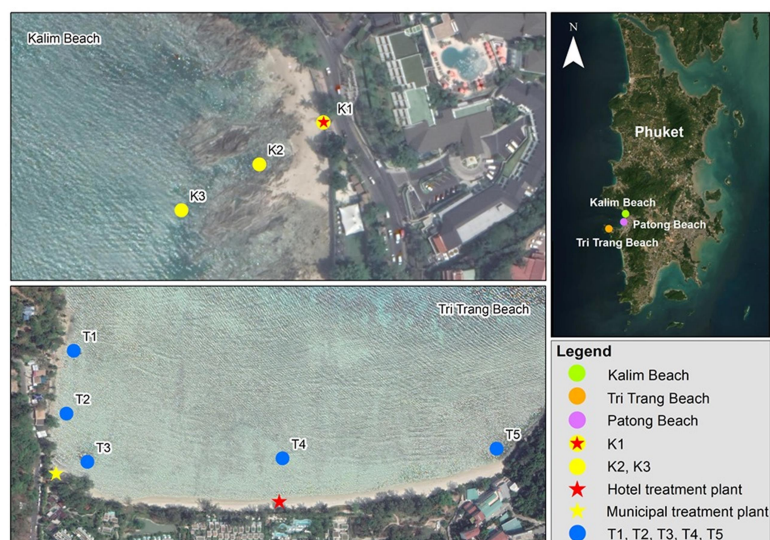
Figure 16 Sampling points for real samples.

The result of real sample analysis using GMSS and DIC are shown in Table 3. The highest concentration of nitrite of 4.52 ± 0.79 mgL^{-1} was found in the effluent from the hotel treatment plant at Karim Beach (K1), while the concentration of nitrite at K2 (0.13 ± 0.02 mgL^{-1}) was lower than at K1, but higher than at K3, where the effluent was diluted by seawater. No effluent from the hotel treatment plant at Tri Trang Beach, could be collected on the day of sampling, however nitrite was found in seawater samples collected at T3 and T4 located near municipal and hotel treatment plants at levels of 0.11 ± 0.04 and 0.14 ± 0.06 mgL^{-1}, respectively. The results obtained using GMSS were not significantly different from those obtained using the standard spectrophotometric method at the 95% confidence level (calculated t–value $= 0.893$, critical t–value $= 2.776$, degrees of freedom $= 4$).

Table 3 Concentration of nitrite in seawater collected from Kalim and Tri Trang Beach, Phuket.

Sample	Concentration (mgL^{-1})	
	Developed method	Spectrophotometric method
K1	4.52 ± 0.79	4.11 ± 0.87
K2	0.13 ± 0.02	0.20 ± 0.04
K3	nd	nd
T1	0.08 ± 0.00	nd
T2	0.07 ± 0.02	0.12 ± 0.02
T3	0.11 ± 0.04	0.15 ± 0.06
T4	0.14 ± 0.06	0.17 ± 0.07
T5	0.04 ± 0.02	nd

nd, no detectable

2.1.6 Stability of GMSS

The stability of the sensors, a quantity of 135 GMSS sensors was prepared in a single batch for stability testing. Three sensors were tested with nitrite standard solution (0.5 mgL^{-1}) on the day of preparation, while the remaining 132 sensors were kept to evaluate their stability. They were vacuum sealed in packs of three (44 packs in total) and kept in three different conditions, consisting of storage in a refrigerator at 4 °C, a desiccator (Acrylic D50–A, Northman, Thailand), and at ambient conditions. One pack (three sensors) was taken from each condition for testing with nitrite standard solution every day for a week, and then their performance was monitored on a weekly basis for 3 weeks, then after 2, 3, 6, and 12 months of storage. The results of the stability evaluation showed that the color intensity resulting from nitrite testing (IG, 0.5 mgL^{-1}) changed by +5.5%, –25.9%, and –24.1% after storage in a refrigerator, desiccator, and ambient conditions, respectively, for 3 months. After 1 month of storage in a desiccator, the color intensity from the GMSS

decreased by only 8.3 %, while the IG of those kept for 1 month at ambient conditions decreased by 15 % indicating that it was less stable when kept under those conditions. Thus, it is recommended that GMSS should be kept in a refrigerator where an increase in color intensity of 12.6% was found after one year's storage (Fig. 17).
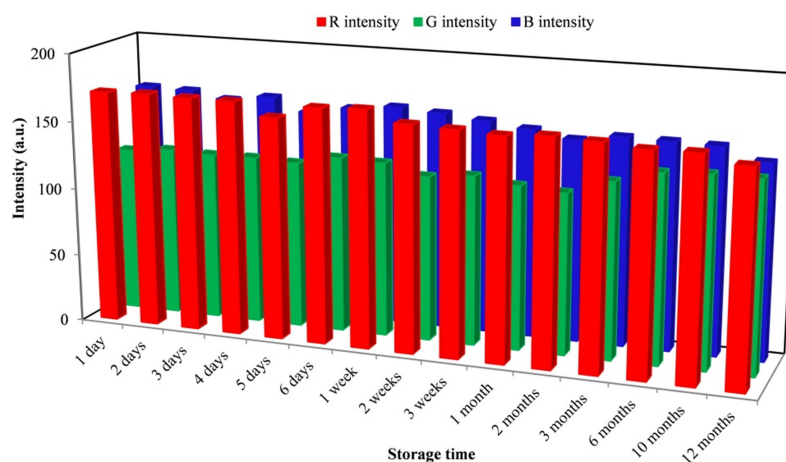
Figure 17 RGB intensities of GMSS stored in refrigerator at various storage times.

2.2 Development of bio–adsorbent for phosphate removal

In this study, a novel starch based monolithic cryogel was composited with calcium silicate hydrate to develop a floatable bio–adsorbent for phosphate removal and recovery. Calcium silicate hydrate (C–S–H) is a semi–crystalline material and is the main component in Portland cement (Yoobanpot et al., 2017) that has been reported to remove phosphate by crystallization (Lee et al., 2018; Okano et al., 2016; Zhang et al., 2019). Its structure is constituted by distorted central Ca–O sheets with silicate tetrahedral chains flanking on each side (Franceschini et al., 2007) and usually it coexists with other crystal phases, e.g., calcium hydroxide (Ca(OH)$_2$) and unreacted phases (Li et al., 2017). C–S–H can dissociate into calcium and silicate in water, and these aggregate or grow hydroxyapatite crystals with phosphorus on their surfaces (Okano et al., 2015). Since C–S–H would act as the calcium ion donor and the pH adjuster at the same time in the recovery process, it has been reported to

be a phosphorus recovery material in biological wastewater treatment process with excellent biocompatibility and biodegradability (Lee et al., 2018; Okano et al., 2016; Zhang et al., 2019). It also exhibits better settleability than conventional calcium compounds with high capacity to crystallize with soluble phosphorus forms that can be used directly as fertilizer (Lee et al., 2018; Okano et al., 2015; Okano et al., 2013).

Various forms of C–S–H have been reported for phosphate removal and recovery. Porous C–S–H exhibits stronger capacity of calcium ion release than crystalline C–S–H as well as higher phosphate species recovery performance (Chen et al., 2009; Guan et al., 2013). C–S–H gel, metastable with respect to crystalline C–S–H, is supposed to have higher calcium ion releasing ability than crystalline C–S–H due to its higher solubility (Maeda et al., 2018), although its removal efficiency is slightly lower than that of $Ca(OH)_2$ (Lee et al., 2018). Amorphous calcium silicate hydrates (A–CSHs) have also been reported for phosphorus recovery with higher potential for phosphorus removal than conventional crystalline C–S–H (Okano et al., 2015; Okano et al., 2016; Okano et al., 2013). Its precipitate also exhibited better settleability, filterability, and dewaterability than conventional $CaCl_2$ and $Ca(OH)_2$ (Okano et al., 2015; Okano et al., 2016; Okano et al., 2013). However, separation of fine crystallites after crystallization from these C–S–H is still difficult and this has limited practical applications to wastewater treatment and phosphorus recovery (Peng et al., 2018). A magnetic calcium silicate hydrate composite material (Fe_3O_4@CSH) has thus been developed to remove and recover phosphate via chemical adsorption in order to improve C–S–H efficiency and settleability (Peng et al., 2018). Although the Fe_3O_4@CSH materials are effective for phosphate adsorption with a maximum adsorption capacity of 55.84 mg phosphorus/g and could be quickly separated by an external magnet, calcium–containing chemical (e.g., $CaCl_2$, $Ca(OH)_2$) is required to be added to the alkaline solution to convert the phosphate to calcium phosphate fertilizer for use in agriculture (Peng et al., 2018). The C–S–H powder has also been immobilized in polyvinyl alcohol matrix (PVA–CSH) and then used for phosphate removal (Ding et al., 2018). Although the PVA–CSH can reduce the loss of C–S–H powder during removal process, PVA is a synthetic petroleum–based polymer that may affect environment along its lifetime from first time in synthesis and finally during degradation. The use of a natural

polymer, e.g., starch, is thus a better choice to prepare a novel material for environmental pollutant removal that can remain environmentally friendly.

2.2.1 Preparation of calcium silicate hydrate composite starch based cryogel (Cry–CSH)

A rapid ultrasound-assisted sol–gel method was used to synthesize C–S–H at room temperature as reported in the literature (Zhang et al., 2019). Briefly, a $CaCl_2$ solution was added dropwise into a Na_2SiO_3 solution under ultrasound irradiation (300 W) in ultrasonic bath with Ca/Si molar ratios of 1.2 and a solid/liquid ratio of 1/8. White sol immediately occurred and gradually hardened, the sample was then taken out and gelled in a plastic container at room temperature. The obtained gel was then soaked with ultrapure water (10 gL^{-1}) for 1 h to remove free $Ca(OH)_2$ before filtering the suspension through a 0.45 μm membrane filter. The obtained C–S–H was then incubated at 80°C for 24 h in an oven before keeping in desiccator for further use.

A starch based cryogel (Cry) was prepared by modifying the procedure to prepare famous Thai dessert "Lod–chong" coupled with conventional freeze and thaw technique. Rice flour (12.5 g) and tapioca starch (3.75 g) were dispersed in 130 mL of limewater, which is saturated calcium hydroxide solution prepared by dissolving red lime (RL) in ultrapure water (15 gL^{-1}) and kept for at least 3 days before taking the upper clear supernatant solution. The mixture was then gradually heated from 60 to 200°C for 1.5 h until the starch completely gelatinized and became clear. In the case of Cry–CSH, the C–S–H (0.6 to 6 g) was added in starch gel (60 g) and further mixed to obtain homogenous mixture before cooling the mixture under continued stirring for 5 min. The mixture was tightly pulled into a 50 mL plastic syringe and then placed in a freezer for freezing at –20°C for 24 h. The resultant monolith was then thawed at room temperature and a freeze and thaw process was repeated for three cycles. The cryogel was then removed from the container before cutting into smaller pieces (1 cm lengths). The obtained materials were then soaked in 95% ethanol for 24 h before drying in an oven at 100°C until achieving the stable

weight. All obtained cryogels were kept in zip–lock plastic bags and placed in desiccator until further use.

A novel calcium silicate hydrate composite cryogel based on native starch (Cry–CSH) was successfully synthesized for phosphate removal and recovery. Prepared C–S–H was added in a gel precursor, containing rice flour, tapioca starch, and limewater, before following the freeze and thaw technique to produce a composite monolithic cryogel. Due to the high pH of limewater (pH ~ 11.8), hydroxyl groups of starch have oxidized making their sites ionic cross–linking with the Ca^{2+} or $Ca(OH)^+$ of dissociated limewater and tightening the starch chain (Bryant and Hamaker, 1997; Chanjarujit et al., 2018; Israkarn and Hongsprabhas, 2017; Israkarn et al., 2007; Wing et al., 1987). However, our recent work found that no new chemical bond has been observed in FTIR spectrum of the obtained cryogel with Ca^{2+}, Ca^{2+} thus may interact with starch molecules by a physical cross–linking via Van der Waals interactions as in prior reports (Cornejo-Villegas et al., 2018; Pineda-Gómez et al., 2012). For Cry–CSH, C–S–H was added after gelatinization of starch, the Si–O from C–S–H molecules can interact with available hydroxyl groups of starch as shown in the proposed mechanism in Fig. 18. Prepared gel precursor with and without C–S–H (Cry–CSH and Cry, respectively) was then transferred into the container (50 mL plastic tube) and frozen. This made water in polymeric matrix freeze to ice crystals, while non–frozen Ca–starch phase for Cry and Ca–Starch–CSH for Cry–CSH may continue cross–linking between Ca^{2+}, C–S–H and starch molecules for the formation of relatively thin walls (Cui, 2011; Mattiasson et al., 2009; Plieva et al., 2005). The materials were then allowed to thaw at room temperature making the ice crystals melt and leaving an interconnected macroporous sponge–like material. The obtained Cry and Cry–CSH had similar appearances and tolerated compression without damage, indicating high elasticity which is a cryogel characteristic. In addition, Cry–CSH can float on water surface for at least 105 days without any damage.
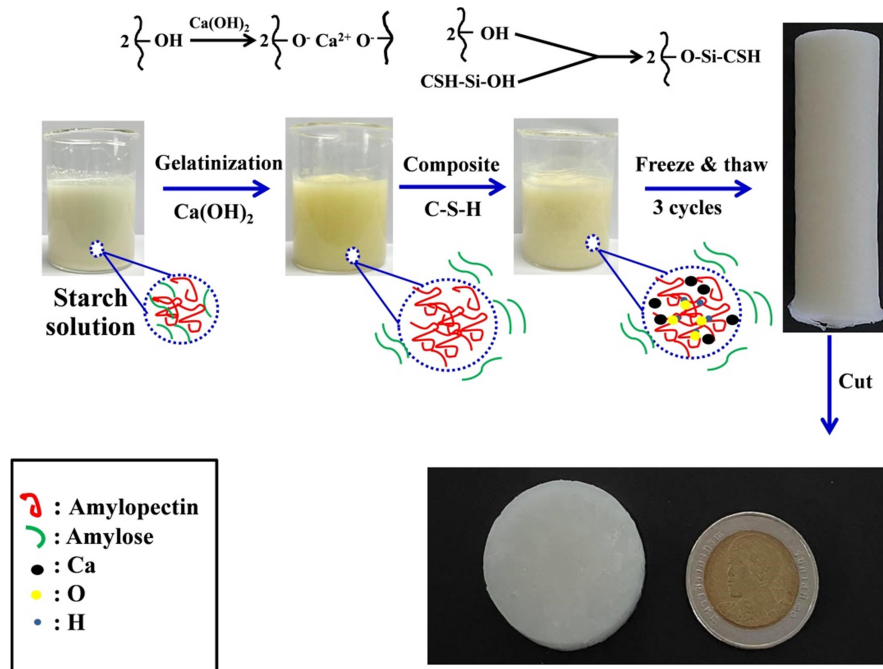
Figure 18 Proposed mechanism for synthesis of Cry–CSH.

2.2.2 Characterization of calcium silicate hydrate composite starch based cryogel (Cry–CSH)

Characterization of C–S–H and Cry–CSH in term of morphology of C–S–H, Cry, and Cry–CSH were investigated using field emission scanning electron microscopy (FE–SEM; FEI, Czech Republic). The functional groups of the materials were analyzed with Fourier transform infrared spectroscopy (FT–IR; Bruker, Germany) using ATR technique and KBr pellet at 4000–600 cm^{-1}, respectively. X–ray diffraction (XRD) patterns were obtained from X–ray diffractometer (Empyrean, PANalytical, Netherlands) using monochromatic Cu Kα radiation. The surface area, porosity, and pore size distribution of as–prepared materials were investigated using a high throughput surface area and porosity analyzer (ASAP2460, Micromeritics, USA). They were degassed at 105°C for 30 min to remove physically absorbed gases from the sample surface before analyzing the nitrogen adsorption/desorption isotherm at 77 K. The specific surface area (S_{BET}) calculated using the Brunauer–Emmet–Teller (BET) method and the pore volume estimated from an adsorption branch using the

Barrett, Joyner and Halenda (BJH) method were used to estimate the average pore diameter.

The FESEM images of the prepared C–S–H, Cry, and Cry–CSH are shown in Fig. 19. SEM images of the Cry (Fig. 19a) revealed macropores in interconnected polymer network, similar to those synthesized using other polymers (Choodum et al., 2016; Lozinsky, 2008). The C–S–H nanoparticles showed an agglomeration of crystalline nanoparticles with rough surface (Fig. 19b). When C–S–H was added into a gel precursor to produce the Cry–CSH, the nanoparticles would be trapped within the walls of the cryogel (Fig. 19c–d) resulting in thicker walls. The FESEM image of Cry–CSH after adsorption of phosphate for 2 h showed spherical particles of amorphous calcium phosphate (ACP) (Fig. 19d) similar to those reported previously (Zhang et al., 2019). The presence of phosphorus is also evidenced in Cry–CSH after phosphate adsorption from SEM–EDX results (Fig. 20). Similar XRD patterns were observed for Cry–CSH before and after adsorption of phosphate for 2 h (Fig. 21) as in previous work where no difference was detected in the XRD pattern within 2 h because the ACP would begin to turn to hydroxyapatite (HAP) after 8 h and then was completely converted at 24 h (Zhang et al., 2019). Although the presence of $Ca(H_2PO_4)_2$ and $CaHPO_4$ have been evidenced in the C–S–H after phosphate adsorption (Peng et al., 2018; Zhang et al., 2019), the $H_2PO_4^-$ and HPO_4^{2-} V_3 vibration commonly present at 1038 cm^{-1} (Peng et al., 2018) or 1046 cm^{-1} (Zhang et al., 2019) overlapped with vibration bands from starch in Cry–CSH (Fig. 24).
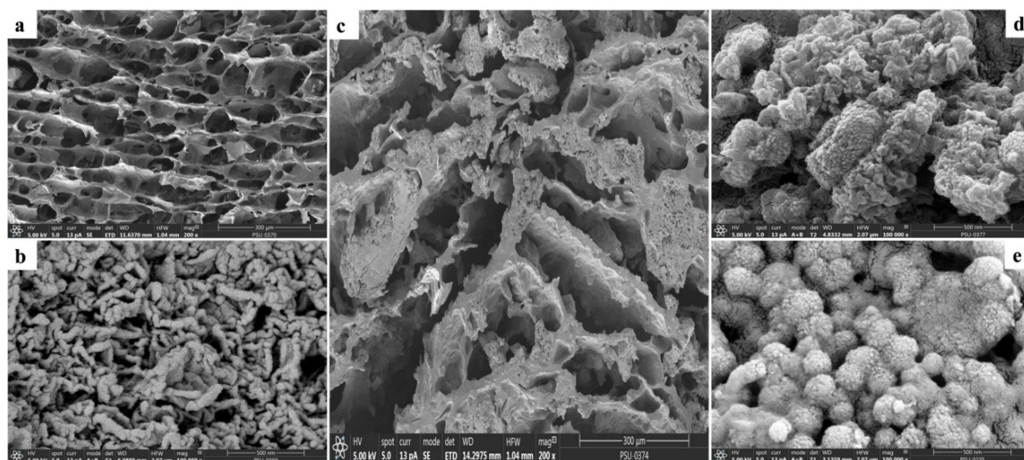
Figure 19 FESEM images of (a) Cry (b) C–S–H (c–d) Cry–CSH before adsorption of phosphate (e) Cry–CSH after adsorption of phosphate.
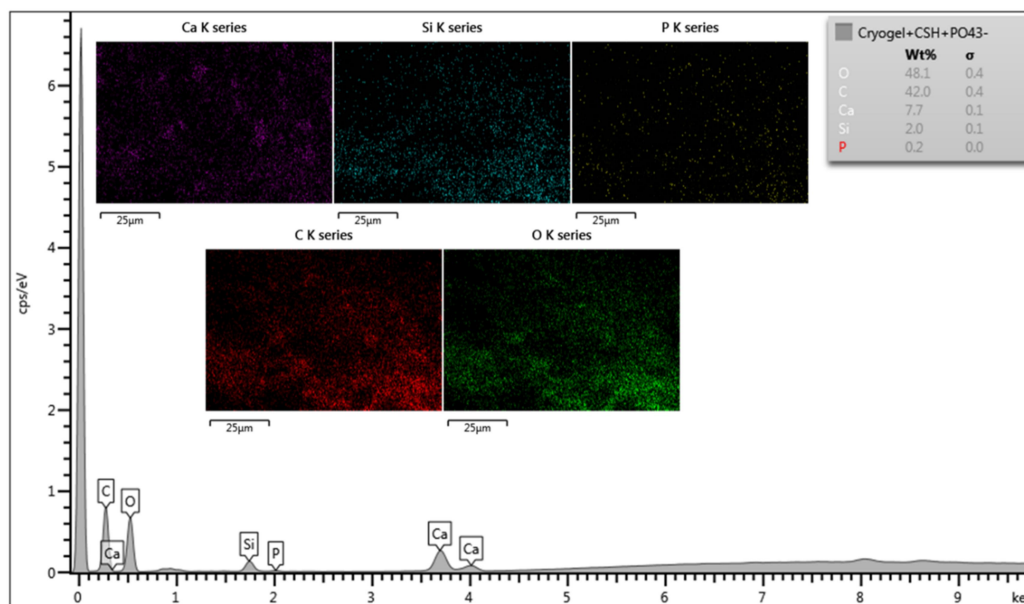
Figure 20 SEM–EDX Cry–CSH after adsorption of phosphate for 2 h.

The XRD patterns of the prepared C–S–H, Cry, and Cry–CSH are shown in Fig. 21. The diffraction pattern of prepared C–S–H showed weak broad peaks at 29.1°, 31.9° and 49.9° corresponding to a typical diagram of relatively ordered C–S–H reported in the literature (Franceschini et al., 2007; Guan and Zhao, 2016; Zhang et al., 2019). The weak peaks of calcite at 29.4°, 36.0°, 39.4°, 43.1°, 47.5° and 48.5° also reflect the unavoidable contact with atmospheric carbon dioxide during the synthesis process (Zhang et al., 2019). The diffraction peak observed ~6.9° was attributed to the (001) reticular planes with distance given by the Bragg relation of 12.8 A˚, corresponding to the interlamellar distance reported previously for C–S–H (12 A˚≤ d001 ≤14 A˚) (Franceschini et al., 2007). The three most intense bands at higher angles are attributed to the (hk0) reticular planes, which are characteristic of the organization of calcium atoms within each C–S–H layer with the distances of 3.06, 2.80 and 1.83 A˚ for d110, d200 and d020, respectively (Franceschini et al., 2007). The XRD patterns of the prepared cryogels revealed a broad hump centered at 2θ ~20° for the amorphous structure, although the characteristic peaks of a V–type crystalline structure of starch were observed at 13.2° and 19.9° (Chanjarujit et al., 2018; Domene-López et al., 2019). The loss of starch crystallinity in the prepared cryogel was caused by the crystallinity of starch granule being disrupted during gelatinization at an elevated temperature (Cornejo-Villegas et al., 2018; Zou and Budtova, 2021) and the cross–linking with Ca^{2+}. For Cry–CSH, the broad hump indicating amorphous structure of cryogel remained in the pattern as well as the characteristic peaks of C–S–H, but with lower intensities for both. This indicates that the in–plane organization of the calcium atoms in Cry–CSH was the same as in C–S–H (Franceschini et al., 2007).
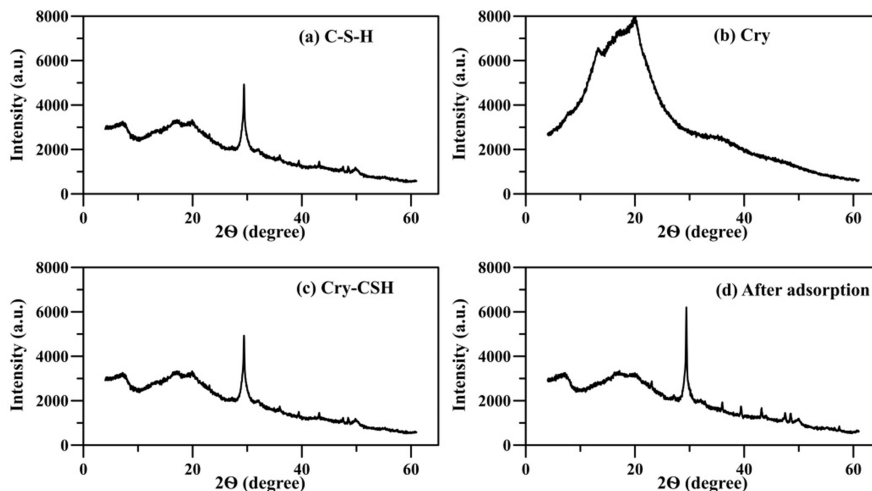
Figure 21 The XRD patterns of the prepared (a) C–S–H, (b) Cry, (c) Cry–CSH before and (d) after adsorption of phosphate.

The adsorption based average pore diameter from the BET analysis of Cry was 0.39 nm with specific surface area (S_{BET}) of 0.7142 m^2g^{-1} and low total pore volume of 0.001 mLg^{-1}. The obtained surface area corresponded to other reports showing low specific surface areas, e.g., 0.6 to 7.7 m^2g^{-1} (Baudron et al., 2019), for porous material synthesized from native starch using freeze-drying. The S_{BET} of C–S–H was found to be much higher at 85.22 m^2g^{-1} than that of Cry, as in previous syntheses using the same method (17.31 m^2g^{-1} to 37.20 m^2g^{-1}) (Zhang et al., 2019), but with a lower total pore volume (0.020 mLg^{-1} compared to 0.0651 mLg^{-1} to 0.1779 mLg^{-1}) (Zhang et al., 2019). The average pore diameter of C–S–H (1.05 nm) was larger than that of Cry, but smaller than in previous work (~15 nm) (Zhang et al., 2019). As expected, the S_{BET} of Cry–CSH (11.03 m^2g^{-1}) and total pore volume (0.003 mLg^{-1}) were lower than of C–S–H, but higher than of Cry, while the average pore diameter (0.97 nm) was larger than that of Cry, but smaller than that of C–S–H. Although the prepared Cry–CSH had larger S_{BET} than PVA–CSH (4.12 m^2g^{-1}), its total pore volume was less than that of PVA–CSH (0.01 mLg^{-1}) (Ding et al., 2018). The pore size distributions of C–S–H, Cry, and Cry–CSH (Fig. 22) calculated by the non–local density functional theory (NLDFT) based on a N_2–DFT model showed the most pore volume for the pore width from ~5 to 50 nm in

the mesopore range, although macropores (> 50 nm) were also observed. All prepared materials exhibited a typical type IV adsorption isotherm (Fig. 23) where the capillary condensation occurred after multilayer adsorption of N_2 within mesopores (Hattori et al., 2013; Thommes et al., 2015) confirming the presence of mesopores in all cases. They revealed an H3 hysteresis indicating slit–shaped pores formed by non–rigid aggregates of plate–like particles and/or pore network consisting of macropores which are not completely filled with pore condensate (Thommes et al., 2015). The open hysteresis loops observed for Cry (Fig. 23a) could be attributed to non–rigid structure of the Cry synthesized from starch, so that it may deform (swell) during adsorption or pore filling (Qi et al., 2017). The trapped nitrogen also cannot be released due to the affinity of nitrogen in cryogel caused by the heterogenous Cry surfaces (Qi et al., 2017). The addition of C–S–H in starch gel precursor made the Cry–CSH show closed H3 hysteresis (Fig. 23c) similar to C–S–H, indicating more rigid structure with less swelling than for Cry (Fig. 23b).
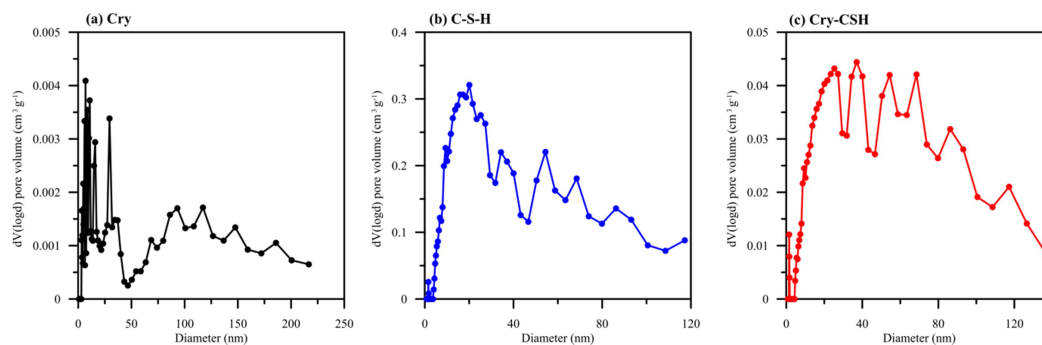
Figure 22 The pore size distribution of (a) Cry, (b) C–S–H, and (c) Cry–CSH.
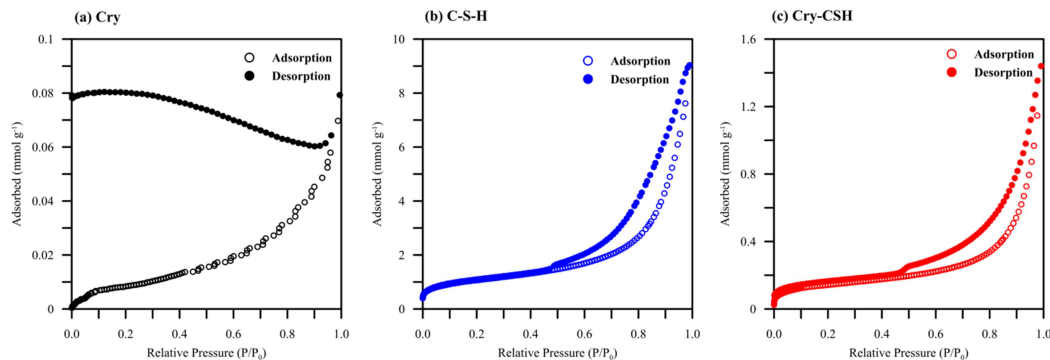
Figure 23 The nitrogen adsorption isotherm of (a) Cry, (b) C–S–H, and (c) Cry–CSH.

The FTIR spectrum of C–S–H revealed the O–H stretching absorption band at 3448 cm^{-1} from water molecules (García-Lodeiro et al., 2008; Yu et al., 2004). This band was also observed in Cry at 3412 cm^{-1} (Fig. 24), attributed to hydroxyl groups in starch molecules which may interact with Ca^{2+} located in their surroundings, as reported previously (Pineda-Gómez et al., 2012). This peak was observed at a wavelength between C–S–H's and Cry's, i.e., 3423 cm^{-1}, for Cry–CSH. The absorption band at 1640 cm^{-1} in C–S–H was attributed to H–O–H bending from water molecules (García-Lodeiro et al., 2008; Yu et al., 2004), while it shifted to 1648 and 1651 cm^{-1} in Cry–CSH and Cry, respectively, due to interactions with Ca^{2+} located in the surroundings (Pineda-Gómez et al., 2012) and/or overlap with the C–O bending in amylopectin. The peaks observed at 1491 and 1430 cm^{-1} in C–S–H spectrum were assigned to C–O asymmetric stretching vibrations of carbonate (García-Lodeiro et al., 2008; Yu et al., 2004), which seems to overlap with the vibrations of C–H symmetrical scissoring of CH$_2$OH moiety in amylopectin observed at 1418 cm^{-1} (Cornejo-Villegas et al., 2018) in Cry, and appearing at 1459 and 1424 cm^{-1} in the composite. The intense band at 970 cm^{-1} in the spectrum is attributed to Si–O stretching vibrations also overlapping the intense peaks from 1083 cm^{-1} to 931 cm^{-1} contributed by vibrations of C–O bonding in amylopectin (Boonkanon et al., 2020; Choodum et al., 2019; Wongniramaikul et al., 2018) in Cry and presented maximum absorption at 1019 cm^{-1} in Cry–CSH. The Si–O–Si bending was also observed in C–S–H and Cry–CSH spectra at 666 cm^{-1} (García-Lodeiro et al., 2008;

Yu et al., 2004), while absorption peak at ~450 to 452 cm^{-1} in both materials was associated with the deformation of SiO$_4$ tetrahedra (Yu et al., 2004). An intense peak appeared in Cry and Cry–CSH at ~2927 cm^{-1} contributed by the C–H stretching in starch molecules, while the peaks at ~1156 cm^{-1} were contributed by C–O–C vibrations in glycosidic linkage (Boonkanon et al., 2020; Choodum et al., 2019; Cornejo-Villegas et al., 2018; Wongniramaikul et al., 2018).
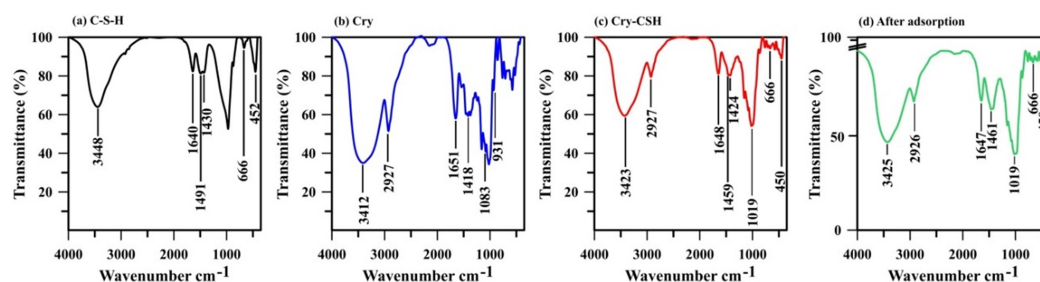
Figure 24 The FTIR spectrum of the prepared (a) C–S–H, (b) Cry, (c) Cry–CSH before and (d) after adsorption of phosphate.

2.2.3 Swelling ratio, water uptake capacity, water retention, and porosity of Cry–CSH

The swelling ratio, water uptake capacity, water retention, and porosity of Cry–CSH of cryogel characteristics including swelling ratio, water uptake capacity, water retention, and porosity of Cry–CSH were investigated following previous reports (Jayaramudu et al., 2019; Xue et al., 2004). The swelling ratio (S$_{g/g}$) was investigated by weighing the dried and wet Cry–CSHs. Three completely dried Cry–CSHs were equilibrated in 50 mL ultrapure water at ambient temperature. The water–adsorbed Cry–CSHs were weighed after removing the surface excess water with filter paper at certain time intervals up to equilibrium (1 to 1440 min). The swelling ratio of Cry–CSH was calculated using equation (1) (Jayaramudu et al., 2019; Lin and Hsu, 2020; Xue et al., 2004) where W$_t$ is the weight of swollen Cry–CSHs at an observation time and W$_0$ is the weight of dried Cry–CSHs. The swelling behavior of the cryogel was analyzed for pH in the range from 2 to 13 at a set of temperatures (20, 30, 40, 50, and 60°C).

$$\text{Swelling ratio } (S_{g/g}) = \frac{(W_t - W_0)}{W_0} \tag{1}$$

The water uptake capacity of Cry–CSHs (%) was calculated using equation (2) (Jayaramudu et al., 2019; Xue et al., 2004) where W_e is the weight of swollen cryogel at the equilibrium.

$$\text{Water uptake capacity (\%)} = 100 \times \frac{(W_t - W_0)}{(W_e - W_0)} \tag{2}$$

The equilibrated Cry–CSHs were then put in Petri dishes at room temperature and re–weighted at certain times. The weights of the Cry–CSHs (W_T) were recorded during the deswelling experiment until they had reached saturated values. The percentage of water retention (%de–swelling) can be calculated using the following equation (3) (Jayaramudu et al., 2019).

$$\text{Water retention (\%)} = 100 \times \frac{(W_T - W_0)}{(W_e - W_0)} \tag{3}$$

The porosity of Cry–CSHs (%) was calculated using equation (4) (Ertürk and Mattiasson, 2014) by squeezing the swollen gel and the weight of swollen gel (W_e) was compared to the weight after squeezing (W_q).

$$\text{Porosity (\%)} = 100 \times \frac{(W_e - W_q)}{W_e} \tag{4}$$

Swelling behavior of Cry–CSH including swelling ratios of Cry and Cry–CSH were measured as functions of time at 25 to 45°C. The swelling ratio of both materials increased with time and temperature (Fig. 25). Since swelling is the expansion of the polymer networks due to the interaction between the polymeric chains and water molecules, the swelling ratio increases with temperature because the interaction behavior disturbs the disentanglement of interpenetrated polymeric chains and destroys hydrogen bonds between the polymer molecules (Gupta and Shivakumar, 2012; Jayaramudu et al., 2019). The experimental results

showed that Cry–CSH reached equilibrium swelling at 60 min (5.51 $g_{water}/g_{Cry-CSH}$) before Cry (90 min; 9.96 g_{water}/g_{Cryl}) at 25°C. These were similar to the theoretical equilibrium swelling ratios (S_{eq}) obtained from a swelling kinetics investigation (5.48 $g_{water}/g_{Cry-CSH}$ for Cry–CSH and 9.97 g_{water}/g_{cry} for Cry) as described in Fig. 26. Apparently, the swelling ratio of Cry–CSH was lower than that of Cry that may contribute to the replacement of C–S–H in polymer chain network in Cry–CSH leading to more rigid material. The swelling rate constant (k_s) and initial swelling rate (r_i) of Cry–CSH were higher than those for Cry (Table 4) matching the rapid equilibration of Cry–CSH that may relate to the higher %porosity of Cry–CSH (50.85%) than of Cry (40.98%) that agrees with the total pore volume from BET analysis. The swelling mechanisms of Cry and Cry–CSH were also determined as described in Fig. 27. The swelling exponent *(n)* that can identify the water transport mechanism (Bajpai and Shrivastava, 2002; Jayaramudu et al., 2019; Murthy et al., 2006) was 0.010 and 0.016 for Cry–CSH and for Cry, respectively. Thus, water diffused through both materials with Fickian diffusion at a slower rate of water diffusion than the polymer relaxation rate (Bajpai and Shrivastava, 2002), matching the low swelling capacity of the materials. The low diffusion coefficient (D) of 0.0002 $cm^2 \cdot min^{-1}$ for Cry–CSH and 0.0012 $cm^2 \cdot min^{-1}$ for Cry (Fig. 28) indicates a slow diffusion rate of water through both materials leading to low swelling ratio, which is a characteristic feature of cryogels that are elastic.
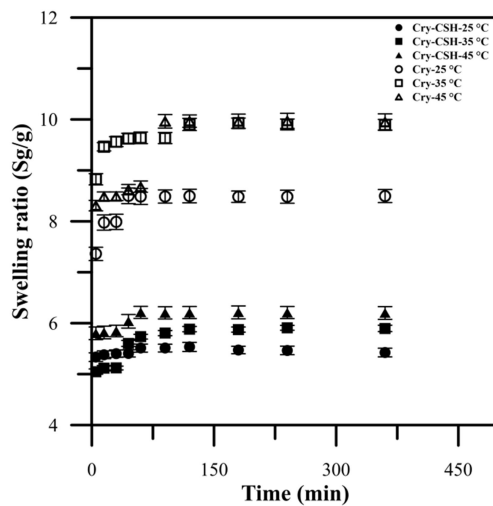
Figure 25 Swelling ratios of Cry and Cry–CSH at 25 to 45°C.
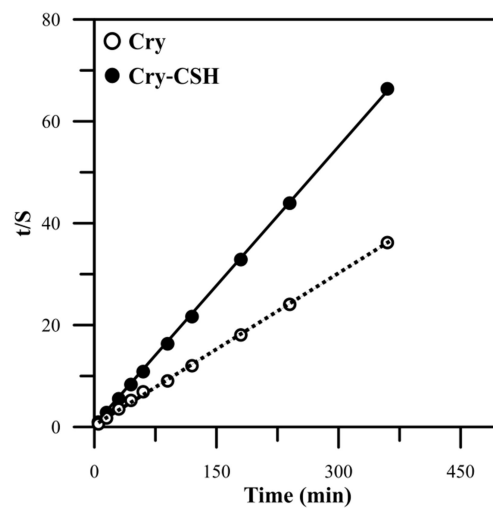
Figure 26 Relationship between t/S and t from investigation of swelling kinetics.

Table 4 Estimated swelling kinetic parameters.

Parameter	Cry	Cry-CSH
Swelling ratio at equilibrium (S) ($g_{water}/g_{cryogel}$)	9.96	5.51
Theoretical swelling ratio at equilibrium (S_{eq}) ($g_{water}/g_{cryogel}$)	9.97	5.48
Initial swelling rate (r_i) ($g_{water}/g_{cryogel}/min$)	3.66	13.95
Swelling rate constant (k_s) ($g_{cryogel}/g_{water}/min$)	0.04	0.46
Swelling exponent (n)	0.016	0.010
Diffusion coefficient (cm^2/min)	0.0012	0.0002
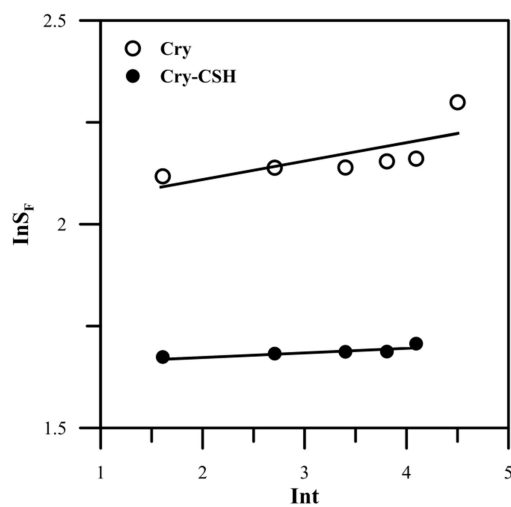
Figure 27 Relationship between ln S_F and ln t from investigation of swelling mechanism of the cryogels.
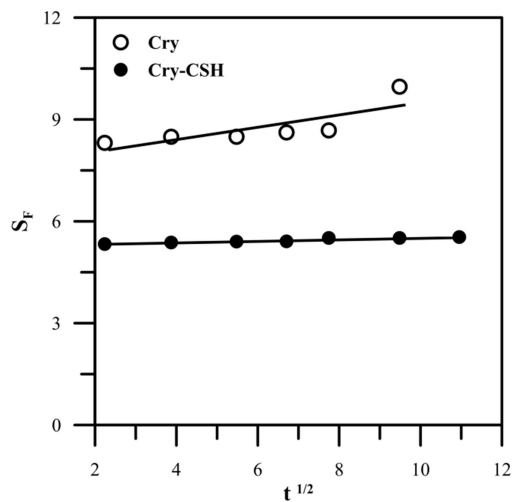
Figure 28 Diffusion curves of Cry and Cry–CSH.

The swelling ratios of Cry and Cry–CSH seems to be independent of pH (Fig. 29) that may contribute to the physical cross–links between Ca^{2+} ions surrounding the hydroxyl groups of the starch, and may limit the attachment of H^+ or OH^- on polymer chains. The results indicate that the material could be applied at a wide pH range without changes to swelling properties.
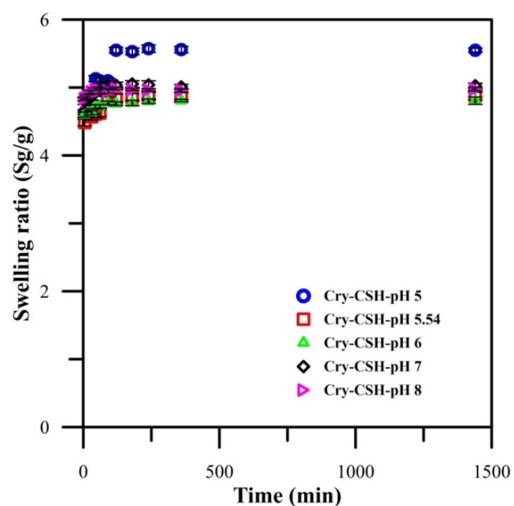
Figure 29 Influence of pH on swelling ratio of Cry–CSH.

The water uptake capacity in Fig. 30 showed that the water amounts completely adsorbed in Cry–CSH and Cry were 621% and 849% of their dry weights, after 60 and 90 min of immersion, and remain steady after 24–hour water uptake. On reversing the swelling process, the water retention ability of the cryogels was investigated. The water retention ability of both Cry and Cry–CSH decreased with time (Fig. 31) and Cry–CSH lost adsorbed water by ~84% at 24 h, more than Cry that lost water by 79%. Both materials completely lost the absorbed water in 36 h. These results indicate that both materials might have available hydroxyl groups that can form hydrogen bonds with water, resulting in delayed water evaporation.
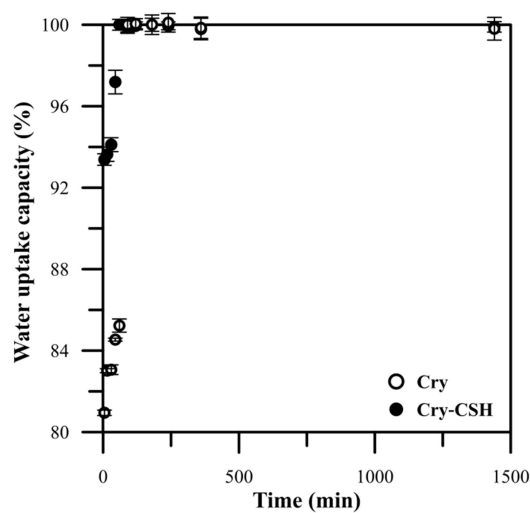
Figure 30 Water uptake capacity of Cry–CSH and Cry.
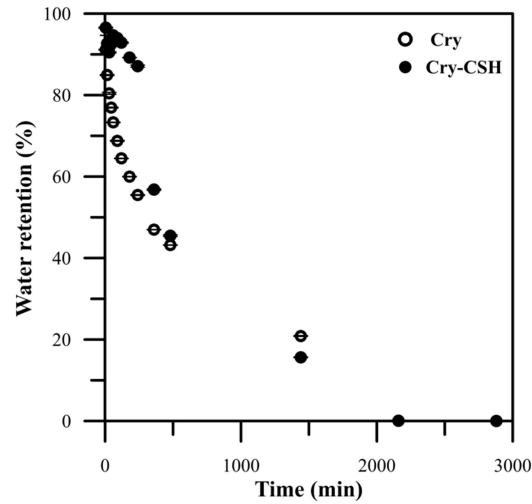
Figure 31 Water retention ability of Cry–CSH and Cry.

2.2.4 Phosphate adsorption by Cry–CSH

The optimum amounts of adsorbents of C–S–H for phosphate removal was investigated by varying doses of C–S–H for adsorption of 50 mgL^{-1} phosphate. The adsorption experiments were done by suspending the adsorbents at their optimum amount in 50 mL phosphate solutions with initial phosphate concentrations in the range from 0.1 to 100 mgL^{-1}. Similar runs were performed for a range of contact times (0 to 1,440 min), pH (5 to 8), and temperatures (25°C to 45°C) at the optimum initial concentration for kinetic studies. The amount of adsorbed phosphate at time t (Q_t: mgPO$_4^{3-}$/g) was calculated as the difference between phosphate concentrations in solution initially (C_i: mgL^{-1}) and at time t (C_t: mgL^{-1}) using the following equation (5) (Almanassra et al., 2020; Peng et al., 2018; Zhang et al., 2019):

$$Q_t = \frac{(C_i - C_t)}{W} \times V \tag{5}$$

where V is the volume of solution (L) and W is the dry mass of adsorbents (g). The phosphate removal efficiency (RE) was calculated using equation (6) where C_e is the phosphate concentration at equilibrium (mgL^{-1}). Each experiment was performed for three replicates and the average of these values was used in plots or any relationships.

$$\%RE= \frac{(C_i\text{-}C_e)}{C_i}\times100 \tag{6}$$

The results showed that increasing the amount of C–S–H from 0.1 to 1.0 g increased the %removal efficiency from 95.12 ± 0.08 to $99.39\pm0.02\%$ (Fig. 32a) and this thereafter remained constant. Since a high amount of adsorbent can slow down the adsorption by resistance to mass transfer between adsorbate with adsorbent in a limited space in container (Mezenner and Bensmaili, 2009; Torit and Phihusut, 2019; Yeddou and Bensmaili, 2007), 0.1 g C–S–H was then selected for further investigation. When C–S–H was composited with macroporous material in Cry–CSH, increasing the amount of C–S–H from 0 to 0.1 g (in 1 g Cry–CSH; 0 to 10% w/w C–S–H in gel precursor) showed increased %removal efficiency from 12.59 ± 2.34 to $94.19\pm0.18\%$ at 0.075 g C–S–H (7.5% w/w) and this remained constant after that (Fig. 32b). Thus, C–S–H was added to gel precursor for 7.5% to prepare Cry–CSH. It is worth noting that Cry (cryogel without C–S–H) could adsorb phosphate for $12.59\pm2.34\%$ due to the cross–linked Ca^{2+} in its structure.
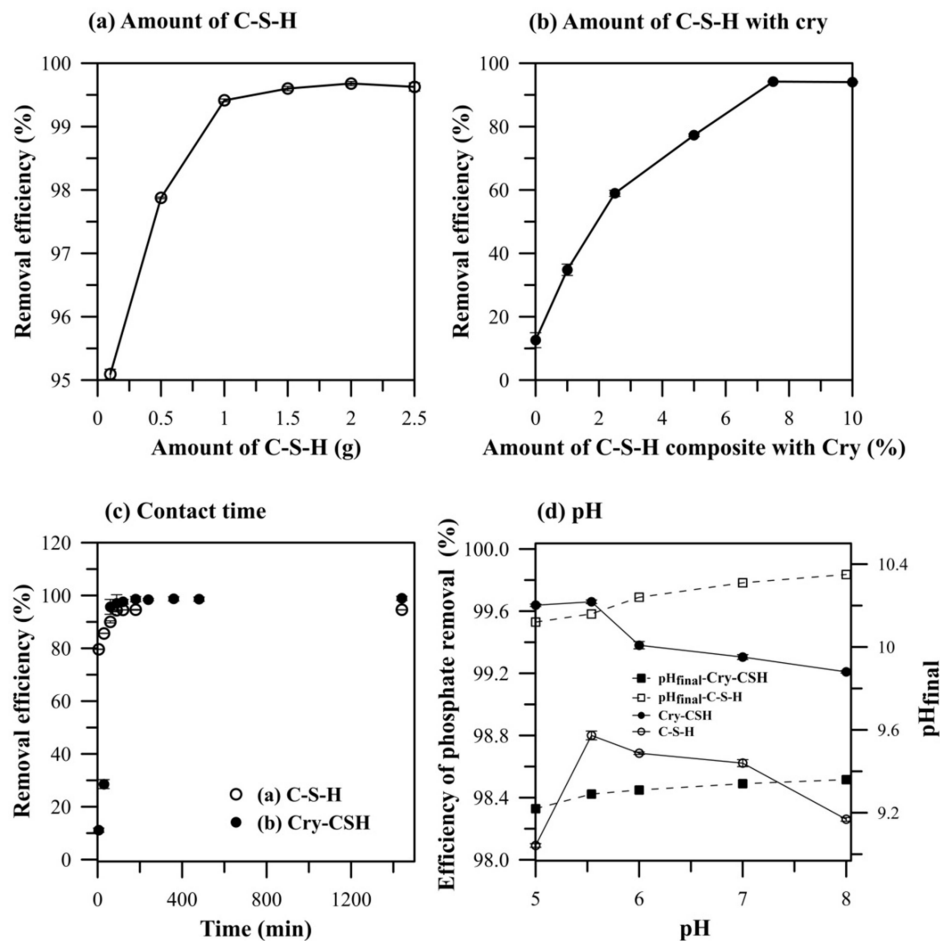
Figure 32 Influence of (a) amount of C–S–H, (b) amount of C–S–H in Cry–CSH, (c) contact time, and (d) pH on %removal efficiency.

2.2.4.1 Influence of contact time

The influence of adsorption time on phosphate removal efficiency is shown in Fig. 32c. It was found that C–S–H could adsorb phosphate with as high efficiency as 79.65±0.08% within 5 min and then increased to 94.42±0.14% within 90 min and remained constant after that. The results indicate rapid equilibration that can be attributed to the superior physicochemical adsorption of phosphate, as specific surface properties contribute to accelerated phosphate adsorption (Peng et al., 2018). In the case of Cry–CSH, it adsorbed phosphate slower than C–S–H. It could remove phosphate for 11.11±0.81% at 5 min and then increase to 95.69±2.81% at 60 min and

slightly increase further to 97.62±0.90% after 120 min. This may be because the cryogel matrix can decrease the reaction rate and thus prolong the equilibration time, as reported for PVA–CSH (Ding et al., 2018).

2.2.4.2 Influence of pH

Influence of pH on phosphate removal efficiency was investigated in the range from 5 to 8 (Fig. 32d). Slight decrease of removal efficiency was observed for both C–S–H and Cry–CSH with increasing pH that may relate to the charge on the material surfaces as well as to the physicochemical behavior of phosphate in water in this pH range. The point of zero charge (pH_{pzc}) was thus investigated based on the pH measurement technique (Khormaei et al., 2007; Pavan et al., 2014). The pH of sodium chloride (NaCl) solution (0.1 M) was adjusted to desired pH in the range of 3 to 12 using HCl (0.01 M) and NaOH (0.1 M). The adsorbent (0.03 g) was then added into pH adjusted NaCl solution (50 mL) and shaken for 24 h. The supernatant was then separated by centrifugation before measuring the final pH. The point where the curve pH final versus pH initial crosses the line and equals to pH final is the pH_{pzc} (Khormaei et al., 2007; Pavan et al., 2014). The study showed pH_{pzc} of C–S–H and Cry–CSH at 7.0 and 6.8, respectively (Fig. 33), indicating positive charge on the adsorbent surfaces when the pH of the phosphate solution is less than pH_{pzc} (Dai, 1994; Jun et al., 2020; Pavan et al., 2014). In addition, both Cry and Cry–CSH as the pH adjuster can release appropriate concentrations of OH^- to maintain the final pH between 9.2 and 10.4 regardless of initial pH and presence of Ca^{2+} on the surfaces. While the dominant phosphate anions at pH from 5 to 8 are $H_2PO_4^-$ and HPO_4^{2-}. Thus, higher phosphate removal efficiency was achieved at lower initial pH because the positively charged surfaces could attract the negatively charged phosphate ions electrostatically. However, removal efficiency of ~98.5% was achieved at pH ~6.5 which is a typical pH for an effluent.

Thus, there is no need for pH adjustment, which is a potential cost, in a real application. The removal efficiency of phosphate by Cry–CSH was compared with those reported in the literature as shown in Table 5.
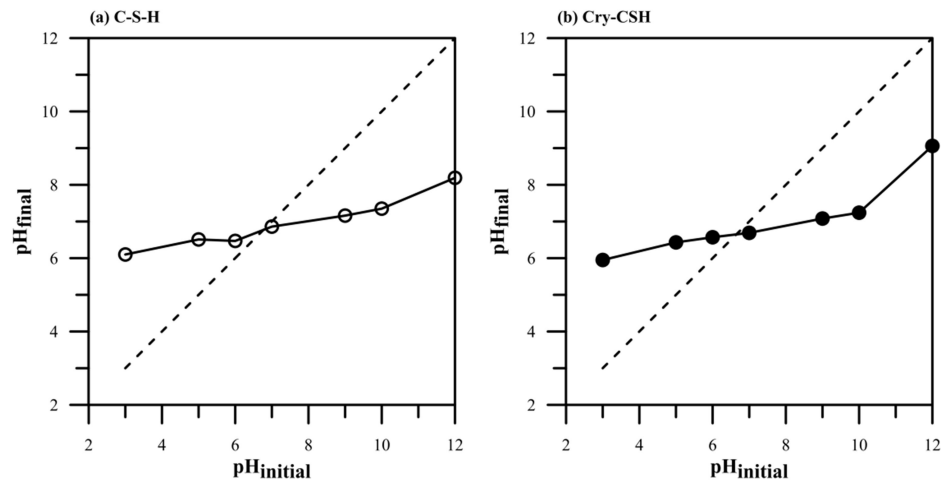
Figure 33 Point of zero charge (pH$_{pzc}$) of C–S–H and Cry–CSH.

Table 5 The phosphate removal capacities of various adsorbents.

Adsorbent	Removal capacity (mg PO$_4^{3-}$/g$_{active\ material}$)	pH	Time (min)	Temperature (K)	Reference
MCM-41	21.01	6.15	240	298	(Seliem et al., 2016)
CDC[*]	16.14	0.12	360	298	(Almanassra et al., 2020)
C–S–H	24.5	5.0	30	298	(Okano et al., 2013)
C–S–H	109.4	5.0	240	298	(Zhang et al., 2019)
PVA-CSH	28.15	7.50	600	298	(Ding et al., 2018)
Cry-CSH	64.52	5.54	120	298	This work

*Carbide derived carbon

2.2.4.3 Adsorption isotherms

Adsorption isotherms of C–S–H and Cry–CSH were determined at different initial phosphate concentrations (Fig. 34a–b). The two isotherm models typically used, i.e., Langmuir and Freundlich were adopted to fit and analyze the experimental data (Almanassra et al., 2020; Langmuir, 1918; Peng et al., 2018; Seliem et al., 2016). Langmuir isotherm equation can be written as in equations (7–8)

(Langmuir, 1918; Seliem et al., 2016) where C_e is the equilibrium concentration of the remaining phosphate in the solution (mgL^{-1}), Q_e is the amount of phosphate adsorbed per mass unit of the adsorbent at equilibrium (mgg^{-1}), Q_{max} is the amount of phosphate per mass unit of adsorbent at complete monolayer coverage (mgg^{-1}), and k_L is the Langmuir constant relating to the strength of adsorption (L^{-1}mg). Q_{max} and k_L can be determined from the slope and intercept of the linear plot between 1/Qe and 1/Ce, respectively. The Freundlich isotherm is expressed in equations (9–10) where k_F and n are the Freundlich constants related to adsorption capacity and intensity, respectively. The values of k_F and 1/n can be obtained from the intercept and slope of the linear regressions fit to log Q_e versus log C_e.

$$Q_e = \frac{Q_{max} k_L C_e}{1 + k_L C_e} \tag{7}$$

$$\frac{1}{Q_e} = \frac{1}{k_L Q_{max}} \left(\frac{1}{C_e} \right) + \frac{1}{Q_{max}} \tag{8}$$

$$Q_e = k_F C_e^{\frac{1}{n}} \tag{9}$$

$$\log Q_e = \log k_F + \frac{1}{n} \log C_e \tag{10}$$

Both nonlinear and linear fitting methods were applied and the goodness of equilibrium model fits in terms of the sum of the square of the errors (SSE), the residual standard deviation (SD), and the determination coefficient (R^2) (Almanassra et al., 2020) are listed in Table 6. The experimental results from C–S–H were fitted with the Langmuir model in its linearized form as in a previous report (Zhang et al., 2019). The R^2, SSE and SD values were best for nonlinearly fitted Freundlich model as in prior literature (Peng et al., 2018). These results imply that the adsorbed phosphate might form a monolayer surface coverage with possibly some heterogeneity on C–S–H (Almanassra et al., 2020) and chemisorption is the predominant adsorption mechanism (Peng et al., 2018). One of the important characteristics of Langmuir isotherm could be expressed by a dimensionless constant, known as the equilibrium parameter R_L (Almanassra et al., 2020; Seliem et al., 2016):

$$R_L= \frac{1}{1+K_L C_0} \tag{11}$$

where C_0 is the initial phosphate concentration. R_L from 0.08 to 0.99 were obtained for adsorption of phosphate on C–S–H indicating that the adsorption process is favorable, which confirms that the Langmuir model is suitable for the adsorption of phosphate on C–S–H.
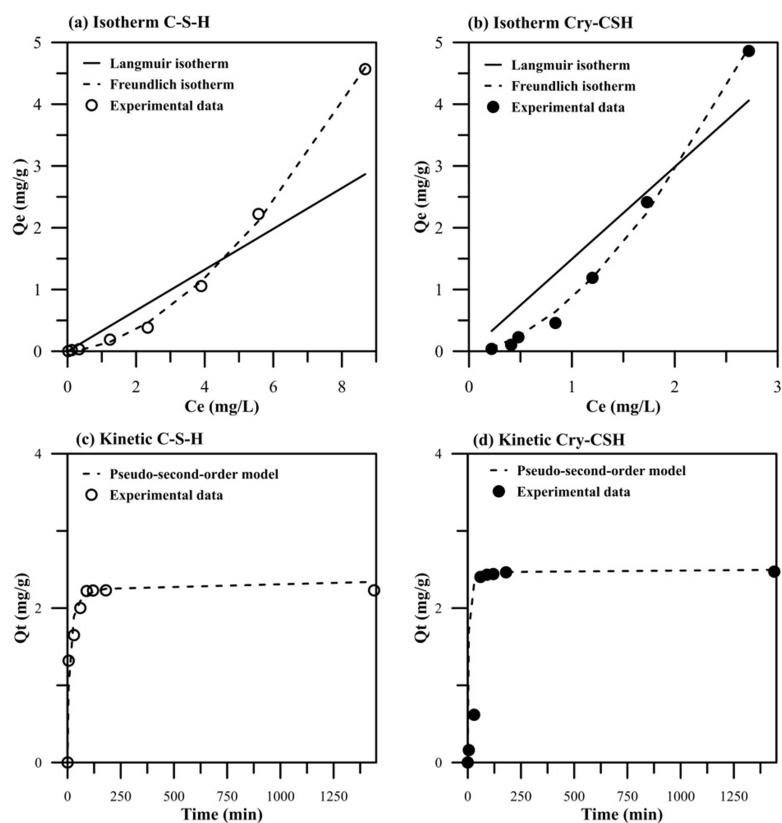
Figure 34 (a–b) Adsorption isotherms, and (c–d) adsorption kinetics of phosphate on C–S–H and Cry–CSH.

When C–S–H was composited with macroporous cryogel, Cry–CSH showed the best nonlinear fit with the Freundlich model, implying that the adsorption was multilayer type on heterogeneous surface. The heterogeneous factor $(1/n)$ related to adsorption intensity or surface heterogeneity was 1.78 implying that cooperative adsorption can be occurring among active sites with different adsorption capacities

(Liu, 2015; Madaeni and Salehi, 2009). This may be contributed by Ca^{2+} moiety in the cryogel structure combined with Ca^{2+} from composited C–S–H resulting in great heterogeneity. The adsorption of phosphate on Cry–CSH probably occurs on multilayers with Ca^{2+} moiety, in 1 both cryogel and C–S–H surface and surroundings, 2) Ca–OH linkages from C–S–H immobilized on Cry–CSH through ion exchange with OH^-, forming $Ca(H_2PO_4)_2$ and/or $CaHPO_4$.

Table 6 Phosphate adsorption and model parameters fit for C–S–H and Cry–CSH.

Model	Parameter	C–S–H		Cry-CSH	
		Linear	Non-linear	Linear	Non-linear
Langmuir	Q_m (mg PO_4^{3-}/g)	1.21	263830	-0.36	233552
	K_L (L/mgPO_4^{3-})	0.12	0.000001	-0.68	0.000006
	R^2	0.9980	0.8181	0.9596	0.7746
	SD	4.47	0.74	1.57	0.67
	SSE	120	3.29	12.40	2.25
Freundlich	K_F (mg^{1-n} L^n/g)	0.21	0.10	0.92	0.87
	1/n	1.20	1.75	1.78	1.73
	R^2	0.9740	0.9985	0.9912	0.9962
	SD	0.19	0.07	0.08	0.12
	SSE	0.21	0.03	0.03	0.07

2.2.4.4 Adsorption kinetics

Kinetics of phosphate removal were evaluated using three kinetic adsorption models, namely the Lagergren pseudo–first order (Sen Gupta and Bhattacharyya, 2011; Yuh-Shan, 2004) and the pseudo second–order (Ho, 2006; Sen Gupta and Bhattacharyya, 2011), and intra–particle diffusion (Seliem et al., 2016; Sen Gupta and Bhattacharyya, 2011), to determine the adsorption capacity and the rate limiting step. The obtained adsorption data were analyzed and fit with kinetic adsorption models. The Lagergren pseudo–first order model is expressed in equation

(12) which could be integrated for the boundary conditions $t = 0$, $Q_t = 0$ and $t = t$, $Q_t = Q_t$ to get equation (13):

$$\frac{dQt}{dt} = k_1(Q_e - Q_t) \tag{12}$$

$$\ln(Q_e - Q_t) = \ln Q_e - k_1 t \tag{13}$$

where Q_e and Q_t are the phosphate adsorbed ($mgPO_4^{3-}/g$) at equilibrium time (min) and at time t (min), respectively. The k_1 is the pseudo first–order kinetic rate constant (min^{-1}) which can be obtained from the slope of the linear plot between $\ln(Q_e - Q_t)$ and t. The pseudo second–order model is investigated on the basis of equation (14) which could be integrated for the boundary conditions $t = 0$, $Q_t = 0$ and $t = t$, $Q_t = Q_t$ as in equation (15), where k_2 is the second order kinetic rate constant (min^{-1}) which can be obtained from the slope of the linear plot between t/Q_t and t.

$$\frac{dQt}{dt} = k_2(Q_e - Q_t)^2 \tag{14}$$

$$\frac{t}{Q_t} = \frac{1}{k_2 Q_e^2} + \frac{1}{Q_e} t \tag{15}$$

The intra–particle diffusion can be estimated using equation (16) (Seliem et al., 2016; Sen Gupta and Bhattacharyya, 2011) where k_p is the rate constant of intra–particle diffusion ($mg/g/min^{1/2}$) that can be obtained from the slope of the plot of Q_t against $t^{1/2}$ and c is the intercept related to the thickness of the boundary layer. If the trend–line of the plot is linear and passes through the origin, intra–particle diffusion is the only rate controlling step (Almanassra et al., 2020; Seliem et al., 2016).

$$Q_t = k_p t^{1/2} + c \tag{16}$$

The adsorption of phosphate on C–S–H and Cry–CSH for 5 to 1440 min at 25 to 45°C is illustrated in Fig. 34c–d. These experimental results were fitted with pseudo–first–order and pseudo–second–order kinetic models and the model–based estimates of equilibrium are given in Table 7. Since the correlation coefficients

(R^2) of the pseudo–second–order model for both materials are quite close to 1.0 (0.9972 to 0.9995 for C–S–H and 0.9999 to 1.0000 for Cry–CSH), this model was the better one for describing the phosphate adsorption, indicating chemisorption. The k_2 for C–S–H increased from 0.06 to 0.20 g/mg/min and from 0.17 to 0.52 g/mg/min for Cry–CSH when increasing the temperature from 25°C to 45°C, indicating that the removal of phosphate by either material was endothermic. The kinetic parameters at 25°C were also estimated using the amount of C–S–H (0.075 g) immobilized in Cry–CSH (1 g) and Qe = 64.52 mgPO$_4^{3-}$/g$_{CSH}$, k_2 = 0.0007 g$_{CSH}$/mgPO$_4^{3-}$/min, R^2 = 0.997 were obtained. It can be noted that k_2 for C–S–H (0.06 g$_{CSH}$/mgPO$_4^{3-}$/min) was much higher than that of C–S–H in Cry–CSH (0.0007 g$_{CSH}$/mgPO$_4^{3-}$/min), maybe because the cryogel matrix decreased the reaction rate and prolonged the equilibration time. This estimated k_2 value was lower than those reported for PVA–CSH (0.0008 g/mg/min) (Ding et al., 2018), which may be due to the smaller pore size of Cry–CSH (0.97 nm compared to 24.937 nm) (Ding et al., 2018). However, the estimated Qe of C–S–H in Cry–CSH was 64.52 mgPO$_4^{3-}$/g$_{CSH,}$ higher than that reported for PVA–CSH (28.15 mg/g$_{CSH}$) (Ding et al., 2018) due to the larger specific surface area of Cry–CSH (11.03 m^{2}g^{-1} compared to 4.123 m^{2}g^{-1}) (Ding et al., 2018).

The half–life ($t_{1/2}$) of adsorption is the time needed to adsorb 50% of the adsorbed phosphate at equilibrium (Almanassra et al., 2020) was also estimated using equation (17). The half–life of adsorption by C–S–H decreased from 7.12 min at 25°C to 2.09 min at 45 °C, and from 2.36 min at 25°C to 0.77 min at 45°C for Cry–CSH, confirming the faster adsorption kinetics at elevated temperatures.

$$t_{1/2} = \frac{1}{k_2 Q_e} \tag{17}$$

Since the adsorption process relates to transport of phosphate ions from the aqueous solution to the surfaces of C–S–H and Cry–CSH, possibly followed by intra–particle diffusion, the intra–particle diffusion based kinetic model was also investigated to obtain better knowledge of the adsorption mechanisms. The plot shown in Fig. 35 is not linear and does not pass through the origin, indicating that more than one step controls the adsorption process. The first steep slope is associated

with the diffusion of phosphate ions from solution across the boundary layer surrounding C–S–H and Cry–CSH to the external surface of the adsorbent. The second stage shows a plateau, indicating slow adsorption with intra–particle diffusion dominating during this stage. In addition, the c for both materials increased with temperature (from 1.21 to 2.21 mg/g for C–S–H and from 1.32 to 2.38 mg/g for Cry–CSH) implying improved adsorption process with increased mobility of the ions, from decreases in both of solution density and viscosity as temperature is increased (Almanassra et al., 2020)

Table 7 Kinetic parameters for phosphate adsorption by C–S–H and Cry–CSH.

Model	Temperature	Parameter	C–S–H	Cry-CSH
Pseudo-first-order	25	Q_e (mg/g)	1.07	1.34
		k_1 (min^{-1})	0.0075	0.018
		R^2	0.9673	0.8562
	35	Q_e (mg/g)	1.09	0.70
		k_1 (min^{-1})	0.024	0.011
		R^2	0.8785	0.9305
	45	Q_e (mg/g)	0.98	0.73
		k_1 (min^{-1})	0.0275	0.026
		R^2	0.7952	1.0000
Pseudo-second-order	25	Q_e (mg/g)	2.34	2.50
		k_2 (g/mg/min)	0.06	0.17
		R^2	0.9972	1.000
	35	Q_e (mg/g)	2.42	2.49
		k_2 (g/mg/min)	0.12	0.26
		R^2	0.9995	0.9999
	45	Q_e (mg/g)	2.39	2.48
		k_2 (g/mg/min)	0.20	0.52
		R^2	0.9995	1.0000

Figure 35 Intra–particle diffusion model for phosphate adsorption on C–S–H and Cry–CSH.

2.2.4.5 Thermodynamic analysis

The thermodynamics of phosphate adsorption on C–S–H and Cry–CSH were investigated over the temperature range from 25 to 45°C to study the effects of temperature on the adsorption and to estimate the changes of thermodynamic factors including Gibbs free energy (ΔG^0), enthalpy (ΔH^0), and entropy (ΔS^0). ΔG^0 can explain the spontaneity and feasibility of the removal process and can be determined from the classical Van't Hoff equation at any temperature (18):

$$\Delta G^0 = -RT \ln k_d \tag{18}$$

where T is the temperature (K), R is the gas constant (8.314 J/mol/K), and k_d is the constant of thermodynamic equilibrium that can be calculated using equation (19):

$$k_d = \frac{C_a}{C_e} \tag{19}$$

where C_a is the extent of pollutant adsorbed on the adsorbent at saturation (mgL^{-1}). ΔH^0 provides information about the nature of adsorption process, whether it is exothermic or endothermic, while ΔS^0 can explain the degrees of freedom in the

system or the extent of order/disorder of the molecules (Almanassra et al., 2020). Both ΔH^0 and ΔS^0 are linked to ΔG^0 by equation (20):

$$\Delta G^0 = \Delta H^0 - T\Delta S^0 \tag{20}$$

when equations (9) and (18) are combined, ΔH^0 and ΔS^0 are obtained from the slope and the intercept as in equation (21):

$$\ln k_d = \frac{\Delta S^0}{R} - \frac{\Delta H^0}{R}\left(\frac{1}{T}\right) \tag{21}$$

Thermodynamic analysis including the activation energy (E_a) of phosphate adsorption was estimated for both C–S–H and Cry–CSH using equation (22) (Almanassra et al., 2020):

$$\ln k_2 = \ln k_0 - \frac{E_a}{RT} \tag{22}$$

where E_a is the activation energy in kJ/mol, k_2 is the pseudo–second–order kinetic constant calculated from the kinetic data at each temperature, and k_0 is a factor independent of temperature. The E_a estimates of 47.5 and 43.9 kJ/mol were obtained for adsorption of phosphate on C–S–H and Cry–CSH, respectively. Since E_a is more than 40 kJ/ mol, the adsorption mechanism on both materials is chemical adsorption (E_a < 40 kJ/mol for physical adsorption (Almanassra et al., 2020)

The thermodynamic differences ΔG^0, ΔH^0, and ΔS^0 for phosphate adsorption on C–S–H and Cry–CSH are presented in Table 8. The negative values of ΔG^0 across the tested temperatures indicate spontaneous adsorption of phosphate on both materials under the experimental conditions, and more favorable adsorption at a higher temperature. The spontaneity of Cry–CSH seems to be higher than of C–S–H. The positive ΔH^0 indicates endothermic phosphate adsorption. ΔS^0 for both C–S–H and Cry–CSH were positive, indicating increased disorder at the solid–solution interface during the adsorption process, and the disorder degree on C–S–H seems to

be higher than of Cry–CSH. The disordered state in both materials is mostly due to the interaction of phosphate with active sites of the adsorbents to form stable structures. These results demonstrate the strong affinity between phosphate and the prepared materials.

Table 8 Thermodynamic parameters for phosphate adsorption by C–S–H and Cry–CSH.

Temperature (K)	$\Delta G°$ (kJ/mol)		$\Delta H°$ (kJ/mol)		$\Delta S°$ (J/mol/K)	
	C–S–H	Cry-CSH	C–S–H	Cry-CSH	C–S–H	Cry-CSH
298	-5.22	-10.42	31.8	19.3	125.3	99.89
308	-7.33	-11.55				
318	-7.68	-12.42				

2.2.5 Influence of competing ions on removal efficiency of Cry–CSH

The influences of various co–exist anions, namely SO_4^{2-}, NO_3^-, NO_2^-, Br^-, F^-, and CO_3^{2-}, on removal efficiency of phosphate by Cry–CSH were investigated. Various competing anions (at 2000 mgL^{-1}) except for CO_3^{2-} were mixed with phosphate (50 mgL^{-1}) in order to determine the selectivity for phosphate. Carbonate (500 and 2000 mgL^{-1}), which has been reported to interfere with phosphate adsorption (Seliem et al., 2016; Zhang et al., 2019), was also mixed with phosphate but separately from the other anions. The removal efficiency of phosphate remained 99.17±0.01% with mixed anions (Fig. 36) indicating excellent selectivity of Cry–CSH for phosphate, better than those of other adsorbents such as carbide derived carbon (Almanassra et al., 2020), or MCM–41 silica with rice husk (Seliem et al., 2016). The removal efficiency of phosphate slightly decreased to 95.35±0.01% when concentration of CO_3^{2-} was 10–fold higher than that of phosphate (500 mgL^{-1}), but

decreased to 55.02±0.82% at 2000 mgL^{-1}. The results show that Cry–CSH is highly selective for phosphate ions and can be applied in phosphate removal and recovery.
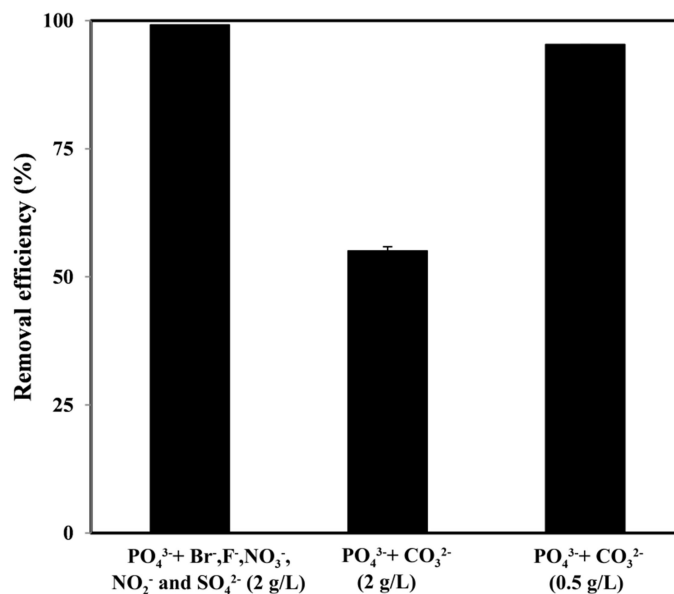
Figure 36 The removal efficiency of phosphate in the presence of various competing ions.

2.2.6 Real sample application of Cry–CSH

The Cry–CSH was tested for phosphate removal from 2 wastewater and 3 effluent samples from the municipal treatment plant in Patong, Phuket. Orthophosphate presented in the samples in the range from 0.93 to 4.05 mgL^{-1} which exceed the concentration level of phosphate that is considered to cause eutrophication of water bodies (>0.02 mgL^{-1}) (Seliem et al., 2016). Concentrations from 0.005 to 0.014 mgL^{-1} were found after adsorption of phosphate using 2 g Cry–CSH, indicating removal efficiencies from 98.6% to 99.8% (Table 9).

Table 9   Real sample tests.

Sample	Type of sample	Before (mgL^{-1} PO$_4^{3-}$)	After (mgL^{-1} PO$_4^{3-}$)	Removal efficiency (%)
1*	Wastewater	4.05±0.04	0.010±0.004	99.8±0.1
2	Wasterwater	1.01±0.03	0.014±0.004	98.6±0.6
3*	Effluent	1.79±0.12	0.005±0.008	99.7±0.4
4	Effluent	0.93±0.02	0.009±0.004	99.0±0.4
5	Effluent	0.96±0.01	0.009±0.004	99.0±0.4

*Samples were collected in December 2019 before Covid–19 pandemic, and there were ~14.4 M tourists that visited Phuket during that year.

2.2.7 Biodegradation of Cry–CSH

Biodegradation of the Cry–CSH and phosphate adsorbed Cry–CSH (PO$_4^{3-}$–Cry–CSH) were investigated using a soil burial test (Junlapong et al., 2020). Swollen Cry–CSHs and PO$_4^{3-}$–Cry–CSH were buried at 10 cm depth under the surface of soil. They were taken out every 3 days and washed thoroughly to remove the soil as much as possible before weighing the remaining weight (W_b). The percentage of weight remaining was calculated using equation (23) where W_e is the weights of the swollen Cry–CSHs and W_b is the weights of Cry–CSHs after soil burial.

$$\text{Weight remaining (\%)} = 100 \times \frac{W_b}{W_e} \tag{23}$$

After having been buried for three days, the Cry–CSH weight loss was 100%, while phosphate adsorbed Cry–CSH remained for 37.8±1.2% by weight. The latter was completely lost after burial in the soil for 10 days, due to hydrolysis and microorganisms (Junlapong et al., 2020).

3. Concluding remarks

This thesis aimed to develop novel materials for environmental applications, especially for the detection and removal of nutrients in water sample. For the first part of the work, a novel colorimetric thin sheet for nitrite detection was successfully developed based on Griess reagent adsorption on mesoporous silica nanoparticles. The spherical nanoparticles from which the colorimetric sheet was developed retained their shape after the Griess reagent adsorption, but there was a rough surface, and some disorder of the long range–ordered hexagonal pores. The Griess reagent appears to absorb mesoporous silica nanoparticles with both physical and chemical absorption. Both nanoparticle form and the nanoparticle sheet form made by binding with a starch solution that the Griess–adsorbed nanoparticles for colorimetric testing of nitrite. The colorimetric thin sheet rapidly time to change from white to red–violet within 3 min at pH 6 without any interference from other common ions, as well as a seawater matrix. The developed sheet was used together with DIC for quantitative analysis of nitrite to allow rapid on–site. This colorimetric sensor provided high sensitivity, rapid response, good selectivity, high accuracy and high precision, which presented a wide linear range (0.05 to 2.50 mg L^{-1}) with a low detection limit (15.0 μg L^{-1}–NO_2^-), good inter–day precision (1.93%RSD), and excellent accuracy (2.67% relative error). Application of the method developed for nitrite detection in seawater samples collected in Phuket. There is a good correlation with results obtained from the standard method (spectrophotometry). The colorimetric sheet developed can be produced at a cost effective (USD 0.04 per sensor), while standard smartphone can conduct using a camera for DIC. Therefore, the method developed in this work can be applied to the monitoring of nitrite analysis in water that a much easier, cheaper, and rapid.

For the second part of the work, a novel calcium silicate hydrate composite starch cryogel for phosphate removal and recovery. The natural gel precursor prepared from rice flour, tapioca starch, and limewater (saturated calcium hydroxide solution as the cross–linker) was mixed with C–S–H at 7.5% w/w.

The OH groups in starch molecules interact with Ca^{2+} ions in limewater with alkaline conditions by physical cross–linking via van der Waals interactions, while C–S–H attached to available OH groups in the starch network. The gel after gelatinization was then frozen (–18°C, 24 h) and thawed (at room temperature) for 3 cycles providing an interconnected macroporous composite with sponge–like structure. This had the C–S–H nanoparticles immobilized in a floatable monolithic starch cryogel network, resulting in much easier adsorbent recovery without loss. Phosphate ion presented in an aqueous phase (pH ~5.5) can be eliminated using Cry–CSH, as it reacts with Ca^{2+} and/or Ca–OH linkages on C–S–H and $Ca(H_2PO_4)_2$ and/or $CaHPO_4$ were shown on cryogel surface forming. The equilibrium of phosphate adsorption was found at 120 min. The optimum conditions represented adsorption capacity of 2.50 $mgPO_4^{3-}/g_{Cry-CSH}$ (64.52 $mgPO_4^{3-}/g_{C–S–H}$) respectively. The phosphate removal by Cry–CSH described well fit with the Freundlich isotherm model, while adsorption kinetic data results were well fit with the pseudo second–order model. The thermodynamic was calculated by activation energy (E_a) of 43.9 kJ/mol indicated chemical adsorption, while a positive enthalpy change (ΔH^0, 19.3 kJ/mol) indicated the endothermic nature of phosphate adsorption. Cry–CSH can float on aqueous surface for passive phosphate adsorption for at least 105 days without damage. Cry–CSH was removed phosphate in real samples from wastewater and effluent samples with high removal efficiency (> 98%). After adsorption, Cry–CSH was biodegraded within 10 days when buried in soil, which, can be further directly used as a fertilizer in agriculture. Thus, the work has demonstrated the significant potential of Cry–CSH for practical and environmentally friendly phosphate removal and recovery.

As Phuket and many regions of Thailand are facing with the problem involving the increasing of nutrients in aquatic ecosystems due to various anthropogenic activities leading to deterioration of the ecosystem and can accelerate eutrophication, the development of colorimetric sensor for on–site detection of nitrite would thus be benefit to Thailand as such pollutant would be rapidly detected with simple and accurate colorimetric test kit. That is, anyone can apply the developed test kit for monitoring the environmental pollutant that could help the government officers to look after the environmental situation. The development of bio–adsorbent for removal of nutrients in water samples is also benefit to Thailand to reduce

contaminated nutrient in water. Since bio–adsorbent developed in this work could biodegrade in soil, the nutrient adsorbed bio–adsorbent could be further used as fertilizer.

References

Almanassra, I.W., Kochkodan, V., Subeh, M., McKay, G., Atieh, M. and Al-Ansari, T., 2020. Phosphate removal from synthetic and treated sewage effluent by carbide derive carbon. Journal of Water Process Engineering. 36, 101323.

Almanassra, I.W., McKay, G., Kochkodan, V., Ali Atieh, M. and Al-Ansari, T., 2021. A state of the art review on phosphate removal from water by biochars. Chemical Engineering Journal. 409, 128211.

Aydın, A., Ercan, Ö. and Taşcıoğlu, S., 2005. A novel method for the spectrophotometric determination of nitrite in water. Talanta. 66, 1181-1186.

Bajpai, A.K. and Shrivastava, M., 2002. Swelling kinetics of a hydrogel of poly(ethylene glycol) and poly(acrylamide-co-styrene). Journal of Applied Polymer Science. 85, 1419-1428.

Bartsch, H., 1991. N-nitroso compounds and human cancer: where do we stand? IARC Sci Publ. 1-10.

Baudron, V., Gurikov, P., Smirnova, I. and Whitehouse, S., 2019. Porous Starch Materials via Supercritical- and Freeze-Drying. Gels. 5.

Beaton, A.D., Sieben, V.J., Floquet, C.F.A., Waugh, E.M., Abi Kaed Bey, S., Ogilvie, I.R.G., Mowlem, M.C. and Morgan, H., 2011. An automated microfluidic colourimetric sensor applied in situ to determine nitrite concentration. Sensors and Actuators B: Chemical. 156, 1009-1014.

Boonkanon, C., Phatthanawiwat, K., Wongniramaikul, W. and Choodum, A., 2020. Curcumin nanoparticle doped starch thin film as a green colorimetric sensor for detection of boron. Spectrochimica Acta Part A: Molecular and Biomolecular Spectroscopy. 224, 117351.

Boos, A., Intasiri, A., Brunette, J.-P. and Leroy, M., 2002. Surfactant-templated silica doped with 1-phenyl-3-methyl-4-stearoylpyrazol-5-one (HPMSP) as a new sorbent. Journal of Materials Chemistry - J MATER CHEM. 12, 886-889.

Bryant, C.M. and Hamaker, B.R., 1997. Effect of Lime on Gelatinization of Corn Flour and Starch. Cereal Chemistry. 74, 171-175.

Butt, S.B., Riaz, M. and Iqbal, M.Z., 2001. Simultaneous determination of nitrite and nitrate by normal phase ion-pair liquid chromatography. Talanta. 55, 789-797.

Chanjarujit, W., Hongsprabhas, P. and Chaiseri, S., 2018. Physicochemical properties and flavor retention ability of alkaline calcium hydroxide-mungbean starch films. Carbohydrate Polymers. 198, 473-480.

Chen, X., Kong, H., Wu, D., Wang, X. and Lin, Y., 2009. Phosphate removal and recovery through crystallization of hydroxyapatite using xonotlite as seed crystal. Journal of Environmental Sciences. 21, 575-580.

Choodum, A., Boonsamran, P., NicDaeid, N. and Wongniramaikul, W., 2015. On-site semi-quantitative analysis for ammonium nitrate detection using digital image colourimetry. Science & Justice. 55, 437-445.

Choodum, A., Kanatharana, P., Wongniramaikul, W. and Daéid, N., 2013. Using the iPhone as a device for a rapid quantitative analysis of trinitrotoluene in soil. Talanta. 115, 143–149.

Choodum, A., Kanatharana, P., Wongniramaikul, W. and NicDaeid, N., 2016. Poly vinyl alcohol cryogel as a selective test kit for pre and post blast trinitrotoluene. Sensors and Actuators B: Chemical. 222, 654-662.

Choodum, A., Keson, J., Kanatharana, P., Limsakul, W. and Wongniramaikul, W., 2017. Selective pre and post blast trinitrotoluene detection with a novel ethylenediamine entrapped thin polymer film and digital image colorimetry. Sensors and Actuators B: Chemical. 252, 463-469.

Choodum, A., Sriprom, W. and Wongniramaikul, W., 2019. Portable and selective colorimetric film and digital image colorimetry for detection of iron. Spectrochimica Acta Part A: Molecular and Biomolecular Spectroscopy. 208, 40-47.

Cornejo-Villegas, M.d.l.Á., Rincón-Londoño, N., Del Real-López, A. and Rodríguez-García, M.E., 2018. The effect of Ca2+ ions on the pasting, morphological, structural, vibrational, and mechanical properties of corn starch–water system. Journal of Cereal Science. 79, 174-182.

Cui, Z., 2011. Medical Biothechnology and Health Care. Comprehensive Biotechnology.

Da'na, E., 2017. Adsorption of heavy metals on functionalized-mesoporous silica: A review. Microporous and Mesoporous Materials. 247, 145-157.

Dai, M., 1994. The Effect of Zeta Potential of Activated Carbon on the Adsorption of Dyes from Aqueous Solution: I. The Adsorption of Cationic Dyes: Methyl Green and Methyl Violet. Journal of Colloid and Interface Science. 164, 223-228.

Danzer, K. and Currie, L.A., 1998. Guidelines for calibration in analytical chemistry. Part I. Fundamentals and single component calibration (IUPAC Recommendations 1998). Pure and Applied Chemistry. 70, 993-1014.

Diagboya, P. and Dikio, E., 2018. Silica-based mesoporous materials; emerging designer adsorbents for aqueous pollutants removal and water treatment. Microporous and Mesoporous Materials. 266, 252-267.

Ding, S., Fang, D., Pang, Z., Luo, B., Kuang, L., Wang, H., Zhang, Q., Shen, Q. and Ji, F., 2018. Immobilization of powdery calcium silicate hydrate via PVA covalent cross-linking process for phosphorus removal. Science of The Total Environment. 645, 937-945.

Domene-López, D., García-Quesada, J.C., Martin-Gullon, I. and Montalbán, M.G., 2019. Influence of Starch Composition and Molecular Weight on Physicochemical Properties of Biodegradable Films. Polymers. 11, 1084.

Ertürk, G. and Mattiasson, B., 2014. Cryogels-versatile tools in bioseparation. Journal of Chromatography A. 1357, 24-35.

Ferreira Soares, D.C., de Sousa Andrada, A. and Andrade Ramaldes, G., 2015. Silica Nanoparticles Containing Gadolinium Complex as Potential Alternative to Anticancer Radiotherapy. Particulate Science and Technology. 33, 331-338.

Fotoohi, B., Kazemzad, M. and Mercier, L., 2018. Additive-free synthesis of robust monolithic mesoporous silica support used in catalysis. Ceramics International. 44.

Franceschini, A., Abramson, S., Mancini, V., Bresson, B., Chassenieux, C. and Lequeux, N., 2007. New covalent bonded polymer–calcium silicate hydrate composites. Journal of Materials Chemistry. 17, 913-922.

García-Lodeiro, I., Fernández-Jiménez, A., Blanco, M.T. and Palomo, A., 2008. FTIR study of the sol–gel synthesis of cementitious gels: C–S–H and N–A–S–H. Journal of Sol-Gel Science and Technology. 45, 63-72.

Guan, W., Ji, F., Chen, Q., Yan, P. and Zhang, Q., 2013. Preparation and phosphorus recovery performance of porous calcium–silicate–hydrate. Ceramics International. 39, 1385-1391.

Guan, W. and Zhao, X., 2016. Fluoride recovery using porous calcium silicate hydrates via spontaneous Ca2+ and OH− release. Separation and Purification Technology. 165, 71-77.

Gupta, N.V. and Shivakumar, H.G., 2012. Investigation of Swelling Behavior and Mechanical Properties of a pH-Sensitive Superporous Hydrogel Composite. Iranian journal of pharmaceutical research : IJPR. 11, 481-493.

Hattori, Y., Kaneko, K. and Ohba, T., 2013. 5.02 - Adsorption Properties, in: Reedijk, J. and Poeppelmeier, K. Eds.), Comprehensive Inorganic Chemistry II (Second Edition). Elsevier, Amsterdam, pp. 25-44.

Hegesh, E. and Shiloah, J., 1982. Blood nitrates and infantile methemoglobinemia. Clin Chim Acta. 125, 107-15.

Ho, Y.-S., 2006. Review of second-order models for adsorption systems. Journal of Hazardous Materials. 136, 681-689.

Hoang Thi, T.T., Cao, V.D., Nguyen, T.N.Q., Hoang, D.T., Ngo, V.C. and Nguyen, D.H., 2019. Functionalized mesoporous silica nanoparticles and biomedical applications. Materials Science and Engineering: C. 99, 631-656.

Honikel, K., 2008. The use and control of nitrate and nitrite for the processing of meat products. Meat science. 78 1-2, 68-76.

Huong, P.T., Jitae, K., Giang, B.L., Nguyen, T.D. and Thang, P.Q., 2019. Novel lanthanum-modified activated carbon derived from pine cone biomass as ecofriendly bio-sorbent for removal of phosphate and nitrate in wastewater. Rendiconti Lincei. Scienze Fisiche e Naturali. 30, 637-647.

Indyk, H. and Woollard, D., 2011. Contaminants of Milk and Dairy Products | Nitrates and Nitrites as Contaminants. pp. 906-911.

Ishio, N., Fukushi, K., Michiba, K., Takeda, S. and Wakida, S., 2002. Optimum conditions for effective use of the terminating ion in transient isotachophoresis

for capillary zone electrophoretic determination of nitrite and nitrate in seawater, with artificial seawater as background electrolyte. Anal Bioanal Chem. 374, 1165-9.

Israkarn, K. and Hongsprabhas, P., 2017. Effect of CaCl2 on the formation of Ca-induced starch aggregates and spherulitic structure in dried starch film. Drying Technology. 35, 1552-1560.

Israkarn, K., Hongsprabhas, P. and Hongsprabhas, P., 2007. Influences of granule-associated proteins on physicochemical properties of mungbean and cassava starches. Carbohydrate Polymers. 68, 314-322.

Jaroniec, M., 2006. Design, synthesis and characterization of ordered mesoporous materials for environmental applications. pp. 23-36.

Jayaramudu, T., Ko, H.-U., Kim, H.C., Kim, J.W. and Kim, J., 2019. Swelling Behavior of Polyacrylamide-Cellulose Nanocrystal Hydrogels: Swelling Kinetics, Temperature, and pH Effects. Materials (Basel, Switzerland). 12.

Jensen, F., 2003. Nitrite disrupts multiple physiological functions aquatic animals. Comparative biochemistry and physiology. Part A, Molecular & integrative physiology. 135, 9-24.

Jun, B.-M., Cho, J., Jang, A., Chon, K., Westerhoff, P., Yoon, Y. and Rho, H., 2020. Charge characteristics (surface charge vs. zeta potential) of membrane surfaces to assess the salt rejection behavior of nanofiltration membranes. Separation and Purification Technology. 247, 117026.

Junlapong, K., Maijan, P., Chaibundit, C. and Chantarak, S., 2020. Effective adsorption of methylene blue by biodegradable superabsorbent cassava starch-based hydrogel. International Journal of Biological Macromolecules. 158, 258-264.

Kachbouri, S., Mnasri, N., Elaloui, E. and Moussaoui, Y., 2018. Tuning particle morphology of mesoporous silica nanoparticles for adsorption of dyes from aqueous solution. Journal of Saudi Chemical Society. 22, 405-415.

Khan, A.J., Song, J., Ahmed, K., Rahim, A., Onófrio Volpe, P.L. and Rehman, F., 2020. Mesoporous silica MCM-41, SBA-15 and derived bridged polysilsesquioxane SBA-PMDA for the selective removal of textile reactive dyes from wastewater. Journal of Molecular Liquids. 298, 111957.

Khormaei, M., Nasernejad, B., Edrisi, M. and Eslamzadeh, T., 2007. Copper biosorption from aqueous solutions by sour orange residue. Journal of Hazardous Materials. 149, 269-274.

Knobeloch, L., Salna, B., Hogan, A., Postle, J. and Anderson, H., 2000. Blue babies and nitrate-contaminated well water. Environmental health perspectives. 108, 675-678.

Kodamatani, H., Yamazaki, S., Saito, K., Tomiyasu, T. and Komatsu, Y., 2009. Selective determination method for measurement of nitrite and nitrate in water samples using high-performance liquid chromatography with post-column photochemical reaction and chemiluminescence detection. J Chromatogr A. 1216, 3163-7.

Lahtinen, M., Kudva, J., Hegde, P., Bhat, K., Kolehmainen, E., Nonappa, Venkatesh and Naral, D., 2014. Synthesis, Characterization, Thermal and Antimicrobial studies of N-substituted Sulfanilamide derivatives. Journal of Molecular Structure. 1060, 280-290.

Langmuir, I., 1918. THE ADSORPTION OF GASES ON PLANE SURFACES OF GLASS, MICA AND PLATINUM. Journal of the American Chemical Society. 40, 1361-1403.

Lee, C.-G., Alvarez, P.J.J., Kim, H.-G., Jeong, S., Lee, S., Lee, K.B., Lee, S.-H. and Choi, J.-W., 2018. Phosphorous recovery from sewage sludge using calcium silicate hydrates. Chemosphere. 193, 1087-1093.

Li, H., Du, T., Xiao, H. and Zhang, Q., 2017. Crystallization of calcium silicate hydrates on the surface of nanomaterials. Journal of the American Ceramic Society. 100, 3227-3238.

Li, W., Zhang, R., Wang, H., Jiang, W., Wang, L., Li, H., Wu, T. and Du, Y., 2016. Digital image colorimetry coupled with a multichannel membrane filtration-enrichment technique to detect low concentration dyes. Analytical Methods. 8, 2887-2894.

Li, Y., Yang, Q. and Yang, J., 2006. Mesoporous alumino silicates synthesized with single molecular precursor (sec-BUO)(2)AlOSi(OEt)(3) as aluminum source. Microporous and Mesoporous Materials - MICROPOROUS MESOPOROUS MAT. 91, 85-91.

Lin, T.-W. and Hsu, S.-h., 2020. Self-Healing Hydrogels and Cryogels from Biodegradable Polyurethane Nanoparticle Crosslinked Chitosan. Advanced Science. 7, 1901388.

Lin, Z., Xue, W., Chen, H. and Lin, J.-M., 2011. Peroxynitrous-Acid-Induced Chemiluminescence of Fluorescent Carbon Dots for Nitrite Sensing. Analytical Chemistry. 83, 8245-8251.

Liu, S., 2015. Cooperative adsorption on solid surfaces. Journal of Colloid and Interface Science. 450, 224-238.

Lozinsky, V., 2008. Polymeric cryogels as a new family of macroporous and supermacroporous materials for biotechnological purposes. Russian Chemical Bulletin. 57, 1015-1032.

Ls, M., 2019. Interactions of Mesoporous Silica and Zno Nanoparticles with Escherichia Coli. Advances in Biotechnology & Microbiology. 12.

Lundberg, J.O., Weitzberg, E., Cole, J.A. and Benjamin, N., 2004. Nitrate, bacteria and human health. Nature Reviews Microbiology. 2, 593-602.

Madaeni, S.S. and Salehi, E., 2009. Adsorption of cations on nanofiltration membrane: Separation mechanism, isotherm confirmation and thermodynamic analysis. Chemical Engineering Journal. 150, 114-121.

Maeda, H., Yokota, S. and Kasuga, T., 2018. Structural changes in calcium silicate hydrate gel and resulting improvement in phosphate species removal properties after mechanochemical treatment. Royal Society Open Science. 5, 181403.

Mattiasson, B., Kumar, A. and Galeaev, I.Y. (Eds.) 2009, Macroporous Polymers: Production Properties and Biotechnological/Biomedical Applications, 1st ed. CRC Press.

Mehmeti, E., Stanković, D., Hajrizi, A. and Kalcher, K., 2016. The use of graphene nanoribbons as efficient electrochemical sensing material for nitrite determination. Talanta. 159, 34-39.

Mezenner, N.Y. and Bensmaili, A., 2009. Kinetics and thermodynamic study of phosphate adsorption on iron hydroxide-eggshell waste. Chemical Engineering Journal. 147, 87-96.

Murthy, P.S.K., Mohan, Y.M., Sreeramulu, J. and Raju, K.M., 2006. Semi-IPNs of starch and poly(acrylamide-co-sodium methacrylate): Preparation, swelling and diffusion characteristics evaluation. Reactive and Functional Polymers. 66, 1482-1493.

Nakanishi, K., Tomita, M. and Kato, K., 2015. Synthesis of amino-functionalized mesoporous silica sheets and their application for metal ion capture. Journal of Asian Ceramic Societies. 3, 70-76.

Nam, J., Jung, I.-B., Kim, B., Lee, S.-M., Kim, S.-E., Lee, K.-N. and Shin, D.-S., 2018. A colorimetric hydrogel biosensor for rapid detection of nitrite ions. Sensors and Actuators B: Chemical. 270, 112-118.

Okano, K., Miyamaru, S., Kitao, A., Takano, H., Aketo, T., Toda, M., Honda, K. and Ohtake, H., 2015. Amorphous calcium silicate hydrates and their possible mechanism for recovering phosphate from wastewater. Separation and Purification Technology. 144, 63-69.

Okano, K., Miyamaru, S., Yamamoto, Y., Kunisada, M., Takano, H., Toda, M., Honda, K. and Ohtake, H., 2016. A mobile pilot-scale plant for in situ demonstration of phosphorus recovery from wastewater using amorphous calcium silicate hydrates. Separation and Purification Technology. 170, 116-121.

Okano, K., Uemoto, M., Kagami, J., Miura, K., Aketo, T., Toda, M., Honda, K. and Ohtake, H., 2013. Novel technique for phosphorus recovery from aqueous solutions using amorphous calcium silicate hydrates (A-CSHs). Water Research. 47, 2251-2259.

Pasquali, C.E., Gallego-Picó, A., Hernando, P., Velasco, M. and Alegría, J.S., 2010. Two rapid and sensitive automated methods for the determination of nitrite and nitrate in soil samples. Microchemical Journal. 94, 79-82.

Pavan, F.A., Camacho, E.S., Lima, E.C., Dotto, G.L., Branco, V.T.A. and Dias, S.L.P., 2014. Formosa papaya seed powder (FPSP): Preparation, characterization and application as an alternative adsorbent for the removal of crystal violet from aqueous phase. Journal of Environmental Chemical Engineering. 2, 230-238.

Peng, L., Dai, H., Wu, Y., Dai, Z., Li, X. and Lu, X., 2018. Performance and adsorption mechanism of a magnetic calcium silicate hydrate composite for phosphate removal and recovery. Water Sci Technol. 2017, 578-591.

Pineda-Gómez, P., Rosales-Rivera, A. and Rodríguez-García, M.E., 2012. Effect of the thermo-alkaline treatment over the thermal degradation of corn starch. Starch - Stärke. 64, 776-785.

Plieva, F.M., Karlsson, M., Aguilar, M.-R., Gomez, D., Mikhalovsky, S. and Galaev', I.Y., 2005. Pore structure in supermacroporous polyacrylamide based cryogels. Soft Matter. 1, 303-309.

Qi, L., Tang, X., Wang, Z. and Peng, X., 2017. Pore characterization of different types of coal from coal and gas outburst disaster sites using low temperature nitrogen adsorption approach. International Journal of Mining Science and Technology. 27, 371-377.

Rout, P.R., Shahid, M.K., Dash, R.R., Bhunia, P., Liu, D., Varjani, S., Zhang, T.C. and Surampalli, R.Y., 2021. Nutrient removal from domestic wastewater: A comprehensive review on conventional and advanced technologies. Journal of Environmental Management. 296, 113246.

Seliem, M.K., Komarneni, S. and Abu Khadra, M.R., 2016. Phosphate removal from solution by composite of MCM-41 silica with rice husk: Kinetic and equilibrium studies. Microporous and Mesoporous Materials. 224, 51-57.

Sen Gupta, S. and Bhattacharyya, K.G., 2011. Kinetics of adsorption of metal ions on inorganic materials: A review. Advances in Colloid and Interface Science. 162, 39-58.

Shin, D.Y., Yoon, J.H., Kim, S.H., Baik, H. and Lee, S.J., 2018. Immobilization of a porphyrinic Mn(iii) catalyst on a new type of silica support comprising a three-dimensionally interconnected network with two different sizes of pores. Catalysis Science & Technology. 8, 6306-6310.

Silva, A.C.P.d., Estevão, B.M., Caetano, W., Santin, S.M.O., Hioka, N., Cordeiro, P.H.Y., Eckert, H., Moisés, M.P. and Tessaro, A.L., 2019. Synthesis of highly ordered mesoporous MCM-41: selective external functionalization by time control. Journal of the Brazilian Chemical Society. 30, 1599-1607.

Sing, K. and Williams, R., 2004. Physisorption Hysteresis Loops and the Characterization of Nanoporous Materials. Adsorption Science and Technology. 22.

Singh, P., Singh, M.K., Beg, Y.R. and Nishad, G.R., 2019. A review on spectroscopic methods for determination of nitrite and nitrate in environmental samples. Talanta. 191, 364-381.

Suzuki, H., Iijima, K., Moriya, A., McElroy, K., Scobie, G., Fyfe, V. and McColl, K.E., 2003. Conditions for acid catalysed luminal nitrosation are maximal at the gastric cardia. Gut. 52, 1095-101.

Taqanaki, E.R., Heidari, R., Monfared, M., Tayebi, L., Azadi, A. and Farjadian, F., 2019. EDTA-modified mesoporous silica as supra adsorbent of copper ions with novel approach as an antidote agent in copper toxicity. International journal of nanomedicine. 14, 7781-7792.

Thommes, M., Kaneko, K., Neimark, A.V., Olivier, J.P., Rodriguez-Reinoso, F., Rouquerol, J. and Sing, K.S.W., 2015. Physisorption of gases, with special reference to the evaluation of surface area and pore size distribution (IUPAC Technical Report). Pure and Applied Chemistry. 87, 1051-1069.

Thommes, M., Smarsly, B., Groenewolt, M., Ravikovitch, P.I. and Neimark, A.V., 2006. Adsorption hysteresis of nitrogen and argon in pore networks and characterization of novel micro- and mesoporous silicas. Langmuir. 22, 756-64.

Topacli, A. and Kesimli, B., 2001a. Investigation on Sulfanilamide and its Interaction with Some Metals and Lincomycin by Infrared Spectroscopy. Spectroscopy Letters - SPECTROSC LETT. 34, 513-526.

Topacli, A. and Kesimli, B., 2001b. Investigation on sulfanilamide and its interaction with some metals and lincomycin by infrared spectroscopy. Spectroscopy Letters. 34, 513-526.

Torit, J. and Phihusut, D., 2019. Phosphorus removal from wastewater using eggshell ash. Environmental Science and Pollution Research. 26, 34101-34109.

Tsikas, D., 2005. Analysis of the L-Arginine / Nitric Oxide Pathway: The Unique Role of Mass Spectrometry. Current Pharmaceutical Analysis - CURR Pharm Anal. 1.

Tsikas, D., 2007. Analysis of the l-arginine/NO pathway. Journal of Chromatography B. 851, 1-2.

Vazquez, N.I., Gonzalez, Z., Ferrari, B. and Castro, Y., 2017. Synthesis of mesoporous silica nanoparticles by sol–gel as nanocontainer for future drug delivery applications. Boletín de la Sociedad Española de Cerámica y Vidrio. 56, 139-145.

Wang, Q.-H., Yu, L.-J., Liu, Y., Lin, L., Lu, R.-g., Zhu, J.-p., He, L. and Lu, Z.-L., 2017. Methods for the detection and determination of nitrite and nitrate: A review. Talanta. 165, 709-720.

Wang, Y., Zhao, Q., Han, N., Bai, L., Li, J., Liu, J., Che, E., Hu, L., Zhang, Q., Jiang, T. and Wang, S., 2015. Mesoporous silica nanoparticles in drug delivery and biomedical applications. Nanomedicine: Nanotechnology, Biology and Medicine. 11, 313-327.

Wei, P., Tian, G., Yu, H. and Qian, Y., 2013. Synthesis of a novel organic-inorganic hybrid mesoporous silica and its flame retardancy application in PC/ABS. Polymer Degradation and Stability. 98, 1022-1029.

Wing, R.E., Maiti, S. and Doane, W.M., 1987. Factors affecting release of butylate from calcium ion-modified starch-borate matrices. Journal of Controlled Release. 5, 79-89.

Wongniramaikul, W., Limsakul, W. and Choodum, A., 2018. A biodegradable colorimetric film for rapid low-cost field determination of formaldehyde contamination by digital image colorimetry. Food Chemistry. 249, 154-161.

Xue, W., Champ, S., Huglin, M.B. and Jones, T.G.J., 2004. Rapid swelling and deswelling in cryogels of crosslinked poly(N-isopropylacrylamide-co-acrylic acid). European Polymer Journal. 40, 467-476.

Yeddou, N. and Bensmaili, A., 2007. Equilibrium and kinetic modelling of iron adsorption by eggshells in a batch system: effect of temperature. Desalination. 206, 127-134.

Yoobanpot, N., Jamsawang, P. and Horpibulsuk, S., 2017. Strength behavior and microstructural characteristics of soft clay stabilized with cement kiln dust and fly ash residue. Applied Clay Science. 141, 146-156.

Yu, P., Kirkpatrick, R., Poe, B., McMillan, P. and Cong, X., 2004. Structure of Calcium Silicate Hydrate (C-S-H): Near-, Mid-, and Far-Infrared Spectroscopy. Journal of the American Ceramic Society. 82, 742-748.

Yuh-Shan, H., 2004. Citation review of Lagergren kinetic rate equation on adsorption reactions. Scientometrics. 59, 171-177.

Zhang, Z., Liu, H., Wu, L., Lan, H. and Qu, J., 2015. Preparation of amino-Fe(III) functionalized mesoporous silica for synergistic adsorption of tetracycline and copper. Chemosphere. 138, 625-632.

Zhang, Z., Wang, X. and Zhao, J., 2019. Phosphate recovery from wastewater using calcium silicate hydrate (C-S-H): sonochemical synthesis and properties. Environmental Science: Water Research & Technology. 5, 131-139.

Zou, F. and Budtova, T., 2021. Tailoring the morphology and properties of starch aerogels and cryogels via starch source and process parameter. Carbohydrate Polymers. 255, 117344.

Appendices

Paper I

A novel colorimetric sensor based on modified mesoporous silica nanoparticles for rapid on-site detection of nitrite

Taweekarn, T., Wongniramaikul, W., Limsakul, W., Sriprom, W., Phawachalotorn C., and Choodum, A.

ORIGINAL PAPER

A novel colorimetric sensor based on modified mesoporous silica nanoparticles for rapid on-site detection of nitrite

Tarawee Taweekarn[1] · Worawit Wongniramaikul[1,2] · Wadcharawadee Limsakul[1] · Wilasinee Sriprom[1] · Chanadda Phawachalotorn[3] · Aree Choodum[1]

Abstract

A novel colorimetric sheet based on Griess reagent–doped mesoporous silica nanoparticles was developed for nitrite detection. Griess reagent was adsorbed on long–range ordered hexagonal mesoporous silica nanoparticles and developed ink–bottle pores with some disorder. When the modified nanoparticles were bound using starch to fabricate a thin ($\sim$ 313 μm) colorimetric sheet, spherical particles with a rougher surface and some distortion of their mesoporosity were observed. The sheet was used in conjunction with digital image colorimetry (DIC) and provides a wide linear range of 0.05 to 2.50 mg L^{-1} with a low detection limit (15.0 μg L^{-1}–NO$_2^-$, equal to 4.5 μg L^{-1} NO$_2^-$–N), good inter-day precision (1.93%RSD), and excellent precision (2.67% relative error). The colorimetric sensors produced from the sheet costs only 0.04 USD each, while the DIC uses a standard smartphone for photographic detection. The method developed offers an easier and cheaper means of conducting rapid on-site determination of nitrite in water with reliable quantitative results.

Keywords Mesoporous silica · Nitrite determination · Griess assay · Colorimetric sensor · Digital image colorimetry

Introduction

Nitrite (NO$_2^-$), a natural nutrient ion that is part of the nitrogen cycle, is derived from the degradation of organic compounds containing nitrogen, such as plant and animal proteins, and plays an important role in the ecosystem. The concentration of nitrite is an important indicator of water quality and it is

✉ Aree Choodum
aree.c@phuket.psu.ac.th

1   Integrated Science and Technology Research Center, Faculty of Technology and Environment, Prince of Songkla University, Phuket Campus, Kathu, Phuket 83120, Thailand

2   Research Program: The Development of Management System for Reduction and Control of Water Contamination and Distribution in Songkhla Lake Basin and the Western Coastline of the South of Thailand, Center of Excellence on Hazardous Substance Management (HSM), 10330 Bangkok, Thailand

3   Department of Applied Science and Business Management, King Mongkut's Institute of Technology Ladkrabang, Prince of Chumphon Campus, Pathiu, Chumphon 86160, Thailand

generally found in surface water at a low concentration (0.07 mg L^{-1} NO$_2^-$–N) because it is easily oxidized to nitrate. However, human activities, e.g., the use of synthetic fertilizers in agriculture and the discharge of chemical fertilizer or industrial waste, may increase the contamination of nitrite in water, which can accelerate eutrophication and has led to the deterioration of the ecosystem. In addition, nitrite has been reported to interfere with the oxygen transport system in animals by irreversibly converting hemoglobin to methemoglobin, resulting in a great reduction in hemoglobin's ability to exchange oxygen [1]. Nitrite is thus dangerous as it can cause methemoglobinemia in aquatic animals [2] and blue baby syndrome in infants [3]. Furthermore, nitrite can also react with secondary and tertiary amines in the stomach causing carcinogenic N–nitrosamines [4]. Therefore, the determination of the presence of nitrite is very important for both environmental protection and public health.

Although accurate results for the analysis of nitrite have been reported using instrumental methods, including ion chromatography (IC), capillary electrophoresis (CE), chemiluminescence, and high–performance liquid chromatography (HPLC), these methods required expert and complicated sample preparation procedures for analysis [5] and also suffer from not being suitable for on-site application. A number of

researchers have thus attempted to develop colorimetric sensors to facilitate on-site determination of nitrite, and several colorimetric reagents based on diazotization and nitrosation reaction have been reported. Barbituric acid has been used to react with nitrite to give a nitroso derivative, violuric acid, with a maximum absorption at 310 nm [6]. This reaction provides a linear calibration in the range of 0 to 3.22 mg L^{-1}–NO_2^- with a determination limit of 9.5 ppb NO_2^-–N. A lower detection limit of 2.9 ppb NO_2^-–N has been reported using phloroglucinol (1,3,5–trihydroxybenzene) [7] which also provided a higher sensitivity nitroso product than using N,N–bis(2–hydroxypropyl)aniline, other phenols and naphthol derivatives [7]. Griess assay seems to be the most widely used colorimetric method in the determination of nitrite as summarized in some reviews [5, 8, 9] due to its low cost, high sensitivity, high stability, and robust performance [10]. This assay is based on a diazotization reaction of nitrite with sulfanilamide in acidic conditions to produce diazonium cations, which are further reacted with the aromatic amine, N–(1–naphthyl) ethylenediamine dihydrochloride (NED), giving azo dye products. Griess reagent–based polymeric sensors have also been developed to avoid the use of liquid reagents, making on-site analysis easier and safer. NED-doped polyethylene glycol (PEG) hydrogel was modified on a glass fiber strip which was able to react with nitrite ions pre-mixed with sulfanilamide and provided a detection limit of 10 μM [11]. However, although the concentration of nitrite can be measured immediately after dropping the sample on the modified strip, the sample (and the standard solution) has to be mixed with sulfanilamide before testing. Hydrogel materials also commonly suffer from a swelling problem with low surface areas.

In this work, a novel colorimetric sheet based on Griess reagent–doped mesoporous silica was developed for nitrite detection. Mesoporous silica is a porous nanomaterial with a pore size in the range of 2–50 nm [12]. Due to its unique physiochemical properties, i.e., it has a large specific surface area and pore volume and is highly porous, chemically inert and functionalizable, with tunable pore and particle sizes [13], it has been applied in various roles, including drug delivery, biomedical and environmental applications [13]. Because of the high porosity of mesoporous silica, it is possible to adsorb Griess reagent and use it as a colorimetric sensor for the detection of nitrite in water. The colorimetric sensor developed in this work was used in conjunction with digital image colorimetry (DIC) rather than spectrophotometry to facilitate rapid on-site quantitative analysis. During imaging with a digital camera, the light reflected by the colorimetric product obtained from the colorimetric sensor passes through an RGB filter and splits into three components (i.e., 400–500, 500–580, and 580–700 nm for the blue, green, and red filter, respectively) [14]. The separated wavelengths are then detected and recorded on an image sensor located behind each filter and the final

color of the digital image is composed of the combined data from the three RGB filters. When the digital image is analyzed by a color analysis program, the individual RGB data recorded are obtained, representing the total photons in each region of the spectrum and can be used as analytical data for quantification.

Experimental

Materials

N–(1–Naphthyl) ethylenediamine dihydrochloride (NED) (99%), sodium nitrite (99%), phosphoric acid (85%), and sodium hydroxide (99%) were supplied by Ajax Finechem (Sydney, Australia www.ajaxfinechem.com). Sulphanilamide (99%) was supplied by Panreac (Barcelona, Spain http://panreac.com), while hydrochloric acid (37%) was obtained from (Carlo Erba, Spain https://www.carloerbareagents.com/). Analytical grade acetone was obtained from J.T. Baker (Radnor, USA https://www.fishersci.com/). All standard solutions were prepared with ultrapure water purified by a water purification system (Merck, Darmstadt, Germany https://www.merckgroup.com/). Tetraethyl orthosilicate (TEOS) (99%) was obtained from Sigma–Aldrich (St. Louis, USA https://www.sigmaaldrich.com/), while cetyltrimethylammonium bromide (CTAB, 99%) was supplied by Loba (Mumbai, India https://www.lobachemie.com/). Commercial grade ethanol (95%) was supplied by S.N.P. Scientific Co. Ltd. (Bangkok, Thailand https://www.snp-scientific.com/) and cassava starch was supplied by Jaydee Brand, SUV intertrade (Nakhon Pathom, Thailand).

Preparation of mesoporous silica

Mesoporous silica was prepared by a modified procedure from previous reports [15, 16]. CTAB surfactant (1.64 g) was added to sodium hydroxide solution (0.1 M, 60 mL) under stirring and heated at 60 °C for 1 h. After cooling to room temperature, ethanol (13.20 mL) was then added into the solution. Alkoxide precursor, TEOS (5.56 mL), was then added causing the solution to immediately become opaque with the start of the reaction. The solution was further stirred for 24 h allowing the reaction to be completed. The white precipitate resulting was then filtered, washed with ultrapure water, and dried at 110 °C overnight. The particles were then calcined at 550 °C for 10 h and stored in a desiccator prior to use.

Preparation of colorimetric sensor

The colorimetric sensor developed in this study was based on the adsorption of Griess reagent on mesoporous silica

nanoparticles. The ingredients for fabricating the nitrite sensor were optimized to obtain the formulation that produced the darkest color product from nitrite using the least amount of chemicals. The Griess reagent used as the colorimetric reagent was prepared by dissolving sulphanilamide (50–500 mg), NED (5–50 mg), and 85% phosphoric acid (1.0–2.0 mL) in 10 mL of ultrapure water. Mesoporous silica (0.5 g) was then added to 10 mL of the Griess reagent and stirred at room temperature for 2 h to allow the adsorption of the reagent onto the particles. The particles were then filtered using a vacuum pump and kept in a desiccator in a brown bottle to protect them from light.

The Griess–adsorbed silica can be used as a colorimetric sensor, in the form of both particles (Griess–adsorbed mesoporous silica particles: GMSP) and as a thin sheet (Griess–adsorbed mesoporous silica sheet: GMSS). The GMSS was prepared by binding the GMSP with a starch solution in the presence of acetone. The starch solution was prepared by gelatinizing cassava starch (1% w/v) in ultrapure water at 90 °C under continuous stirring until a clear viscous solution was obtained. Then, 0.50 g of GMSP was mixed with the starch solution (5 mL) under magnetic stirring to ensure a homogeneous distribution before the addition of acetone solution (2 mL), and the mixture was further stirred for 3–5 min. The slurry (100 μL) was then deposited on the flat cap of a 1.5-mL centrifuge tube and incubated at 100 °C for 15 min. After cooling to room temperature, the sensors were immediately vacuum-sealed in packs of three in an opaque foil bag and stored in a refrigerator for further use.

Characterization of mesoporous silica, GMSP, and GMSS

The morphology of the mesoporous silica, GMSP, and GMSS prepared was investigated using a field emission scanning electron microscope (FESEM, Apreo, FEI https://www.thermofisher.com/), while the microstructure of the nanoparticles was analyzed using a transmission electron microscope (TEM, JEM–2010, JEOL https://www.jeol.co.jp/) at 200 kV. A Fourier transform infrared spectrophotometer (FTIR, Vertex70, Bruker https://www.bruker.com/) was used to investigate their functional groups using the KBr pellet method. The XRD pattern was obtained using an X-ray diffractometer (Empyrene, PANalytical https://www.malvernpanalytical.com/). The surface area, porosity, and pore size distribution was determined by means of the nitrogen adsorption/desorption isotherm using a high throughput surface area and porosity analyzer (ASAP2460, Micromeritics https://www.micromeritics.com/) at 77 K. The prepared silica sample was degassed at 250 °C for 20 h to remove physically absorbed gasses from the sample surface before analysis, while the GMSP and GMSS were processed at 105 °C for 24 h to avoid the degradation of the chemical recipes used for modification. The Brunauer–Emmett–Teller (BET) method was applied to calculate the specific surface area (S_{BET}). The pore volume was obtained from an adsorption branch using the Barrett, Joyner, and Halenda (BJH) method. The average pore diameter was calculated from the pore volume and BET surface area.

Colorimetric test of nitrite and digital image colorimetric system

Colorimetric tests of nitrite using GMSP and GMSS were conducted using sodium nitrite as a nitrite standard. A stock solution (100 mg L^{-1}) was prepared by dissolving sodium nitrite in ultrapure water, which was further diluted with ultrapure water to appropriate concentrations (0–1 mg L^{-1}) as standard working solutions. For testing, the GMSP were directly added into the standard solution in a vial (2 mL), while 100 μL of standard solution was dropped on the GMSS and left for an appropriate time to allow the diazotization reaction to take place. Three replications were conducted at each nitrite concentration.

DIC was applied after colorimetric testing for quantitative analysis. A custom-built RGB photographic box (8.5 × 9.5 × 6.25 in.) modified from previous work [17] was used to eliminate any effects of environmental light. Three GMSS sensors were placed in sample holders inside the box, while an iPhone 7.0 was then positioned above an opening on the top of the box. Six images of the colorimetric products were then taken using the digital camera of the iPhone (12MP, backside-illuminated CMOS). The aperture, illumination, and photo settings were fixed as follows: f/1.8 aperture, 1/18 s exposure time, ISO 20, flash off, automatic white balance, HDR off, to achieve reproducible results. The images were saved as JPEG files (24–bits, 1.31 MB, 3024 × 4032 pixels) to the iPhone's memory before being transfer to a computer for color analysis. A custom-built RGB analysis program [17–19] was then used to analyze the average intensities of the RGB values of the color products from the six images from each of the three sensors used as a single data point for each standard concentration, from which calibration curves were established.

Effect of pH and reaction time

As pH is an essential condition for ion analysis, the effect of the pH was investigated. Nitrite standard solution (1.00 mg L^{-1}) was adjusted to various pH levels (1 to 9) with sodium hydroxide or hydrochloric acid, before being tested with GMSS. The colorimetric products obtained were then photographed and analyzed.

The optimum reaction time between nitrite and the Griess reagent in the GMSS was also investigated by dropping nitrite standard solution (100 μL, 1.00 mg L^{-1}, adjusted to pH 6) on GMSS for between 0 and 30 min.

Influence of interferences

The GMSS was also tested with some substances present in seawater which might interfere with the detection of nitrite, comprising Na^+, Mg^{2+}, Ca^{2+}, Cu^{2+}, Ni^{2+}, Zn^{2+}, Pb^{2+}, F^-, Cl^-, SO_4^{2-}, CO_3^{2-}, OH^-, and NO_3^- [20] to investigate its selectivity. Standard solutions of each substance were prepared at 10,000 mg L^{-1} before testing with the GMSS using the same procedure as for nitrite standard solution (1.00 mg L^{-1}). Each ion (10,000 mg L^{-1}) was also mixed with nitrite standard solution (0.50 mg L^{-1}) and adjusted to pH 6 before being tested with GMSS.

Influence of seawater matrix

The influence of the seawater matrix was evaluated using seawater sampled from the Andaman Sea far from human activity (1 km from He Island, 8 km from Chalong Pier, Phuket province, Thailand). The seawater was used to prepare nitrite standard solutions at various concentrations (0–1 mg L^{-1}, adjusted to pH 6) instead of ultrapure water. The sensitivity of the standard graph from using seawater was compared to that using ultrapure water.

Analytical performance and method validation

The DIC calibration curve for quantitative analysis of nitrite was established by plotting the analyzed RGB intensities of the digital image of the color products against the concentrations of nitrite (0 to 100 mg L^{-1}). The linear portion was selected for quantitative analysis by considering the widest concentration range of nitrite that provided a linearity (R^2) > 0.99. Intra-day precision in terms of percentage relative standard deviation (%RSD) was investigated by testing three GMSS sensors on the same day. The same experiments were performed on five consecutive days for inter-day precision. The accuracy in terms of the percentage relative error (%RE) was evaluated by analyzing the nitrite standard at a known concentration (0.75 mg L^{-1}) against the established calibration curve. The detection limit was determined based on the IUPAC guidelines by testing ultrapure water using 12 GMSS sensors. After their digital images were analyzed, the standard deviation of the RGB intensities was used to calculate the LOD as 3SD/slope of the calibration graph (m) [21].

Real sample analysis

The GMSS and DIC were applied to investigate nitrite contamination in seven seawater samples randomly collected from Kalim and Tri Trang Beaches (Phuket, Thailand; Fig. 1) which is often found to suffer from eutrophication, as well as an effluent sample from a hotel treatment plant at Kalim Beach (K1). The samples were kept in polyethylene bottles without airspace and stored in ice in a styrene foam box. They were then filtered through a 0.20-μm cellulose acetate membrane and the pH adjusted to 6 before being tested with the GMSS/DIC method developed within a few hours. All the samples were also analyzed using the standard method for nitrite detection using a spectrophotometric for comparison [22].

Results and discussion

Characterization of prepared silica nanoparticles

Mesoporous silica nanoparticles were synthesized by the sol-gel method [15, 16] using TEOS as a silica precursor in alcohol solution (ethanol) under basic conditions (NaOH) in the presence of a surfactant (CTAB). The formation of mesoporous silica nanoparticles occurred via the swelling-shrinking mechanism proposed by Yi et al. [23] as shown in Online Resource (S1). Template molecules, CTAB at a concentration greater than the critical micelle concentration in aqueous solution, self-assemble into spherical micelles and periodic liquid crystal mesophases. After the addition of ethanol and TEOS which concentrate at hydrophilic interfaces, condensation occurred through electrostatic and hydrogen bonding interaction to form an amorphous silica mold of the ordered periodic mesophase [24]. Thus, TEOS was firstly solubilized in CTAB hydrocarbon cores, consequently enlarging the micelles. When TEOS within the CTAB hydrocarbon core was completely consumed, the micelles shrunk and became smaller in size [23]. The template is then removed by calcination [24] that could also eliminate the hydroxyl groups on the silica [25, 26].

The results from BET analysis showed that the nanoparticles prepared had an average pore size of 2.8 nm with a multipoint specific surface area of 1208 m^2 g^{-1} and a pore volume of 0.84 mL g^{-1}. These were very similar to those reported in previous work as having been synthesized using a similar procedure with a surface area of 1200 m^2 g^{-1} with a 2.4-nm pore diameter [15]. In addition, the nanoparticles exhibited a typical type IV adsorption isotherm (S2a) corresponding to those in previous reports [15, 16, 27] where the capillary condensation of N_2 within a pore occurred above $P/P_0 = 0.3$ indicating the presence of ordered hexagonal mesopores [16, 28]. A parallel H4 hysteresis loop indicated a narrow slit-like pore or hollow spheres with walls composed of ordered mesoporous silica. Moreover, the narrow pore size distribution (S2b) indicated a significant presence of mesopores with a homogeneous pore size [16, 27] of about 2.44 nm similar to those in a previous report (i.e., 2–3 nm [16]).

The FESEM images of the prepared silica nanoparticles showed an agglomeration of spherical nanoparticles with a
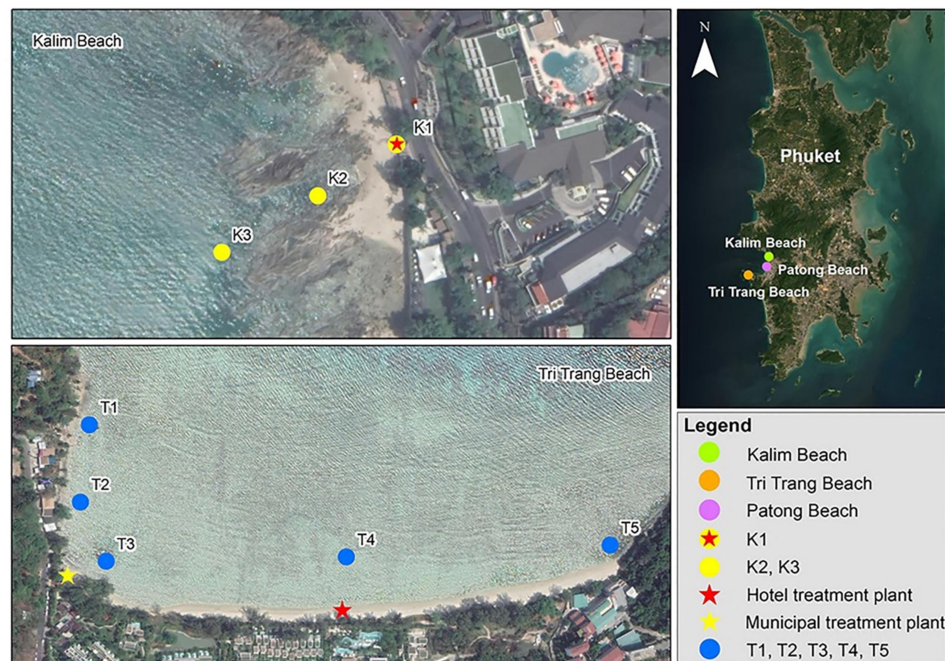
Fig. 1 Sampling points for real samples

rough external surface (Fig. 2a). In order to characterize them in more detail, the silica nanoparticles were imaged by TEM as shown in Fig. 3. The micrograph confirmed their spherical shape and demonstrated a variety of particle sizes between 200 and 600 nm (Fig. 3a). At high magnification (Fig. 3b), the TEM image also confirmed the presence of a hexagonal array and ordered mesopores with a honeycomb structure.

In addition, the porous structure of the prepared particles was investigated using XRD. The powder's XRD pattern revealed diffraction peaks in lower 2θ angles indicating the hexagonal structure [29] as shown in Online Resource (S3). Absorption peaks were observed at 2θ values of 0.60°, 1.80°, and 4.58° (broad peak) with d-spacing of 17.1, 5.29, and 1.96 nm, respectively, which could be indexed to the (100), (110), and (200) planes of the porous structure, respectively, indicating the long-range order of the hexagonal structure [29].

The FTIR spectrum of the prepared silica nanoparticles is shown in Fig. 4a. The large absorption band at 3454 cm^{-1} was attributed to the stretching vibration of the O–H groups of mesoporous silica [30]. This indicated the remaining the hydroxyl group on prepared silica although the calcination of 550 °C was applied for 10 h. The small peaks at 2925, 2854,

and 1462 cm^{-1} were associated with symmetrical and asymmetrical stretching of the CH$_2$, CH$_3$, and CH$_3$–(N$^+$) groups, respectively, of CTAB residues [15, 31]. An intense band of asymmetric Si–O–Si stretching was observed at 1085 cm^{-1}, while the peaks at 969 cm^{-1} and 800 cm^{-1} corresponded to the vibration of free Si–OH and Si–O–Si bending, respectively [15, 30, 32]. Finally, the band at 1637 cm^{-1} was attributed to the bending vibration of O–H groups from water molecules physically absorbed in the silica [32].

Optimization and characterization of GMSP

The GMSP were prepared by the adsorption of Griess reagent onto mesoporous silica nanoparticles. The GMSP preparation was optimized by formulating the Griess reagent that could be adsorbed onto the silica nanoparticles and produce the darkest color product when exposed to nitrite, using the least possible amount of chemicals. The results and additional data of optimization are shown in Online Resource (S4).

The results from BET analysis of the GMSP showed an obvious reduction in the specific surface area to 137 m^2 g^{-1} with a lower pore volume of 0.20 mL g^{-1} due to the adsorption of Griess reagent on the surface of the mesoporous silica,

Fig. 2 FESEM images of prepared silica nanoparticles (**a**), GMSP (**b**), GMSS (**c**), and cross-section (**d**) of GMSS showing the thickness of the sheet

which favored pores with a small size. This led to an increase in the average pore size to 5.9 nm compared to 2.4 nm in the parent silica. However, it is to be noted that the temperature used to degas the GMSP before analysis (105 °C for 24 h) was less than that used in the parent silica (250 °C for 20 h) which may have contributed to physical adsorption of stranger on the GMSP pores. The GMSP exhibited a typical type IV adsorption isotherm of N_2, indicating the remaining of mesopores from the parent silica. However, it revealed a parallel H2 hysteresis loop (S5a) instead of an H4 hysteresis loop as observed in the parent silica, indicating ink–bottle pores (a pore mouth smaller than the pore body) [33]. This result suggested that the Griess reagent was absorbed at the mouth of the silica mesopore. The pore size distribution (S5b) displayed pores of 1.5, 1.7, 2.9, 3.4, and 5.4 nm implying that the GMSP have a polymodal nanostructure, mainly due to their disordered mesoporous structure [28]. Spherical particles of size 400–1000 nm were observed in the GMSP with a rougher external surface area than that of the parent silica (Fig. 2b). TEM micrographs confirmed that GMSP maintained its spherical shape but the particles were larger at around 800 nm (Fig. 3c); however, the ordered structure of the parent silica seemed to be changed by the adsorption of the Griess reagent (Fig. 3d). The strong peak in diffraction intensity observed at 4.58° in the parent silica also clearly reduced, indicating some extent of disorder, although the diffraction peaks of (100) and (110) were still present at 0.51° and 1.42°, respectively. This

confirmed that the GMSP preserved its mesoporous structural order after the adsorption of Griess reagent, but some disorder also occurred [29, 34].

The FTIR spectra of the GMSP showed a shift in the absorption band at 3454 cm^{-1} in the parent silica to 3425 cm^{-1} and it became broader after the adsorption of Griess reagent (Fig. 4b). The O–H groups of the parent silica [30] may overlap with the O–H from the phosphoric acid and N–H group from the NED and sulfanilamide [35]. The small peaks at 2923, 2855, and 1463 cm^{-1} of the CTAB residues from the mesoporous silica [15, 31] remained in their positions. Although the vibration band of O–H bending from water molecules which was present in the parent silica at 1637 cm^{-1} seemed to remain in the same position, it may overlap with the C=O stretching [35] or NH_2 scissoring [36] of the sulfanilamide. Similarly, the intense band of Si–O–Si and Si–OH vibration observed in the parent silica at 1085 cm^{-1} and 969 cm^{-1} [15, 30, 32] may overlap with the SO_2 symmetric stretching of the sulfanilamide (which commonly appears at 1150 ± 15 cm^{-1} [36]) and was observed at 1091 and 1161 cm^{-1} in the GMSP. Finally, a band observed at 2384 cm^{-1} was associated with the vibration of the NED functional groups.

As expected, the colorimetric test of the GMSP with nitrite standard solution provided a red–violet product (Fig. 5a). This product occurred within the layers of GMSP at a high concentration of nitrite (>25 mg L^{-1})

Fig. 3 TEM images of prepared silica nanoparticles (**a**, **b**), GMSP (**c**, **d**), and GMSS (**e**, **f**)
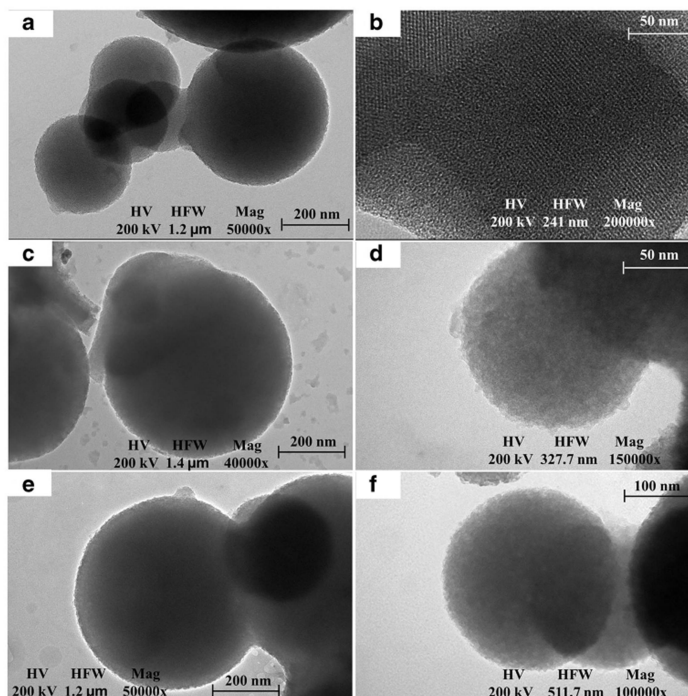
but dissolved out into the solution at a low concentration. This contributed to a gradient concentration and size of the nitrite molecules. The diffusion flux of the nitrite ions from their solution into the GMPS at a high concentration was faster than at a low concentration causing the amount of

Griess reagent at a high concentration of nitrite to rapidly reduce when the colorimetric reaction occurred. This caused the concentration gradient of the Griess reagent on the GMPS to be very low, leading to less diffusion to the solution. The colorimetric product thus occurred on the
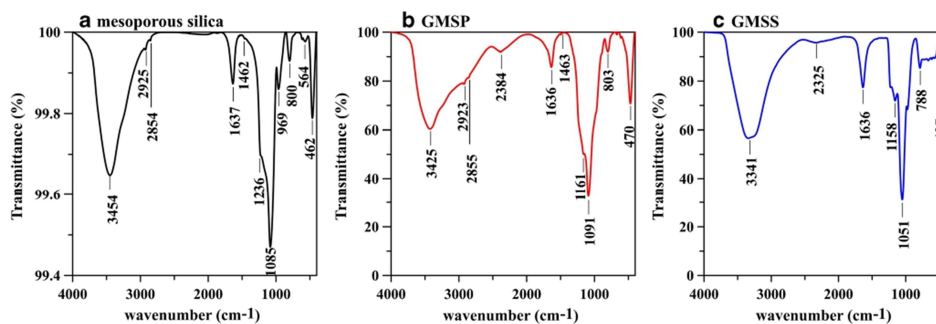

Fig. 4 FTIR spectra of prepared silica nanoparticles (**a**), GMSP (**b**), and GMSS (**c**)

86

87

a

b

          0   0.1   0.25   0.5   1   5   25   50   75   100 mgL⁻¹
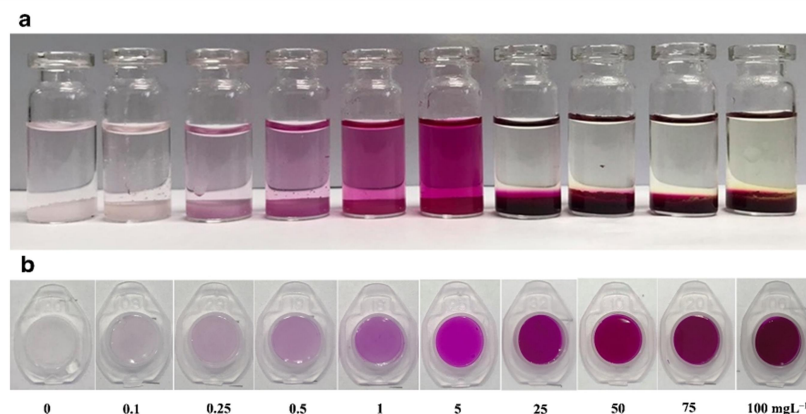
Fig. 5 The colorimetric products of GMSP (**a**) and GMSS (**b**) from testing with nitrite at various concentrations

GMPS only. In contrast with a low concentration of nitrite, a slower diffusion flux of nitrite occurred, and some of the Griess reagent desorbed from the silica particles and reacted with the nitrite in the solution. The results indicated that some of the Griess molecules might absorb on mesoporous silica with weak interaction, e.g., physical absorption, together with hydrogen bonding interaction between remaining silanol on prepared mesoporous silica and amine and/or hydroxyl groups from Griess reagent. However, the red−violet product at a low concentration of 0.25 mg L^{-1}–NO_2^- (0.08 mg L^{-1} NO_2^-–N) could be clearly observed with the naked eye, indicating good sensitivity for nitrite detection by the GMPS.

Optimization and characterization of GMSS

The GMSS was prepared by binding the GMSP with starch in the presence of acetone and fabricating a thin white sheet with a thickness of 313 μm (Fig. 2d) on the flat lid of a small centrifuge tube (1.5 mL). Additional data for optimization of GMSS is shown in Online Resource (S6).

As expected, the results from the BET analysis of the GMSS showed a lower pore volume of 0.15 mL g^{-1} than the GMSP, as well as the parent silica, due to the binding of the GMSP in a starch film, indicating that the starch may fill the pores of the GMSP. Its specific surface area (168 $m^2\,g^{-1}$) was less than that of the parent silica (1200 $m^2\,g^{-1}$), but was slightly higher than that of the GMSP (137 $m^2\,g^{-1}$). The average pore size of the GMSS (3.7 nm) was bigger than that of the parent silica (2.8 nm), but smaller than that of the GMSP (5.9 nm). It seems that some of the Griess reagent adsorbed on the small pores of the silica in the GMSP may desorb and dissolve in the starch solution before coating the silica particles of the GMSS as a thin film, resulting in a decrease in the

average pore size of the GMSS compared to the GMSP. This result corresponded to the maintenance of a type IV adsorption isotherm of N_2 on the GMSS with a parallel H4 hysteresis loop (S7a) as in the parent silica. The pore size distribution of GMSS (S7b) was narrower than that of GMSP but continued to show a polymodal nanostructure, indicating a disordered mesoporous structure [28]. As expected, the FESEM images of the GMSS showed rougher particles than the GMSP and parent silica, while the particles spherical shapes could still be observed with a size of ~ 1 μm (Fig. 2c). The TEM micrographs also confirmed the spherical shape of the particles in the GMSS (Fig. 3e) with some distortion of its mesoporosity similar to that of the GMSP (Fig. 3f). The XRD pattern of the GMSS at a low angle was also similar to that of the GMSP (S3) confirming its mesoporous silica characteristic with some disorder.

The presence of starch in the GMSS made a large absorption band of O–H stretching at 3425 cm^{-1} in the GMSP become broader and shifted toward a lower frequency (3341 cm^{-1}; Fig. 4c), while it commonly present at 3280 cm^{-1} in starch [17]. The band of NED functional groups observed at 2384 cm^{-1} in the GMSP had shifted to 2325 cm^{-1} in the GMSS. The intense band of Si–O–Si stretching observed at 1085 cm^{-1} in the silica, which shifted to 1091 cm^{-1} in the GMSP may overlap with the C–O vibration peaks of amylopectin in the starch and had shifted to 1051 cm^{-1} in the GMSS [17, 37]. The SO_2 of the sulfanilamide present at 1161 cm^{-1} in the GMSP remained in a similar position at 1158 cm^{-1} in the GMSS.

Colorimetric test and DIC for quantification of nitrite

The colorimetric test of nitrite using GMSP and GMSS was based on the reaction of the Griess reagent adsorbed on the

mesoporous silica and the nitrite ions in the sample solutions. Those ions reacted with the sulfanilamide in the acidic conditions, forming diazonium cations, which then reacted with NED to form azo dye [8, 10]. A red–violet product occurred immediately after testing which reached equilibrium after 3 min (S8a). This was more rapid than the EPA 1686 standard method based on the same reaction (10 min) [22] and a previous study based on a nitrosation reaction (30 min) [6].

GMSS was used to evaluate the performance in quantifying nitrite since it requires only 100 μL of the sample or standard compared to GMSP which requires 2 mL. The influence of pH on the intensities of the colorimetric product was investigated, since acidic conditions were required for the Griess reaction. The results showed that the intensity of the green light from the digital image of the red–violet product decreased with pH levels of 1 to 3 and thereafter became constant (S8b), indicating that the reaction is able to occur effectively when the pH of the solution has a pH in the range of 3 to 9. The use of phosphate buffer for pH adjustment provided the same results as using HCl and NaOH. Since the EPA standard method [22] recommends a pH of 5 to 9 for the analysis of nitrite, pH 6 was selected in the analysis of nitrite in the sample of seawater, which commonly has a pH of 6 to 7. When the standard or sample adjusted to pH 6 was dropped on the GMSS, the pH reduced to 2 as the GMSS contained phosphoric acid and the reaction thus occurred in acidic conditions. This corresponded to a previous work in which the reaction of a Griess–modified polyethylene glycol hydrogel occurred at pH 2 [11].

A darker product was obtained with an increasing concentration of nitrite (Fig. 5b) because the products absorbed more light at a wavelength of 543 nm corresponding to red–violet, and reflected less intense light at other wavelengths.

The relationship between the RGB intensities, I_R, I_G, I_B, and concentrations of nitrite between 0 and 100 mg L^{-1} are shown in Fig. 6a. The results showed that the intensities of I_R and I_B were higher than that of I_G, indicating the appearance of the red–violet product which reflects red and blue light while absorbing green light (500–580 nm). This result corresponded to the spectrophotometric results in which the maximum absorption of the red–violet product was obtained at 543 nm, while the literature has variously reported absorption at 540 nm [5], 543 nm [38], and 548 nm [11]. The RGB intensities decreased when the concentration of nitrite was increased because darker products were obtained at higher concentrations. The change in I_G was much higher than those in I_B and I_R indicating that most of the green light was absorbed, resulting in the red–violet product. The linear portion of I_G and I_B observed in the range of 0.05 to 1.00 mg L^{-1} could be applied in the quantitative analysis of nitrite although the use of I_G is recommended as higher sensitivity was obtained. The relationship between I_G/I_{Total} ($I_R + I_G + I_B$) and the concentration of nitrite was also investigated to minimize the influence of the imaging conditions [39] and a wider linear range of 0.05 to 2.50 mg L^{-1} was observed (Fig. 6b).

System performance and method validation

The analytical performance of GMSS and DIC for the analysis of nitrite was investigated. Since the red–violet product specifically absorbed the light at 543 nm, the I_G presented the highest sensitivity (70 ± 2 a.u. L mg^{-1}) with good linearity ($R^2 = 0.9968$). The linear range of the I_G relationship was in the range of 0.05 to 1.00 mg L^{-1}, while the limit of detection (LOD) and limit of quality (LOQ) were found to be 40.0 ± 8.0 μg L^{-1} and 0.12 ± 0.03 mg L^{-1}–NO$_2^-$, respectively (equal to 12.2 and 36.5 μg L^{-1} NO$_2^-$–N, respectively). These are lower than the concentration limits for drinking water suggested by the US Environmental Protection Agency (1 mg L^{-1}) [40] and the World Health Organization (3 mg L^{-1} for short-term, and 0.2 mg L^{-1} for long-term exposure) [41]. A wider linear range was obtained from I_G/I_{Total} (0.05 to 2.50 mg L^{-1}) with a lower LOD of 15.0 μg L^{-1} and an LOQ of 0.05 mg L^{-1} (equal to 4.6 and 15.2 μg L^{-1} NO$_2^-$–N, respectively).

Fig. 6 Relationships between the concentration of nitrite (**a**) and RGB intensities (**b**) I_G/I_{Total} from color products
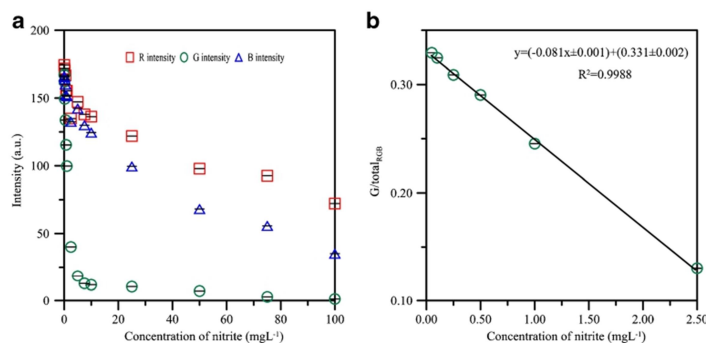
88

Table 1   Analytical performance of the developed method compared to previous reports

Parameter	Ref. [42]	Ref. [11]	This work
Method	Sequential injection analysis with miniaturized fiber optic colorimetric sensor	Colorimetric sensor	Colorimetric sensor
Supporting material	–	Polyethylene glycol hydrogel superimposed glass fiber membrane strip	Mesoporous silica-starch composite
Colorimetric reagent	Griess reagent	Griess reagent	Griess reagent
Detection method	Microspectrophotometer	Digital image colorimetry	Digital image colorimetry
Analysis time	40 min for incubation time with 6.24 s for detection	Few seconds, but the sample is pre-mixed with sulfanilamide before testing	3 min
On-site analysis	Difficult	Easy	Easiest
Linear range	0.2 to 1.8 mg L^{-1}	0.46 to 2300 mg L^{-1}	0.05 to 2.50 mg L^{-1}
Limit of detection	7 µg L^{-1}	460 µg L^{-1}	15 µg L^{-1}
Precision	0.37%RSD	–	1.93 %RSD
Accuracy	<5% relative error	–	2.67% relative error

The colorimetric test using GMSS also provided good accuracy from quantifying control samples (0.75 mg L^{-1}, $n = 3$) with a 2.67% relative error, while the %recovery of spiked water samples (ultrapure, tap, and seawater samples collected from a source far from human activities) were in the range of 88–114% (S9). Good intra-day precision of 1.30%RSD from nine GMSS sensors was obtained while the analysis of nitrite using 15 GMSS sensors over 5 days provided 1.93%RSD. When the cost of the GMSS as a nitrite sensor was considered, one sheet costs only THB0.75 (USD0.02), while each sensor (thin sheet and flat cap) costs ~ THB1.25 (USD0.04) which is much cheaper than other commercially available test kits, e.g., Nitrite Chemical Test Kit HI3873, (0–1 mg L^{-1}) which costs USD36/100 tests and Nitrite Low Range Checker HI707–25 (0–600 µg L^{-1}) which costs USD13/25 tests. The analytical performance of the developed sensor was compared with previous reports [11, 42] as shown in Table 1.

The feasibility of GMSS and DIC for on-site quantitative analysis was also evaluated. The results showed that the RGB intensities remained unaffected by external lighting being on or off (S10), indicating that external light had no measurable effect on the system developed, which can thus be used for on-site quantitative analysis of nitrite.

Influence of coexisting ions and matrix effect

The influence of interference from other substances on nitrite testing using GMSS was investigated. Red–violet product was observed only from nitrite ions even at a much lower concentration (1.00 mgL^{-1}), while no color change was observed from any of the other ions (10,000 mgL^{-1}) (S11). A possible coexisting interference effect was also evaluated by adding each ion at a concentration of 10,000 mgL^{-1} to a nitrite

standard solution with a concentration of 0.50 mgL^{-1} before testing with GMSS. The I$_G$ of the digital images of the products showed changes in the range of 0.01–4.69% (S12), indicating good selectivity of GMSS for nitrite. The effect of the seawater matrix was also evaluated as shown in Online Resource (S13).

Real sample analysis

The GMSS and DIC were applied for the determination of nitrite in seawater and effluent from a hotel treatment plant in Phuket and the results are shown in Table 2. The highest concentration of nitrite of 4.52 ± 0.79 mg L^{-1} was found in the effluent from the hotel treatment plant at Karim Beach (K1), while the concentration of nitrite at K2 (0.13 ± 0.02 mg L^{-1}) was lower than at K1, but higher than at K3, where the effluent

Table 2   Concentration of nitrite in seawater collected from Kalim and Tri Trang Beach, Phuket

Sample	Concentration of nitrite (mgL^{-1})	
	Developed method	Spectrophotometric method
K1	4.52 ± 0.79	4.11 ± 0.87
K2	0.13 ± 0.02	0.20 ± 0.04
K3	nd	nd
T1	0.08 ± 0.00	nd
T2	0.07 ± 0.02	0.12 ± 0.02
T3	0.11 ± 0.04	0.15 ± 0.06
T4	0.14 ± 0.06	0.17 ± 0.07
T5	0.04 ± 0.02	nd

nd, no detectable

89

was diluted by seawater. No effluent from the hotel treatment plant at Tri Trang Beach could be collected on the day of sampling; however, nitrite was found in seawater samples collected at T3 and T4 located near municipal and hotel treatment plants at levels of 0.11 ± 0.04 and 0.14 ± 0.06 mg L^{-1}, respectively. The results obtained using GMSS were not significantly different from those obtained using the standard spectrophotometric method at the 95% confidence level (calculated t value = 0.893, critical t value = 2.776, degrees of freedom = 4).

Stability of GMSS

The results of the stability evaluation are shown in Online Resource (S14). It is recommended that GMSS should be kept in a refrigerator where an increase in color intensity of + 5.5% and 12.6% was found after 3 months and 1 year's storage.

Conclusions

A novel colorimetric sheet for nitrite detection was successfully developed based on the adsorption of Griess reagent on mesoporous silica nanoparticles. The spherical nanoparticles from which the sheet was developed retained their shape after the adsorption of the Griess reagent, but had a rougher surface, and some disorder of the long range–ordered hexagonal pores was observed. The Griess reagent seems to absorb on mesoporous silica nanoparticles with both physical and chemical absorption. The Griess–adsorbed silica nanoparticles can be used for colorimetric testing of nitrite both in particle form and in the form of a thin sheet made by binding the nanoparticles using starch. The colorimetric sheet developed rapidly changed from white to red–violet within 3 min at pH 6 without any interference from other common ions, as well as a seawater matrix. The sheet was used in conjunction with DIC to allow rapid on-site quantitative analysis of nitrite. The results showed a wide linear range (0.05 to 2.50 mg L^{-1}) with a low detection limit (15.0 µg L^{-1}–NO_2^-), good inter-day precision (1.93%RSD), and excellent accuracy (2.67% relative error). The application of the method developed to determine nitrite in seawater samples collected in Phuket showed a good correlation with results obtained from the standard spectrophotometric method. The colorimetric sheet developed can be produced at a cost of only USD0.04 per sensor, while the DIC can be conducted using the camera in a standard smartphone. Therefore, the method developed in this work represents a much easier, cheaper, and rapid method of on-site analysis of nitrite in water.

Compliance with ethical standards

References

1. Chan TY (1996) Food–borne nitrates and nitrites as a cause of methemoglobinemia. Southeast Asian J Trop Med Public Health 27:189–192. https://pubmed.ncbi.nlm.nih.gov/9031426/. Accessed 27 Oct 2020

2. Jensen FB (2003) Nitrite disrupts multiple physiological functions in aquatic animals. Comp Biochem Physiol A Mol Integr Physiol 135:9–24. https://doi.org/10.1016/s1095-6433(02)00323-9

3. Lundberg JO, Weitzberg E, Cole JA, Benjamin N (2004) Nitrate, bacteria and human health. Nat Rev Microbiol 2:593–602. https://doi.org/10.1038/nrmicro929

4. Suzuki H, Iijima K, Moriya A, McElroy K, Scobie G, Fyfe V, McColl KE (2003) Conditions for acid catalysed luminal nitrosation are maximal at the gastric cardia. Gut 52:1095–1101. https://doi.org/10.1136/gut.52.8.1095

5. Wang QH, Yu LJ, Liu Y, Lin L, Lu RG, Zhu JP, He L, Lu ZL (2017) Methods for the detection and determination of nitrite and nitrate: a review. Talanta 165:709–720. https://doi.org/10.1016/j.talanta.2016.12.044

6. Aydın A, Ercan Ö, Taşcıoğlu S (2005) A novel method for the spectrophotometric determination of nitrite in water. Talanta 66:1181–1186. https://doi.org/10.1016/j.talanta.2005.01.024

7. Burakham R, Oshima M, Grudpan K, Motomizu S (2004) Simple flow–injection system for the simultaneous determination of nitrite and nitrate in water samples. Talanta 64:1259–1265. https://doi.org/10.1016/j.talanta.2004.03.059

8. Tsikas D (2007) Analysis of the L–arginine/NO pathway. J Chromatogr B 851:51–70. https://doi.org/10.1016/j.jchromb.2007.02.020

9. Singh P, Singh MK, Beg YR, Nishad GR (2019) A review on spectroscopic methods for determination of nitrite and nitrate in

91

environmental samples. Talanta 191:364–381. https://doi.org/10.1016/j.talanta.2018.08.028

10. Choodum A, Boonsamran P, NicDaeid N, Wongniramaikul W (2015) On–site semi–quantitative analysis for ammonium nitrate detection using digital image colourimetry. Sci Justice 55:437–445. https://doi.org/10.1016/j.scijus.2015.05.001

11. Nam J, Jung IB, Kim B, Lee SM, Kim SE, Lee KN, Shin DS (2018) A colorimetric hydrogel biosensor for rapid detection of nitrite ions. Sensors Actuators B Chem 270:112–118. https://doi.org/10.1016/j.snb.2018.04.171

12. Fotoohi B, Kazemzad M, Mercier L (2018) Additive–free synthesis of robust monolithic mesoporous silica support used in catalysis. Ceram Int 44:20199–20210. https://doi.org/10.1016/j.ceramint.2018.08.003

13. Da'na E (2017) Adsorption of heavy metals on functionalized–mesoporous silica: a review. Microporous Mesoporous Mater 247:145–157. https://doi.org/10.1016/j.micromeso.2017.03.050

14. Choodum A, Kanatharana P, Wongniramaikul W, Nic Daeid N (2013) Using the iPhone as a device for a rapid quantitative analysis of trinitrotoluene in soil. Talanta 115:143–149. https://doi.org/10.1016/j.talanta.2013.04.037

15. Boos A, Intasiri A, Brunette JP, Leroy MJF (2002) Surfactant–templated silica doped with 1–phenyl–3–methyl–4–stearoylpyrazol–5–one (HPMSP) as a new sorbent. J Mater Chem 12:886–889. https://doi.org/10.1039/B110659G

16. Vazquez NI, Gonzalez Z, Ferrari B, Castro Y (2017) Synthesis of mesoporous silica nanoparticles by sol–gel as nanocontainer for future drug delivery applications síntesis de nanopartículas mesoporosas de sílice como futuros sistemas de liberación controlada de medicamentos. Bol SECV 56:139–145. https://doi.org/10.1016/j.bsecv.2017.03.002

17. Boonkanon C, Phatthanawiwat K, Wongniramaikul W, Choodum A (2020) Curcumin nanoparticle doped starch thin film as a green colorimetric sensor for detection of boron. Spectrochim Acta A 224:117351. https://doi.org/10.1016/j.saa.2019.117351

18. Choodum A, Keson J, Kanatharana P, Limsakul W, Wongniramaikul W (2017) Selective pre and post blast trinitrotoluene detection with a novel ethylenediamine entrapped thin polymer film and digital image colorimetry. Sensors Actuators B Chem 252:463–469. https://doi.org/10.1016/j.snb.2017.06.030

19. Choodum A, Malathong K, NicDaeid N, Limsakul W, Wongniramaikul W (2016) A cost effective hydrogel test kit for pre and post blast trinitrotoluene. Forensic Sci Int 266:202–208. https://doi.org/10.1016/j.forsciint.2016.05.036

20. Mehmeti E, Stanković D, Hajrizi A, Kalcher K (2016) The use of graphene nanoribbons as efficient electrochemical sensing material for nitrite determination. Talanta 159:34–39. https://doi.org/10.1016/j.talanta.2016.05.079

21. Danzer K, Currie LA (1998) Guidelines for calibration in analytical chemistry. Part I. Fundamentals and single component calibration (IUPAC Recommendations 1998). Pure Appl Chem 70:993–1014. https://doi.org/10.1351/pac199870040993

22. U.S. Environmental Protection Agency (2001) Method 1686 nitrate/nitrite–N in water and biosolids by manual colorimetry. https://www.epa.gov/sites/production/files/2015-10/documents/method_1686_draft_2001.pdf. Accessed 27 Oct 2020

23. Yi Z, Dumée LF, Garvey CJ, Feng C, She F, Rookes JE, Mudie S, Cahill DM, Kong L (2015) A new insight into growth mechanism and kinetics of mesoporous silica nanoparticles by in situ small angle X-ray scattering. Langmuir 31:8478–8487. https://doi.org/10.1021/acs.langmuir.5b01637

24. Li Z, Zhang Y, Feng N (2019) Mesoporous silica nanoparticles: synthesis, classification, drug loading, pharmacokinetics, biocompatibility and application in drug delivery. Expert Opin Drug Deliv 16:219–237. https://doi.org/10.1080/17425247.2019.1575806

25. Liu S, Peng Y, Chen J, Shi W, Yan T, Li B, Zhang Y, Li J (2018) Engineering surface functional groups on mesoporous silica: towards a humidity-resistant hydrophobic adsorbent. J Mater Chem A 6:13769–13777. https://doi.org/10.1039/C8TA04082F

26. Basso AM, Nicola BP, Bernardo-Gusmão K, Pergher SBC (2020) Tunable effect of the calcination of the silanol groups of KIT-6 and SBA-15 mesoporous materials. Appl Sci 10:970–985. https://doi.org/10.3390/app10030970

27. Shin DY, Yoon JH, Kim SH, Baik H, Lee SJ (2018) Immobilization of a porphyrinic Mn(iii) catalyst on a new type of silica support comprising a three–dimensionally interconnected network with two different sizes of pores. Catal Sci Technol 8:6306–6310. https://doi.org/10.1039/c8cy01886c

28. Li Y, Yang Q, Yang J, Li C (2006) Mesoporous aluminosilicates synthesized with single molecular precursor (sec–BuO)2AlOSi(OEt)3 as aluminum source. Microporous Mesoporous Mater 91:85–91. https://doi.org/10.1016/j.micromeso.2005.11.021

29. Zhang Z, Liu H, Wu L, Lan H, Qu J (2015) Preparation of amino–Fe(III) functionalized mesoporous silica for synergistic adsorption of tetracycline and copper. Chemosphere 138:625–632. https://doi.org/10.1016/j.chemosphere.2015.07.014

30. Kachbouri S, Mnasri N, Elaloui E, Moussaoui Y (2018) Tuning particle morphology of mesoporous silica nanoparticles for adsorption of dyes from aqueous solution. J Saudi Chem Soc 22:405–415. https://doi.org/10.1016/j.jscs.2017.08.005

31. Silva ACPD, Cordeiro PHY, Estevão BM, Caetano W, Eckert H, Santin SMO, Moisés MP, Hioka N, Tessaro AL (2019) Synthesis of highly ordered mesoporous MCM–41: selective external functionalization by time control. J Braz Chem Soc 30:1599–1607. https://doi.org/10.21577/0103-5053.20190058

32. Khan AJ, Song J, Ahmed K, Rahim A, Onófrio Volpe PL, Rehman F (2020) Mesoporous silica MCM–41, SBA–15 and derived bridged polysilsesquioxane SBA–PMDA for the selective removal of textile reactive dyes from wastewater. J Mol Liq 298:111957. https://doi.org/10.1016/j.molliq.2019.111957

33. Thommes M, Smarsly B, Groenewolt M, Ravikovitch PI, Neimark AV (2006) Adsorption hysteresis of nitrogen and argon in pore networks and characterization of novel micro and mesoporous silicas. Langmuir 22:756–764. https://doi.org/10.1021/la051686h

34. Taqanaki ER, Heidari R, Monfared M, Tayebi L, Azadi A, Farjadian F (2019) EDTA–modified mesoporous silica as supra adsorbent of copper ions with novel approach as an antidote agent in copper toxicity. Int J Nanomedicine 14:7781–7792. https://doi.org/10.2147/IJN.S218760

35. Lahtinen M, Kudva J, Hegde P, Bhat K, Kolehmainen E, Venkatesh N, Naral D (2014) Synthesis, characterization, thermal and antimicrobial studies of N–substituted sulfanilamide derivatives. J Mol Struct 1060:280–290. https://doi.org/10.1016/j.molstruc.2013.12.063

36. Topacli A, Kesimli B (2001) Investigation on sulfanilamide and its interaction with some metals and lincomycin by infrared spectroscopy. Spectrosc Lett 34:513–526. https://doi.org/10.1081/SL-100105097

37. Wongniramaikul W, Limsakul W, Choodum A (2018) A biodegradable colorimetric film for rapid low–cost field determination of formaldehyde contamination by digital image colorimetry. Food Chem 249:154–161. https://doi.org/10.1016/j.foodchem.2018.01.021

38. López Pasquali CE, Gallego-Picó A, Fernández Hernando P, Velasco M, Durand Alegría JS (2010) Two rapid and sensitive automated methods for the determination of nitrite and nitrate in soil samples. Microchem J 94:79–82. https://doi.org/10.1016/j.microc.2009.09.005

39. Li W, Zhang R, Wang H, Jiang W, Wang L, Li H, Wu T, Du Y (2016) Digital image colorimetry coupled with a multichannel

membrane filtration–enrichment technique to detect low concentration dyes. Anal Methods 8:2887–2894. https://doi.org/10.1039/C6AY00022C

40. U.S. Environmental Protection Agency (1987) Estimated national occurrence and exposure to nitrate and nitrite in public drinking water supplies. Washington, DC, pp 1–31. https://www.who.int/water_sanitation_health/dwq/chemicals/nitrate.pdf. Accessed 27 Oct 2020

41. World Health Organization (WHO) (2003) Nitrate and nitrite in drinking–water: background document for development of WHO guidelines for drinking–water quality. Geneva, pp 1–21. https://apps.who.int/iris/handle/10665/75380. Accessed 27 Oct 2020

42. Xiong Y, Wang CJ, Tao T, Duan M, Fang SW, Zheng M (2016) A miniaturized fiber-optic colorimetric sensor for nitrite determination by coupling with a microfluidic capillary waveguide. Anal Bioanal Chem 408:3413–3423. https://doi.org/10.1007/s00216-016-9415-1

Publisher's note Springer Nature remains neutral with regard to jurisdictional claims in published maps and institutional affiliations.

Paper II

Removal and recovery of phosphate using a novel calcium silicate hydrate composite starch cryogel

Taweekarn, T., Wongniramaikul, W., and Choodum, A.

Removal and recovery of phosphate using a novel calcium silicate hydrate composite starch cryogel

Tarawee Taweekarn, Worawit Wongniramaikul, Aree Choodum [*]

Integrated Science and Technology Research Center, Faculty of Technology and Environment, Prince of Songkla University, Phuket Campus, Kathu, Phuket, 83120, Thailand

ARTICLE INFO

ABSTRACT

Phosphate is a major pollutant that deteriorates water quality and causes eutrophication, a novel calcium silicate hydrate composite cryogel (Cry-CSH) was thus successfully prepared for phosphate removal and recovery in this work. Calcium silicate hydrate (C–S–H) was mixed with the gel precursor (7.5% w/w) prepared from native starch and limewater (saturated calcium hydroxide solution as the cross-linker). The mixture was frozen and thawed for 3 cycles giving an interconnected macroporous composite. This had C–S–H nanoparticles (75 mg) immobilized on a monolithic floatable cryogel network (2.5 cm diameter × 1.0 cm height) enabling an easier recovery and without the losses that occur when using C–S–H nanoparticles. The phosphate adsorption reaches equilibrium at 120 min with adsorption capacity of 2.50 $mgPO_4^{3-}/g_{Cry-CSH}$ (65.42 $mgPO_4^{3-}/g_{C-S-H}$) under optimum conditions. Adsorption equilibrium data were well fit by the Freundlich isotherm model, while kinetic results were well fit by the pseudo second-order model. The calculated activation energy (E_a) of 43.9 kJ/mol indicates chemical adsorption, while a positive change in enthalpy (ΔH^0, 19.3 kJ/mol) indicates the endothermic nature of phosphate adsorption. Cry-CSH can remove phosphate from wastewater and effluent samples with excellent removal efficiency (>98%). It can float on water surface for at least 105 days without damage, while its phosphate adsorbed form can be biodegraded within 10 days under soil buried conditions. Thus, this work demonstrated the significant potential of Cry-CSH for practical and environmentally friendly phosphate removal and recovery.

1. Introduction

Phosphorus is one of the most essential nutrients and contributes to agricultural and industrial development. Phosphate is the most common form of phosphorus nutrients and is considered a major pollutant that deteriorates water quality. Phosphate at concentrations between 25 μgL^{-1} and 0.03 mgL^{-1} (Almanassra et al., 2020) or above 0.02 mgL^{-1} (Seliem et al., 2016) can cause eutrophication, which is a the depletion of oxygen in water bodies induced by the over-production of algae and phytoplankton. This can cause a serious environmental problem (Almanassra et al., 2020; Huong et al., 2019; Seliem et al., 2016), as well as loss of income and economic disruptions, and effects on human health (Almanassra et al., 2021a, 2021b). As such, phosphate removal and maintaining its concentration at a low level in water is extremely significant to mitigate and control water eutrophication.

Calcium silicate hydrate (C–S–H) is a semi-crystalline material that has been reported to remove phosphate by crystallization (Lee et al.,

2018; Okano et al., 2016; Zhang et al., 2019). C–S–H can dissociate into calcium and silicate in water, and these aggregate or grow hydroxyapatite crystals with phosphorus on their surfaces (Okano et al., 2015). Since C–S–H would act as the calcium ion donor and the pH adjuster at the same time in the recovery process, it has been reported to be a phosphorus recovery material in biological wastewater treatment process with excellent biocompatibility and biodegradability (Lee et al., 2018; Okano et al., 2016; Zhang et al., 2019). It also exhibits better settleability than conventional calcium compounds with high capacity to crystallize with soluble phosphorus forms that can be used directly as fertilizer (Lee et al., 2018; Okano et al., 2013, 2015).

Various forms of C–S–H have been reported for phosphate removal and recovery. Porous C–S–H exhibits stronger capacity of calcium ion release than crystalline C–S–H as well as higher phosphate species recovery performance (Guan et al., 2013). C–S–H gel, metastable with respect to crystalline C–S–H, is supposed to have higher calcium ion releasing ability than crystalline C–S–H due to its higher solubility

(Maeda et al., 2018), although its removal efficiency is slightly lower than that of Ca(OH)$_2$ (Lee et al., 2018). Amorphous calcium silicate hydrates (A-CSHs) have also been reported for phosphorus recovery with higher potential for phosphorus removal than conventional crystalline C–S–H (Okano et al., 2013, 2015, 2016). Its precipitate also exhibited better settleability, filterability, and dewaterability than conventional CaCl$_2$ and Ca(OH)$_2$ (Okano et al., 2013, 2015, 2016). However, separation of fine crystallites after crystallization from these C–S–H is still difficult and this has limited practical applications to wastewater treatment and phosphorus recovery (Peng et al., 2018). A magnetic calcium silicate hydrate composite material (Fe$_3$O$_4$@CSH) has thus been developed to remove and recover phosphate via chemical adsorption in order to improve C–S–H efficiency and settleability (Peng et al., 2018). Although the Fe$_3$O$_4$@CSH materials are effective for phosphate adsorption with a maximum adsorption capacity of 55.84 mg phosphorus/g and could be quickly separated by an external magnet, calcium-containing chemical (e.g., CaCl$_2$, Ca(OH)$_2$) is required to be added to the alkaline solution to convert the phosphate to calcium phosphate fertilizer for use in agriculture (Peng et al., 2018). The C–S–H powder has also been immobilized in polyvinyl alcohol matrix (PVA-CSH) and then used for phosphate removal (Ding et al., 2018). Although the PVA-CSH can reduce the loss of C–S–H powder during removal process, PVA is a synthetic petroleum-based polymer that may affect environment along its lifetime from first time in synthesis and finally during degradation. The use of a natural polymer, e.g. starch, is thus a better choice to prepare a novel material for environmental pollutant removal that can remain environmentally friendly.

In this study, a novel starch based monolithic cryogel was composited with calcium silicate hydrate to develop a floatable bio-adsorbent for phosphate removal and recovery. The developed composite can reduce the loss of C–S–H powder as well as deal with fine particle adsorbent during removal process, and can be further directly used as fertilizer in agriculture. The as-prepared materials were characterized to better understand the adsorption mechanisms of phosphate as well as its adsorption kinetics and equilibrium isotherm models. The phosphate removal efficiency in both synthetic phosphate solution and real water sample containing phosphate was also investigated.

2. Materials and methods

2.1. Materials

Disodium hydrogen phosphate (Analytical Reagent grade) supplied by Ajax Finechem, (Sydney, Australia) was used to prepare stock solution (100 mgL^{-1}). Ammonium heptamolybdate tetrahydrate and potassium antimony tartrate were supplied by Carlo Erba (Val–de–Reuil, France), while ascorbic acid (Analytical Reagent grade) was purchased from Fisher scientific, (Leicestershire, UK). Calcium chloride (99%) and sodium silicate were purchased from Loba (Mumbai, India). Rice flour (Erawan Brand, Nakhon Pathom, Thailand) and cassava starch (Jaydee Brand, Nakhon Pathom, Thailand) were locally purchased from supermarket. Their amylose contents analyzed by spectrophotometer that referenced Thai agriculture standard TAS 4000–2003 (In-house method TE-PH-021 based on Quality and Testing of Thai Horn Mali Rice, 2004, Department of Agriculture, Thailand) were 23% and 27%, respectively. Ethanol (95%, commercial grade) was supplied by S.N.P. Scientific Co. Ltd. (Bangkok, Thailand). All standard solutions were prepared with ultrapure water purified by a water purification system (Merck, Darmstadt, Germany).

2.2. Preparation of calcium silicate hydrate composite starch based cryogel (Cry-CSH)

A rapid ultrasound-assisted sol–gel method was used to synthesize C–S–H at room temperature as reported in the literature (Zhang et al., 2019). Briefly, a CaCl$_2$ solution was added dropwise into a Na$_2$SiO$_3$

solution under ultrasound irradiation (300 W) in ultrasonic bath with Ca/Si molar ratios of 1.2 and a solid/liquid ratio of 1/8. White sol immediately occurred and gradually hardened, the sample was then taken out and gelled in a plastic container at room temperature. The obtained gel was then soaked with ultrapure water (10 gL^{-1}) for 1 h to remove free Ca(OH)$_2$ before filtering the suspension through a 0.45 μm membrane filter. The obtained C–S–H was then incubated at 80 °C for 24 h in an oven before keeping in desiccator for further use.

Starch based cryogel (Cry) was prepared by modifying the procedure to prepare famous Thai dessert "Lod-chong" coupled with conventional freeze and thaw technique. Rice flour (12.5 g) and tapioca starch (3.75 g) were dispersed in 130 mL of limewater, which is saturated calcium hydroxide solution prepared by dissolving red lime (RL) in ultrapure water (15 gL^{-1}) and kept for at least 3 days before taking the upper clear supernatant solution. The mixture was then gradually heated from 60 to 200 °C for 1.5 h until the starch completely gelatinized and became clear. In the case of Cry-CSH, the C–S–H (0.6–6 g) was added in starch gel (60 g) and further mixed to obtain homogenous mixture before cooling the mixture under continued stirring for 5 min. The mixture was tightly pulled into a 50 mL plastic syringe and then placed in a freezer for freezing at −20 °C for 24 h. The resultant monolith was then thawed at room temperature and a freeze and thaw process was repeated for three cycles. The cryogel was then removed from the container before cutting into smaller pieces (1 cm lengths). The obtained materials were then soaked in 95% ethanol for 24 h before drying in an oven at 100 °C until achieving the stable weight. All obtained cryogels were kept in zip-lock plastic bags and placed in desiccator until further use.

2.3. Characterization of C–S–H and Cry-CSH

The morphology of C–S–H, Cry, and Cry-CSH was investigated using field emission scanning electron microscopy (FE-SEM; FEI, Czech Republic). The functional groups of the materials were analyzed with Fourier transform infrared spectroscopy (FT-IR; Bruker, Germany) using ATR technique and KBr pellet at 4000-400 cm^{-1}, respectively. X-ray diffraction (XRD) patterns were obtained from X-ray diffractometer (Empyrean, PANalytical, Netherlands) using monochromatic Cu Kα radiation. The surface area, porosity, and pore size distribution of as-prepared materials were investigated using a high throughput surface area and porosity analyzer (ASAP2460, Micromeritics, USA). They were degassed at 105 °C for 30 min to remove physically absorbed gases from the sample surface before analyzing the nitrogen adsorption/desorption isotherm at 77 K. The specific surface area (S_{BET}) calculated using the Brunauer–Emmet–Teller (BET) method and the pore volume estimated from an adsorption branch using the Barrett, Joyner and Halenda (BJH) method were used to estimate the average pore diameter. The point of zero charge (pH$_{pzc}$) was investigated based on the pH measurement technique (Khormaei et al., 2007; Pavan et al., 2014). The pH of sodium chloride (NaCl) solution (0.1 M) was adjusted to desired pH in the range of 3–12 using HCl (0.01 M) and NaOH (0.1 M). The adsorbent (0.03 g) was then added into pH adjusted NaCl solution (50 mL) and shaken for 24 h. The supernatant was then separated by centrifugation before measuring the final pH. The point where the curve pH final versus pH initial crosses the line and equals to pH final is the pH$_{pzc}$ (Khormaei et al., 2007; Pavan et al., 2014).

The cryogel characteristics including swelling ratio, water uptake capacity, water retention, and porosity of Cry-CSH were investigated and are discussed in Supplementary material S1–S8.

2.4. Phosphate adsorption experiment

The phosphate adsorption experiments on C–S–H, Cry, and Cry-CSH were performed by a batch adsorption method at room temperature (25 °C). The materials were added to 50 mL phosphate standard solution in conical flasks and stirred at 150 rpm under the required conditions along with the blank control (without adsorbent). The phosphate

solutions were maintained at an initial pH without pH adjustment (~5.5) unless otherwise stated. The solutions were collected at pre-determined time intervals, filtered using a 0.20 μm cellulose acetate membrane filter, and analyzed using spectrophotometer based on the standard ascorbic acid method (APHA-AWWA-WEF, 1998). A calibration curve was established to ensure the accuracy of the measurements by analyzing a series of phosphate standard solutions in the range from 0 to 2.5 mgL^{-1}.

The adsorbent doses of C–S–H and Cry-CSH were optimized before using in adsorption experiments by adding the C–S–H (0.1, 0.25, 0.5, 1, 1.5, 2, 2.5 g) and 1 g Cry-CSH (1.0, 2.5, 5.0, 7.5, 10%w/w) into 50 mgL^{-1} phosphate solution. The suspended solutions were shaken at 150 rpm at room temperature for 2 h.

Adsorption isotherm experiments were done by suspending the adsorbents at their optimum amount in 50 mL phosphate solutions with initial phosphate concentrations in the range from 0.1 to 100 mgL^{-1}. Similar runs were performed for a range of contact times (0–1440 min), pH (5–8), and temperatures (25 °C–45 °C) at the optimum initial concentration for kinetic studies. The amount of adsorbed phosphate at time t (Q$_t$: mgPO$_4$$^{3-}$/g) was calculated as the difference between phosphate concentrations in solution initially (C$_i$: mgL^{-1}) and at time t (C$_t$: mgL^{-1}) using the following equation (1) (Almanassra et al., 2020; Peng et al., 2018; Zhang et al., 2019):

$$Q_t = \frac{(C_i - C_t)}{W} \times V \tag{1}$$

where V is the volume of solution (L) and W is the dry mass of adsorbents (g). The phosphate removal efficiency (RE) was calculated using equation (2) where C$_e$ is the phosphate concentration at equilibrium (mgL^{-1}). Each experiment was performed for three replicates and the average of these values was used in plots or any relationships.

$$\%RE = \frac{(C_i - C_e)}{C_i} \times 100 \tag{2}$$

2.5. Phosphate adsorption model

To understand the adsorption mechanisms of phosphate on the C–S–H and Cry-CSH, appropriate chemical models were investigated. Kinetics of phosphate removal were evaluated using three kinetic adsorption models, namely the Lagergren pseudo-first order (Sen Gupta and Bhattacharyya, 2011; Yuh-Shan, 2004) and the pseudo second-order (Ho, 2006; Sen Gupta and Bhattacharyya, 2011), and intra-particle diffusion (Seliem et al., 2016; Sen Gupta and Bhattacharyya, 2011), to determine the adsorption capacity and the rate limiting step. The obtained adsorption data were analyzed and fit with kinetic adsorption models. The Lagergren pseudo-first order model is expressed in equation (3) which could be integrated for the boundary conditions t = 0, Q$_t$ = 0 and t = t, Q$_t$ = Q$_t$ to get equation (4):

$$\frac{dQt}{dt} = k_1(Q_e - Q_t) \tag{3}$$

$$\ln(Q_e - Q_t) = \ln Q_e - k_1 t \tag{4}$$

where Q$_e$ and Q$_t$ are the phosphate adsorbed (mgPO$_4$$^{3-}$/g) at equilibrium time (min) and at time t (min), respectively. The k$_1$ is the pseudo first-order kinetic rate constant (min^{-1}) which can be obtained from the slope of the linear plot between ln(Q$_e$ − Q$_t$) and t. The pseudo second-order model is investigated on the basis of equation (5) which could be integrated for the boundary conditions t = 0, Q$_t$ = 0 and t = t, Q$_t$ = Q$_t$ as in equation (6), where k$_2$ is the second order kinetic rate constant (min^{-1}) which can be obtained from the slope of the linear plot between t/Q$_t$ and t.

$$\frac{dQt}{dt} = k_2(Q_e - Q_t)^2 \tag{5}$$

$$\frac{t}{Q_t} = \frac{1}{k_2 Q_e^2} + \frac{1}{Q_e} t \tag{6}$$

The kinetic equations for pseudo first-order and second-order in terms of concentration and time are also discussed in Supplementary material, Table S9. The intra-particle diffusion can be estimated using equation (7) (Seliem et al., 2016; Sen Gupta and Bhattacharyya, 2011) where k$_p$ is the rate constant of intra-particle diffusion (mg/g/min$^{1/2}$) that can be obtained from the slope of the plot of Q$_t$ against t$^{1/2}$ and c is the intercept related to the thickness of the boundary layer. If the trend-line of the plot is linear and passes through the origin, intra-particle diffusion is the only rate controlling step (Almanassra et al., 2020; Seliem et al., 2016).

$$Q_t = k_p t^{1/2} + c \tag{7}$$

Adsorption isotherm of phosphate on C–S–H and Cry-CSH was also investigated in order to further understand the adsorption mechanism. The adsorbents were placed into phosphate solution at various initial concentrations to explore the adsorption of phosphate onto these particles in sufficient time. The adsorbed phosphate was then plotted versus the residual phosphate in the solution. The two isotherm models typically used, i.e. Langmuir and Freundlich, were adopted to fit and analyze the experimental data. Langmuir isotherm equation can be written as in equations (8) and (9) (Langmuir, 1918; Seliem et al., 2016) where C$_e$ is the equilibrium concentration of the remaining phosphate in the solution (mgL^{-1}), Q$_e$ is the amount of phosphate adsorbed per mass unit of the adsorbent at equilibrium (mg/g), Q$_{max}$ is the amount of phosphate per mass unit of adsorbent at complete monolayer coverage (mg/g), and k$_L$ is the Langmuir constant relating to the strength of adsorption (L^{-1}mg). Q$_{max}$ and k$_L$ can be determined from the slope and intercept of the linear plot between 1/Qe and 1/Ce, respectively. The Freundlich isotherm is expressed in equations 10 and 11 where k$_F$ and n are the Freundlich constants related to adsorption capacity and intensity, respectively. The values of k$_F$ and 1/n can be obtained from the intercept and slope of the linear regressions fit to log Q$_e$ versus log C$_e$.

$$Q_e = \frac{Q_{max} k_L C_e}{1 + k_L C_e} \tag{8}$$

$$\frac{1}{Q_e} = \frac{1}{k_L Q_{max}}\left(\frac{1}{C_e}\right) + \frac{1}{Q_{max}} \tag{9}$$

$$Q_e = k_F C_e^{\frac{1}{n}} \tag{10}$$

$$\log Q_e = \log k_F + \frac{1}{n}\log C_e \tag{11}$$

The thermodynamics of phosphate adsorption on C–S–H and Cry-CSH were investigated over the temperature range from 25 to 45 °C to study the effects of temperature on the adsorption and to estimate the changes of thermodynamic factors including Gibbs free energy (ΔG^0), enthalpy (ΔH^0), and entropy (ΔS^0). ΔG^0 can explain the spontaneity and feasibility of the removal process and can be determined from the classical Van't Hoff equation (12) at any temperature:

$$\Delta G^0 = -RT \ln k_d \tag{12}$$

where T is the temperature (K), R is the gas constant (8.314 J/mol/K), and k$_d$ is the constant of thermodynamic equilibrium that can be calculated using equation (13):

$$k_d = \frac{C_a}{C_e} \tag{13}$$

where C$_a$ is the extent of pollutant adsorbed on the adsorbent at saturation (mgL^{-1}). ΔH^0 provides information about the nature of adsorption process, whether it is exothermic or endothermic, while ΔS^0 can explain the degrees of freedom in the system or the extent of order/

disorder of the molecules (Almanassra et al., 2020). Both ΔH^0 and ΔS^0 are linked to ΔG^0 by equation (14):

$$\Delta G^0 = \Delta H^0 - T\Delta S^0 \qquad (14)$$

When equations (10) and (12) are combined, ΔH^0 and ΔS^0 are obtained from the slope and the intercept as in equation (15):

$$ln k_d = \frac{\Delta S^0}{R} - \frac{\Delta H^0}{R}\left(\frac{1}{T}\right) \qquad (15)$$

2.6. Biodegradation of the Cry-CSH

Biodegradation of the Cry-CSH and phosphate adsorbed Cry-CSH ($PO_4{}^{3-}$–Cry-CSH) were investigated using a soil burial test (Junlapong et al., 2020). Swollen Cry-CSHs and $PO_4{}^{3-}$–Cry-CSH were buried at 10 cm depth under the surface of soil. They were taken out every 3 days and washed thoroughly to remove the soil as much as possible before weighing the remaining weight (W_b). The percentage of weight remaining was calculated using equation (16) where W_e is the weights of the swollen Cry-CSHs and W_b is the weights of Cry-CSHs after soil burial.

$$\text{Weight remaining } (\%) = 100 \times \frac{W_b}{W_e} \qquad (16)$$

3. Results and discussion

3.1. Preparation of Cry-CSH

A novel calcium silicate hydrate composite cryogel based on native starch (Cry-CSH) was successfully synthesized for phosphate removal and recovery. Prepared C–S–H was added in a gel precursor, containing rice flour, tapioca starch, and limewater, before following the freeze and thaw technique to produce a composite monolithic cryogel. Due to the high pH of limewater (pH ∼ 11.8), hydroxyl groups of starch have oxidized making their sites ionic cross-linking with the Ca^{2+} or $Ca(OH)^+$ of dissociated limewater and tightening the starch chain (Bryant and Hamaker, 1997; Chanjarujit et al., 2018). However, our recent work found that no new chemical bond has been observed in FTIR spectrum of the obtained cryogel with Ca^{2+}, Ca^{2+} thus may interact with starch molecules by a physical cross-linking via van der Waals interactions as in prior reports (Cornejo-Villegas et al., 2018; Pineda-Gómez et al., 2012). For Cry-CSH, C–S–H was added after gelatinization of starch, the Si–O from C–S–H molecules can interact with available hydroxyl groups of starch as shown in the proposed mechanism in Fig. 1. Prepared gel precursor with and without C–S–H (Cry-CSH and Cry, respectively) was then transferred into the container (50-mL plastic tube) and frozen. This made water in polymeric matrix freeze to ice crystals, while non-frozen

Ca-starch phase for Cry and Ca-Starch-CSH for Cry-CSH may continue cross-linking between Ca^{2+}, C–S–H and starch molecules for the formation of relatively thin walls (Mattiasson et al., 2009). The materials were then allowed to thaw at room temperature making the ice crystals melt and leaving an interconnected macroporous sponge-like material. The obtained Cry and Cry-CSH had similar appearances and tolerated compression without damage, indicating high elasticity which is a cryogel characteristic. In addition, Cry-CSH can float on water surface for at least 105 days without any damage.

3.2. Characterization of Cry-CSH

The FESEM images of the prepared C–S–H, Cry, and Cry-CSH are shown in Fig. 2. SEM images of the Cry (Fig. 2a) revealed macropores in interconnected polymer network, similar to those synthesized using other polymers (Choodum et al., 2016; Lozinsky, 2008). The C–S–H nanoparticles showed an agglomeration of crystalline nanoparticles with rough surface (Fig. 2b). When C–S–H was added into a gel precursor to produce the Cry-CSH, the nanoparticles would be trapped within the walls of the cryogel (Fig. 2c–d) resulting in thicker walls.

The adsorption based average pore diameter from the BET analysis of Cry was 0.39 nm with specific surface area (S_{BET}) of 0.7142 m^2g^{-1} and low total pore volume of 0.001 mLg^{-1}. The obtained surface area corresponded to other reports showing low specific surface areas, e.g. 0.6–7.7 m^2g^{-1} (Baudron et al., 2019), for porous material synthesized from native starch using freeze-drying. The S_{BET} of C–S–H was found to be much higher at 85.22 m^2g^{-1} than that of Cry, as in previous syntheses using the same method (17.31 m^2g^{-1} to 37.20 m^2g^{-1}), but with a lower total pore volume (0.020 mLg^{-1} compared to 0.0651 mLg^{-1} to 0.1779 mLg^{-1} (Zhang et al., 2019)). The average pore diameter of C–S–H (1.05 nm) was larger than that of Cry, but smaller than in previous work (∼15 nm (Zhang et al., 2019)). As expected, the S_{BET} of Cry-CSH (11.03 m^2g^{-1}) and total pore volume (0.003 mLg^{-1}) were lower than of C–S–H, but higher than of Cry, while the average pore diameter (0.97 nm) was larger than that of Cry, but smaller than that of C–S–H. Although the prepared Cry-CSH had larger S_{BET} than PVA-CSH (4.12 m^2g^{-1}), its total pore volume was less than that of PVA-CSH (0.01 mLg^{-1}) (Ding et al., 2018). The pore size distributions of C–S–H, Cry, and Cry-CSH (S10) calculated by the non–local density functional theory (NLDFT) based on a N_2-DFT model (a mathematical method to model the properties of the sorptive fluid (nitrogen) confined in porous solids) showed the most pore volume for the pore width from ∼5 to 50 nm in the mesopore range, although macropores (>50 nm) were also observed. All prepared materials exhibited a typical type IV adsorption isotherm (S11) where the capillary condensation occurred after multilayer adsorption of N_2 within mesopores (Thommes et al., 2015) confirming the presence of mesopores in all cases. They revealed an H3 hysteresis (which the lower limit of the desorption branch is located at the cavitation-induced P/P_0) indicating slit-shaped pores formed by non-rigid aggregates of plate-like particles and/or pore network consisting of macropores which are not completely filled with pore condensate (Thommes et al., 2015). The open hysteresis loops observed for Cry could be attributed to non-rigid structure of the Cry synthesized from starch, so that it may deform (swell) during adsorption or pore filling. The trapped nitrogen also cannot be released due to the affinity of nitrogen in cryogel caused by the heterogenous Cry surfaces (Qi et al., 2017). The addition of C–S–H in starch gel precursor made the Cry-CSH show closed H3 hysteresis similar to C–S–H, indicating more rigid structure with less swelling than for Cry.

The XRD patterns of the prepared C–S–H, Cry, and Cry-CSH are shown in Fig. 3. The diffraction peaks at 29.1°, 31.9° and 49.9° indicated relatively ordered structure in the prepared C–S–H (Franceschini et al., 2007; Zhang et al., 2019), while the peaks at 29.4°, 36.0°, 39.4°, 43.1°, 47.5° and 48.5° indicated the presence of calcite due to unavoidable contact with atmospheric carbon dioxide during the synthesis (Zhang et al., 2019). The diffraction peak observed ∼6.9° was attributed to the (001) reticular planes with distance given by the Bragg relation of 12.8
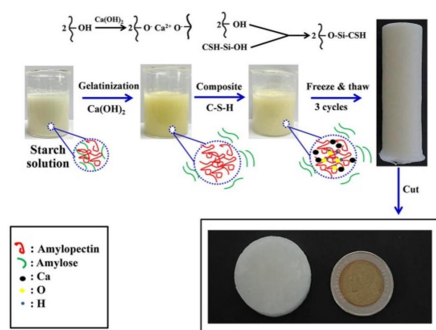

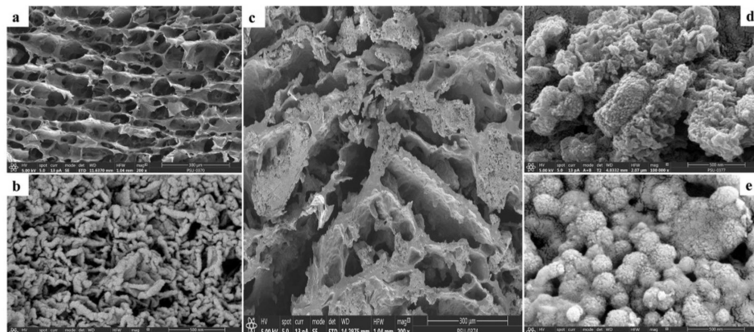**Fig. 1.** Proposed mechanism for synthesis of Cry-CSH.

98

T. Taweekarn et al.   Journal of Environmental Management 301 (2022) 113923

Fig. 2. FESEM images of (a) Cry, (b) C–S–H, and (c–d) Cry-CSH before (e) after adsorption of phosphate.
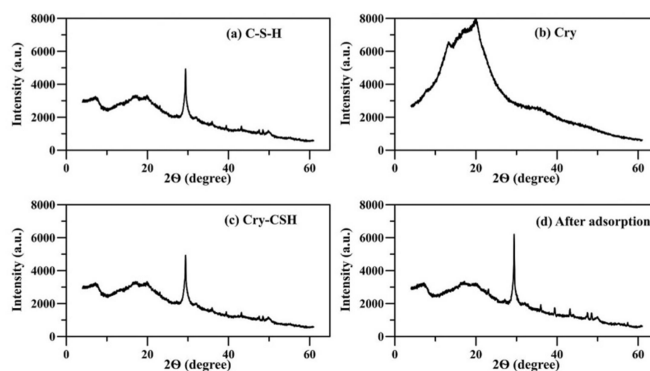

Fig. 3. The XRD patterns of (a) C–S–H, (b) Cry, (c) Cry-CSH before, and (d) after adsorption of phosphate.

Å, corresponding to the interlamellar distance reported previously for C–S–H (12 Å$\leq$ d001 $\leq$ 14 Å) (Franceschini et al., 2007). The three most intense bands at higher angles are attributed to the (hk0) reticular planes, which are characteristic of the organization of calcium atoms within each C–S–H layer with the distances of 3.06, 2.80 and 1.83 Å for d110, d200 and d020, respectively (Franceschini et al., 2007). The XRD patterns of Cry indicated the loss of starch crystallinity by a broad hump centered at 2θ ~20° for the amorphous structure, instead of the sharp peaks at 13.2° and 19.9° from V-type crystalline structure of starch (Chanjarujit et al., 2018; Domene-López et al., 2019). The loss of

crystallinity in Cry was caused by the crystallinity of starch granule being disrupted during gelatinization at an elevated temperature (Cornejo-Villegas et al., 2018) and the cross-linking with Ca²⁺. For Cry-CSH, the broad hump indicating amorphous structure of Cry remained in the pattern as well as the characteristic peaks of C–S–H, but with lower intensities for both. This indicates that the in-plane organization of the calcium atoms in Cry-CSH was the same as in C–S–H and intercalation of cryogel inside the interlayers of C–S–H does not occur as a basal distance larger than 14 Å was not observed (Franceschini et al., 2007).

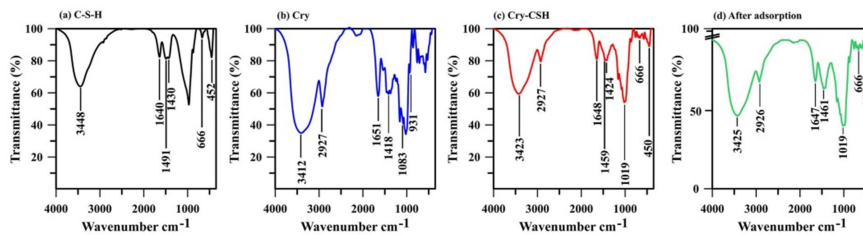The FTIR spectrum of C–S–H revealed the O–H stretching absorption

Fig. 4. The FTIR spectra of (a) C–S–H, (b) Cry, (c) Cry-CSH before, and (d) after adsorption of phosphate.

band at 3448 cm^{-1} from water molecules (García-Lodeiro et al., 2008; Yu et al., 2004). This band was also observed in Cry at 3412 cm^{-1} (Fig. 4), attributed to hydroxyl groups in starch molecules which may interact with Ca^{2+} located in their surroundings, as reported previously (Pineda-Gómez et al., 2012). This peak was observed at a wavelength between C–S–H's and Cry's, i.e. 3423 cm^{-1}, for Cry-CSH. The absorption band at 1640 cm^{-1} in C–S–H was attributed to H–O–H bending from water molecules (García-Lodeiro et al., 2008; Yu et al., 2004), while it shifted to 1648 and 1651 cm^{-1} in Cry-CSH and Cry, respectively, due to interactions with Ca^{2+} located in the surroundings and/or overlap with the C–O bending in amylopectin. The peaks observed at 1491 and 1430 cm^{-1} in C–S–H spectrum were assigned to C–O asymmetric stretching vibrations of carbonate (García-Lodeiro et al., 2008; Yu et al., 2004), which seems to overlap with the vibrations of C–H symmetrical scissoring of CH$_2$OH moiety in amylopectin observed at 1418 cm^{-1} (Cornejo-Villegas et al., 2018) in Cry, and appearing at 1459 and 1424 cm^{-1} in the composite. The intense band at 970 cm^{-1} in the spectrum is attributed to Si–O stretching vibrations also overlapping the intense peaks from 1083 cm^{-1} to 931 cm^{-1} contributed by vibrations of C–O bonding in amylopectin (Boonkanon et al., 2020; Choodum et al., 2019) in Cry and presented maximum absorption at 1019 cm^{-1} in Cry-CSH. The Si–O–Si bending was also observed in C–S–H and Cry-CSH spectra at 666 cm^{-1} (García-Lodeiro et al., 2008; Yu et al., 2004), while absorption peak at ~450 to 452 cm^{-1} in both materials was associated with the deformation of SiO$_4$ tetrahedra (Yu et al., 2004). An intense peak appeared in Cry and Cry-CSH at ~2927 cm^{-1} contributed by the C–H stretching in starch molecules, while the peaks at ~1156 cm^{-1} were contributed by C–O–C vibrations in glycosidic linkage (Cornejo-Villegas et al., 2018; Wongniramaikul et al., 2018).

3.3. Phosphate adsorption by Cry-CSH

3.3.1. The optimum amounts of adsorbents

The optimum amount of C–S–H for phosphate removal was investigated by varying doses of C–S–H for adsorption of 50 mgL^{-1} phosphate. The results showed that increasing the amount of C–S–H from 0.1 to 1.0 g increased the %removal efficiency from 95.12 ± 0.08 to 99.39 ± 0.02% (Fig. 5a) and this thereafter remained constant. Since a high amount of adsorbent can slow down the adsorption by resistance to mass transfer between adsorbate with adsorbent in a limited space in container (Mezenner and Bensmaili, 2009; Torit and Phihusut, 2019), 0.1 g C–S–H was then selected for further investigation. When C–S–H was composited with macroporous material in Cry-CSH, increasing the amount of C–S–H from 0 to 0.1 g (in 1 g Cry-CSH; 0 to 10%w/w C–S–H in gel precursor) showed increased %removal efficiency from 12.59 ± 2.34 to 94.19 ± 0.18% at 0.075 g C–S–H (7.5%w/w) and this remained constant after that (Fig. 5b). Thus, C–S–H was added to gel precursor for 7.5% to prepare Cry-CSH. It is worth noting that Cry (cryogel without C–S–H) could adsorb phosphate for 12.59 ± 2.34% due to the cross-linked Ca^{2+} in its structure.

3.3.2. Influence of contact time

Effect of adsorption time on phosphate removal efficiency is shown in Fig. 5c. It was found that C–S–H could adsorb phosphate with as high efficiency as 79.65 ± 0.08% within 5 min and then increased to 94.42 ± 0.14% within 90 min and remained constant after that. The results indicate rapid equilibration that can be attributed to the superior physicochemical adsorption of phosphate, as specific surface properties contribute to accelerated phosphate adsorption (Peng et al., 2018). In the case of Cry-CSH, it adsorbed phosphate slower than C–S–H. It could remove phosphate for 11.11 ± 0.81% at 5 min and then increase to 95.69 ± 2.81% at 60 min and slightly increase further to 97.62 ± 0.90% after 120 min. This may be because the cryogel matrix can decrease the reaction rate and thus prolong the equilibration time, as reported for PVA-CSH (Ding et al., 2018).

The FESEM image of Cry-CSH after adsorption of phosphate for 2 h showed spherical particles of amorphous calcium phosphate (ACP) (Fig. 2d) similar to those reported previously (Zhang et al., 2019). The presence of phosphorus is also evidenced in Cry-CSH after phosphate adsorption from SEM-EDX results (S12). Similar XRD patterns were observed for Cry-CSH before and after adsorption of phosphate for 2 h (Fig. 3) as in previous work where no difference was detected in the XRD pattern within 2 h because the ACP would begin to turn to hydroxyapatite (HAP) after 8 h and was completely converted at 24 h (Zhang et al., 2019). Although the presence of Ca(H$_2$PO$_4$)$_2$ and CaHPO$_4$ have been evidenced in the C–S–H after phosphate adsorption (Peng et al., 2018; Zhang et al., 2019), the H$_2$PO$_4^-$ and HPO$_4^{2-}$ V$_3$ vibration commonly present at 1038 cm^{-1} (Peng et al., 2018) or 1046 cm^{-1} (Zhang et al., 2019) overlapped with vibration bands from starch in Cry-CSH (Fig. 4).

3.3.3. Influence of pH

Influence of pH on phosphate removal efficiency was investigated in the range from 5 to 8 (Fig. 5d). Slight decrease of removal efficiency was observed for both C–S–H and Cry-CSH with increasing pH that may relate to the charge on the material surfaces as well as to the physicochemical behavior of phosphate in water in this pH range. The study of the point of zero charge (pH$_{pzc}$) of the adsorbents showed pH$_{pzc}$ of C–S–H and Cry-CSH at 7.0 and 6.8, respectively (S13), indicating positive charge on the adsorbent surfaces when the pH of the phosphate solution is less than pH$_{pzc}$ (Dai, 1994; Jun et al., 2020; Pavan et al., 2014). In addition, both Cry and Cry-CSH as the pH adjuster can release appropriate concentrations of OH$^-$ to maintain the final pH between 9.2 and 10.4 regardless of initial pH and presence of Ca^{2+} on the surfaces. While the dominant phosphate anions at pH from 5 to 8 are H$_2$PO$_4^-$ and HPO$_4^{2-}$. Thus, higher phosphate removal efficiency was achieved at lower initial pH because the positively charged surfaces could attract the negatively charged phosphate ions electrostatically. However, removal efficiency of ~98.5% was achieved at pH ~6.5 which is a typical pH for an effluent. Thus, there is no need for pH adjustment which is a potential cost in a real application.
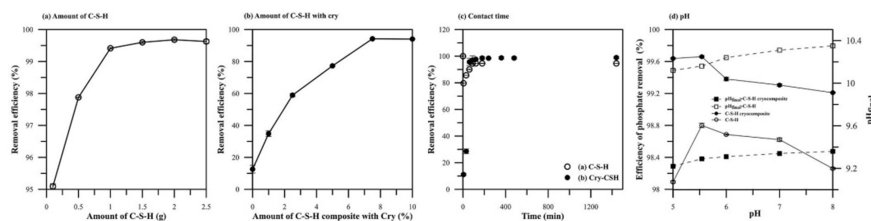

Fig. 5. Influence of (a) amount of C–S–H, (b) amount of C–S–H in Cry-CSH, (c) contact time, and (d) pH on %removal efficiency.

3.3.4. Adsorption isotherms

The adsorption capacities of C–S–H and Cry-CSH were determined at different initial phosphate concentrations (Fig. 6a–b) and the most commonly used Langmuir and Freundlich models were applied to fit the adsorption behavior of phosphate on both materials. Both nonlinear and linear fitting methods were applied and the goodness of equilibrium model fits in terms of the sum of the square of the errors (SSE), the residual standard deviation (SD), and the determination coefficient (R^2) (Almanassra et al., 2020) are listed in Table 1. The experimental results from C–S–H were fitted with the Langmuir model in its linearized form as in a previous report (Zhang et al., 2019). The R^2, SSE and SD values were best for nonlinearly fitted Freundlich model as in prior literature (Peng et al., 2018). These results imply that the adsorbed phosphate might form a monolayer surface coverage with possibly some heterogeneity on C–S–H (Almanassra et al., 2020) and chemisorption is the predominant adsorption mechanism (Peng et al., 2018). One of the important characteristics of Langmuir isotherm could be expressed by a dimensionless constant, known as the equilibrium parameter R_L (Almanassra et al., 2020; Seliem et al., 2016):

$$R_L = \frac{1}{1 + K_L C_0} \tag{17}$$

where C_0 is the initial phosphate concentration. R_L from 0.08 to 0.99 were obtained for adsorption of phosphate on C–S–H indicating that the adsorption process is favorable, which confirms that the Langmuir model is suitable for the adsorption of phosphate on C–S–H.

When C–S–H was composited with macroporous cryogel, Cry-CSH showed the best nonlinear fit with the Freundlich model, implying

Table 1
Phosphate adsorption and model parameters fit for C–S–H and Cry-CSH.

Model	Parameter	C–S–H		Cry-CSH	
		Linear	Non-linear	Linear	Non-linear
Langmuir	Q_m (mg PO_4^{3-}/g)	1.21	263830	−0.36	233552
	K_L (L/mgPO_4^{3-})	0.12	0.000001	−0.68	0.000006
	R^2	0.9980	0.8181	0.9596	0.7746
	SD	4.47	0.74	1.57	0.67
	SSE	120	3.29	12.40	2.25
Freundlich	K_F (mg^{1-n} L^n/g)	0.21	0.10	0.92	0.87
	1/n	1.20	1.75	1.78	1.73
	R^2	0.9740	0.9985	0.9912	0.9962
	SD	0.19	0.07	0.08	0.12
	SSE	0.21	0.03	0.03	0.07

that the adsorption is not limited to a monolayer coverage on heterogeneous surface (Almanassra et al., 2020). The heterogeneous factor (1/n) related to adsorption intensity or surface heterogeneity was 1.78 implying that cooperative adsorption can be occurring among active sites with different adsorption capacities (Liu, 2015; Madaeni and Salehi, 2009). This may be contributed by Ca^{2+} moiety in the cryogel structure combined with Ca^{2+} from composited C–S–H resulting in great heterogeneity. The adsorption of phosphate on Cry-CSH probably occurs on multilayers with Ca^{2+} moiety, in 1) both cryogel and C–S–H surface and surroundings, 2) Ca–OH linkages from C–S–H immobilized on Cry-CSH through ion exchange with OH^-, forming $Ca(H_2PO_4)_2$ and/or $CaHPO_4$.
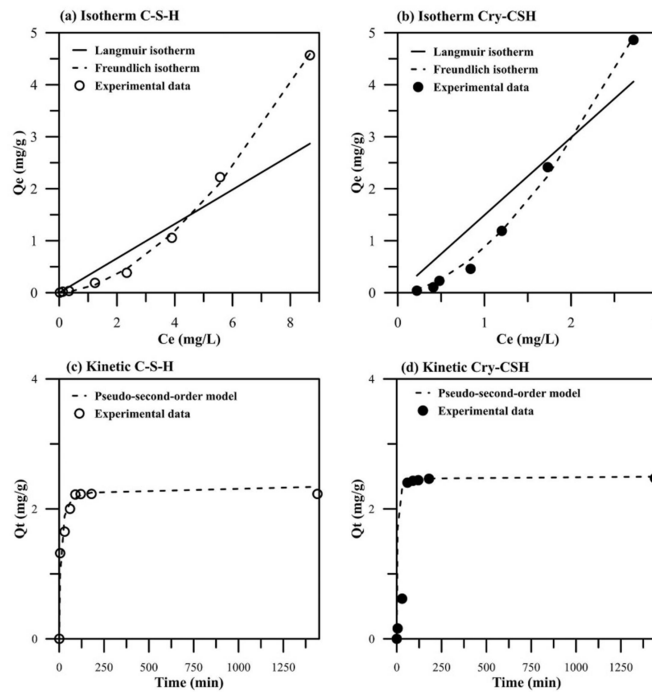

Fig. 6. (a–b) Adsorption isotherms, and (c–d) adsorption kinetics of phosphate on C–S–H and Cry-CSH.

3.3.5. Adsorption kinetics

The adsorption of phosphate on C–S–H and Cry-CSH for 5–1440 min at 25–45 °C is illustrated in Fig. 6c–d. These experimental results were fitted with pseudo-first-order and pseudo-second-order kinetic models and the model-based estimates of equilibrium are given in Table 2. Since the correlation coefficients (R^2) of the pseudo-second-order model for both materials are quite close to 1.0 (0.9972–0.9995 for C–S–H and 0.9999 to 1.0000 for Cry-CSH), this model was the better one for describing the phosphate adsorption, indicating chemisorption. The k_2 for C–S–H increased from 0.06 to 0.20 g/mg/min and from 0.17 to 0.52 g/mg/min for Cry-CSH when increasing the temperature from 25 °C to 45 °C, indicating that the removal of phosphate by both materials was endothermic. The kinetic parameters at 25 °C were also estimated using the amount of C–S–H (0.075 g) immobilized in Cry-CSH (1 g) and Qe = 64.52 mgPO_4^{3-}/g$_{CSH}$, k_2 = 0.0007 g$_{CSH}$/mgPO_4^{3-}/min, R^2 = 0.997 were obtained. It be noted that k_2 for C–S–H (0.06 g$_{CSH}$/mgPO_4^{3-}/min) was much higher than that of C–S–H in Cry-CSH (0.0007 g$_{CSH}$/mgPO_4^{3-}/min), maybe because the cryogel matrix decreased the reaction rate and prolonged the equilibration time. This estimated k_2 value was lower than those reported for PVA-CSH (0.0008 g/mg/min) (Ding et al., 2018), which may be due to the smaller pore size of Cry-CSH (0.97 nm compared to 24.937 nm (Ding et al., 2018)). However, the estimated Qe of C–S–H in Cry-CSH was 64.52 mgPO_4^{3-}/g$_{CSH}$, higher than that reported for PVA-CSH (28.15 mg/g$_{CSH}$) (Ding et al., 2018) due to the larger specific surface area of Cry-CSH (11.03 m^{2}g^{-1} compared to 4.123 m^{2}g^{-1} (Ding et al., 2018)). The removal capacity of phosphate by Cry-CSH was compared with those reported in the literature as shown in Table 3.

The half-life ($t_{1/2}$) of adsorption is the time needed to adsorb 50% of the adsorbed phosphate at equilibrium (Almanassra et al., 2020) was also estimated using equation (18). The half-life of adsorption by C–S–H decreased from 7.12 min at 25 °C to 2.09 min at 45 °C, and from 2.36 min at 25 °C to 0.77 min at 45 °C for Cry-CSH, confirming the faster adsorption kinetics at elevated temperatures.

$$t_{1/2} = \frac{1}{k_2 Q_e} \qquad (18)$$

Since the adsorption process relates to transport of phosphate ions from the aqueous solution to the surfaces of C–S–H and Cry-CSH, possibly followed by intra-particle diffusion, the intra-particle diffusion based kinetic model was also investigated to obtain better knowledge of the adsorption mechanisms. The plot shown in S14 is not linear and does not pass through the origin, indicating that more than one step controls the adsorption process. The first steep slope is associated with the diffusion of phosphate ions from solution across the boundary layer surrounding C–S–H and Cry-CSH to the external surface of the

Table 2
Kinetic parameters for phosphate adsorption by C–S–H and Cry-CSH.

Model	Temperature	Parameter	C–S–H	Cry-CSH
Pseudo-first-order	25	Qe (mg/g)	1.07	1.34
		k_1 (min^{-1})	0.0075	0.018
		R^2	0.9673	0.8562
	35	Qe (mg/g)	1.09	0.70
		k_1 (min^{-1})	0.024	0.011
		R^2	0.8785	0.9305
	45	Qe (mg/g)	0.98	0.73
		k_1 (min^{-1})	0.0275	0.026
		R^2	0.7952	1.0000
Pseudo-second-order	25	Qe (mg/g)	2.34	2.50
		k_2 (g/mg/min)	0.06	0.17
		R^2	0.9972	1.000
	35	Qe (mg/g)	2.42	2.49
		k_2 (g/mg/min)	0.12	0.26
		R^2	0.9995	0.9999
	45	Qe (mg/g)	2.39	2.48
		k_2 (g/mg/min)	0.20	0.52
		R^2	0.9995	1.000

Table 3
The phosphate removal capacities of various adsorbents.

Adsorbent	Removal capacity (mg PO_4^{3-}/g$_{active\ material}$)	pH	Time (min)	Temperature (K)	Reference
MCM-41	21.01	6.15	240	298	Seliem et al. (2016)
CDC*	16.14	0.12	360	298	Almanassra et al. (2020)
C–S–H	24.5	5.0	30	298	Okano et al. (2013)
C–S–H	109.4	5	240	298	Zhang et al. (2019)
PVA-CSH	28.15	7.50	600	298	Ding et al. (2018)
Cry-CSH	64.52	5.54	120	298	This work

Carbide derived carbon.

adsorbent. The second stage shows a plateau, indicating slow adsorption with intra-particle diffusion dominating during this stage. In addition, the c for both materials increased with temperature (from 1.21 to 2.21 mg/g for C–S–H and from 1.32 to 2.38 mg/g for Cry-CSH) implying improved adsorption process with increased mobility of the ions, from decreases in both of solution density and viscosity as temperature is increased (Almanassra et al., 2020).

3.3.6. Thermodynamic analysis

The activation energy (E_a) of phosphate adsorption was estimated for both C–S–H and Cry-CSH using equation (19) (Almanassra et al., 2020):

$$\ln k_2 = \ln k_0 - \frac{E_a}{RT} \qquad (19)$$

where E_a is the activation energy in kJ/mol, k_2 is the pseudo-second-order kinetic constant calculated from the kinetic data at each temperature, and k_0 is a factor independent of temperature. The E_a estimates of 47.5 and 43.9 kJ/mol were obtained for adsorption of phosphate on C–S–H and Cry-CSH, respectively. Since E_a is more than 40 kJ/mol, the adsorption mechanism on both materials is chemical adsorption (E_a < 40 kJ/mol for physical adsorption (Almanassra et al., 2020)).

The thermodynamic differences ΔG^0, ΔH^0, and ΔS^0 for phosphate adsorption on C–S–H and Cry-CSH are presented in Table 4. The negative values of ΔG^0 across the tested temperatures indicate spontaneous adsorption of phosphate on both materials under the experimental conditions, and more favorable adsorption at a higher temperature. The spontaneity of Cry-CSH seems to be higher than of C–S–H. The positive ΔH^0 indicates endothermic phosphate adsorption. ΔS^0 for both C–S–H and Cry-CSH were positive, indicating increased disorder at the solid–solution interface during the adsorption process, and the disorder degree on C–S–H seems to be higher than of Cry-CSH. The disordered state in both materials is mostly due to the interaction of phosphate with active sites of the adsorbents to form stable structures. These results demonstrate the strong affinity between phosphate and the prepared materials.

Table 4
Thermodynamic parameters for phosphate adsorption by C–S–H and Cry-CSH.

Temperature (K)	ΔG° (kJ/mol)		ΔH° (kJ/mol)		ΔS° (J/mol/K)	
	C–S–H	Cry-CSH	C–S–H	Cry-CSH	C–S–H	Cry-CSH
298	−5.22	−10.42	31.8	19.3	125.3	99.89
308	−7.33	−11.55				
318	−7.68	−12.42				

3.3.7. Influence of competing ions on removal efficiency of Cry-CSH

The influences of various co-exist anions, namely SO_4^{2-}, NO_3^-, NO_2^-, Br^-, F^-, and CO_3^{2-}, on removal efficiency of phosphate by Cry-CSH were investigated. Various competing anions (at 2000 mgL^{-1}) except for CO_3^{2-} were mixed with phosphate (50 mgL^{-1}) in order to determine the selectivity for phosphate. Carbonate (500 and 2000 mgL^{-1}), which has been reported to interfere with phosphate adsorption (Seliem et al., 2016; Zhang et al., 2019), was also mixed with phosphate but separately from the other anions. The removal efficiency of phosphate remained 99.17 ± 0.01% with mixed anions (S15) indicating excellent selectivity of Cry-CSH for phosphate, better than those of other adsorbents such as carbide derived carbon (Almanassra et al., 2020), or MCM-41 silica with rice husk (Seliem et al., 2016). The removal efficiency of phosphate slightly decreased to 95.35 ± 0.01% when concentration of CO_3^{2-} was 10-fold higher than that of phosphate (500 mgL^{-1}), but decreased to 55.02 ± 0.82% at 2000 mgL^{-1}. The results show that Cry-CSH is highly selective for phosphate ions and can be applied in phosphate removal and recovery.

3.4. Real sample application of Cry-CSH

The Cry-CSH was tested for phosphate removal from 2 wastewater and 3 effluent samples from the municipal treatment plant in Patong, Phuket. Orthophosphate presented in the samples in the range from 0.93 to 4.05 mgL^{-1} which exceed the concentration level of phosphate that is considered to cause eutrophication of water bodies (>0.02 mgL^{-1} (Seliem et al., 2016)). Concentrations from 0.005 to 0.014 mgL^{-1} were found after adsorption of phosphate using 2 g Cry-CSH, indicating removal efficiencies from 98.6% to 99.8% (Table 5). The chemical oxygen demand (COD) of the water after adsorption of phosphate using Cry-CSH was found to have increased 1.3 ± 0.7 fold, possibly due to the release of OH^- and Ca^{2+} from C–S–H (Ding et al., 2018; Zhang et al., 2019).

3.5. Biodegradation of Cry-CSH

Biodegradation of Cry-CSH and phosphate adsorbed on Cry-CSH was investigated using a soil burial test (Junlapong et al., 2020). After having been buried for three days, the Cry-CSH weight loss was 100%, while phosphate adsorbed Cry-CSH remained for 37.8 ± 1.2% by weight. The latter was completely lost after burial in the soil for 10 days, due to hydrolysis and microorganisms (Junlapong et al., 2020).

4. Conclusion

This work presented a novel calcium silicate hydrate composite cryogel (Cry-CSH) for phosphate removal and recovery. Cry-CSH had the C–S–H nanoparticles immobilized in a floatable monolithic cryogel network, resulting in much easier adsorbent recovery without loss. It can remove phosphate from wastewater and effluent samples with a high removal efficiency (>98%) and it can be further used directly used as a fertilizer in agriculture and will be biodegraded within 10 days when buried in soil. Thus, this work has demonstrated the significant potential of Cry-CSH for practical and environmentally friendly phosphate removal and recovery.

Credit author statement

Tarawee Taweekarn: Investigation, conceptualization, methodology, data curation, validation, formal analysis, visualization, writing- original draft preparation. Worawit Wongniramaikul: Funding acquisition, conceptualization, methodology, data curation, resources, formal analysis, writing-review and editing. Aree Choodum: Project administration, funding acquisition, conceptualization, methodology, validation, supervision, data curation, formal analysis, writing-original draft preparation, review, and editing.

Table 5
Real sample tests.

Sample	Type of sample	Before (mgL^{-1} PO_4^{3-})	After (mgL^{-1} PO_4^{3-})	%Removal efficiency
1[a]	Wastewater	4.05 ± 0.04	0.010 ± 0.004	99.8 ± 0.1
2	Wasterwater	1.01 ± 0.03	0.014 ± 0.004	98.6 ± 0.6
3[a]	Effluent	1.79 ± 0.12	0.005 ± 0.008	99.7 ± 0.4
4	Effluent	0.93 ± 0.02	0.009 ± 0.004	99.0 ± 0.4
5	Effluent	0.96 ± 0.01	0.009 ± 0.004	99.0 ± 0.4

[a] Samples were collected in December 2019 before Covid-19 pandemic, and there were ~14.4 M tourists that visited Phuket during that year.

Declaration of competing interest

The authors declare that they have no known competing financial interests or personal relationships that could have appeared to influence the work reported in this paper.

Appendix A. Supplementary data

Supplementary data to this article can be found online at https://doi.org/10.1016/j.jenvman.2021.113923.

References

Almanassra, I.W., Kochkodan, V., McKay, G., Atieh, M.A., Al-Ansari, T., 2021a. Review of phosphate removal from water by carbonaceous sorbents. J. Water Process. Eng. 287, 112245. https://doi.org/10.1016/j.jenvman.2021.112245.

Almanassra, I.W., Kochkodan, V., Subeh, M., McKay, G., Atieh, M., Al-Ansari, T., 2020. Phosphate removal from synthetic and treated sewage effluent by carbide derive carbon. J. Water Process. Eng. 36, 101323. https://doi.org/10.1016/j.jwpe.2020.101323.

Almanassra, I.W., McKay, G., Kochkodan, V., Ali Atieh, M., Al-Ansari, T., 2021b. A state of the art review on phosphate removal from water by biochars. Chem. Eng. J. 409, 128211. https://doi.org/10.1016/j.cej.2020.128211.

APHA-AWWA-WEF, 1998. Ascorbic acid method. In: Standard Method for the Examination of Water and Wastewater, nth ed. American. Public Health Association, Washington DC.

Baudron, V., Gurikov, P., Smirnova, I., Whitehouse, S., 2019. Porous starch materials via supercritical- and freeze-drying. Gels 5. https://doi.org/10.3390/gels5010012.

Boonkanon, C., Phatthanawiwat, K., Wongniramaikul, W., vChoodum, A., 2020. Curcumin nanoparticle doped starch thin film as a green colorimetric sensor for detection of boron. Spectrochim. Acta Mol. Biomol. Spectrosc. 224 https://doi.org/10.1016/j.saa.2019.117351, 117351-117351.

Bryant, C.M., Hamaker, B.R., 1997. Effect of lime on gelatinization of corn flour and starch. Cereal Chem. 74, 171–175. https://doi.org/10.1094/CCHEM.1997.74.2.171.

Chanjarujit, W., Hongsprabhas, P., Chaiseri, S., 2018. Physicochemical properties and flavor retention ability of alkaline calcium hydroxide-mungbean starch films. Carbohydr. Polym. 198, 473–480. https://doi.org/10.1016/j.carbpol.2018.06.118.

Choodum, A., Kanatharana, P., Wongniramaikul, W., NicDaeid, N., 2016. Poly vinyl alcohol cryogel as a selective test kit for pre and post blast trinitrotoluene. Sensor. Actuator. B Chem. 222, 654–662. https://doi.org/10.1016/j.snb.2015.08.115.

Choodum, A., Sriprom, W., Wongniramaikul, W., 2019. Portable and selective colorimetric film and digital image colorimetry for detection of iron. Spectrochim. Acta Mol. Biomol. Spectrosc. 208, 40–47. https://doi.org/10.1016/j.saa.2018.09.062.

Cornejo-Villegas, M.d.l.Á., Rincón-Londoño, N., Del Real-López, A., Rodríguez-García, M. E., 2018. The effect of Ca2+ ions on the pasting, morphological, structural, vibrational, and mechanical properties of corn starch–water system. J. Cereal. Sci. 79, 174–182. https://doi.org/10.1016/j.jcs.2017.10.003.

Dai, M., 1994. The effect of zeta potential of activated carbon on the adsorption of dyes from aqueous solution: I. The adsorption of cationic dyes: methyl green and methyl violet. J. Colloid Interface Sci. 164, 223–228. https://doi.org/10.1006/jcis.1994.1160.

Ding, S., Fang, D., Pang, Z., Luo, B., Kuang, L., Wang, H., Zhang, Q., Shen, Q., Ji, F., 2018. Immobilization of powdery calcium silicate hydrate via PVA covalent cross-linking

process for phosphorus removal. Sci. Total Environ. 645, 937–945. https://doi.org/10.1016/j.scitotenv.2018.07.197.

Domene-López, D., García-Quesada, J.C., Martin-Gullon, I., Montalbán, M.G., 2019. Influence of starch composition and molecular weight on physicochemical properties of biodegradable films. Polymers 11, 1084. https://doi.org/10.3390/polym11071084.

Franceschini, A., Abramson, S., Mancini, V., Bresson, B., Chassenieux, C., Lequeux, N., 2007. New covalent bonded polymer–calcium silicate hydrate composites. J. Mater. Chem. 17, 913–922. https://doi.org/10.1039/B613077A.

García-Lodeiro, I., Fernández-Jiménez, A., Blanco, M.T., Palomo, A., 2008. FTIR study of the sol–gel synthesis of cementitious gels: C–S–H and N–A–S–H. J. Sol. Gel Sci. Technol. 45, 63–72. https://doi.org/10.1007/s10971-007-1643-6.

Guan, W., Ji, F., Chen, Q., Yan, P., Zhang, Q., 2013. Preparation and phosphorus recovery performance of porous calcium–silicate–hydrate. Ceram. Int. 39, 1385–1391. https://doi.org/10.1016/j.ceramint.2012.07.079.

Ho, Y.-S., 2006. Review of second-order models for adsorption systems. J. Hazard Mater. 136, 681–689. https://doi.org/10.1016/j.jhazmat.2005.12.043.

Huong, P.T., Jitae, K., Giang, B.L., Nguyen, T.D., Thang, P.Q., 2019. Novel lanthanum-modified activated carbon derived from pine cone biomass as ecofriendly bio-sorbent for removal of phosphate and nitrate in wastewater. Rendiconti Lincei. Sci. Fis. Nat. 30, 637–647. https://doi.org/10.1007/s12210-019-00827-3.

Jun, B.-M., Cho, J., Jang, A., Chon, K., Westerhoff, P., Yoon, Y., Rho, H., 2020. Charge characteristics (surface charge vs. zeta potential) of membrane surfaces to assess the salt rejection behavior of nanofiltration membranes. Separ. Purif. Technol. 247, 117026. https://doi.org/10.1016/j.seppur.2020.117026.

Junlapong, K., Maijan, P., Chaibundit, C., Chantarak, S., 2020. Effective adsorption of methylene blue by biodegradable superabsorbent cassava starch-based hydrogel. Int. J. Biol. Macromol. 158, 258–264. https://doi.org/10.1016/j.ijbiomac.2020.04.247.

Khormaei, M., Nasernejad, B., Edrisi, M., Eslamzadeh, T., 2007. Copper biosorption from aqueous solutions by sour orange residue. J. Hazard Mater. 149, 269–274. https://doi.org/10.1016/j.jhazmat.2007.03.074.

Langmuir, I., 1918. The Adsorption of gases on plane durfaces of glass, mica and platinum. J. Am. Chem. Soc. 40, 1361–1403. https://doi.org/10.1021/ja02242a004.

Lee, C.-G., Alvarez, P.J.J., Kim, H.-G., Jeong, S., Lee, S., Lee, K.B., Lee, S.-H., Choi, J.-W., 2018. Phosphorous recovery from sewage sludge using calcium silicate hydrates. Chemosphere 193, 1087–1093. https://doi.org/10.1016/j.chemosphere.2017.11.129.

Liu, S., 2015. Cooperative adsorption on solid surfaces. J. Colloid Interface Sci. 450, 224–238. https://doi.org/10.1016/j.jcis.2015.03.013.

Lozinsky, V., 2008. Polymeric cryogels as a new family of macroporous and supermacroporous materials for biotechnological purposes. Russ. Chem. Bull. 57, 1015–1032. https://doi.org/10.1007/s11172-008-0131-7.

Madaeni, S.S., Salehi, E., 2009. Adsorption of cations on nanofiltration membrane: separation mechanism, isotherm confirmation and thermodynamic analysis. Chem. Eng. J. 150, 114–121. https://doi.org/10.1016/j.cej.2008.12.005.

Maeda, H., Yokota, S., Kasuga, T., 2018. Structural changes in calcium silicate hydrate gel and resulting improvement in phosphate species removal properties after mechanochemical treatment. R. Soc. Open Sci. 5, 181403. https://doi.org/10.1098/rsos.181403.

Mattiasson, B., Kumar, A., Galeaev, I.Y. (Eds.), 2009. Macroporous Polymers: Production Properties and Biotechnological/Biomedical Applications, first ed. CRC Press.

Mezenner, N.Y., Bensmaili, A., 2009. Kinetics and thermodynamic study of phosphate adsorption on iron hydroxide-eggshell waste. Chem. Eng. J. 147, 87–96. https://doi.org/10.1016/j.cej.2008.06.024.

Okano, K., Miyamaru, S., Kitao, A., Takano, H., Aketo, T., Toda, M., Honda, K., Ohtake, H., 2015. Amorphous calcium silicate hydrates and their possible mechanism for recovering phosphate from wastewater. Separ. Purif. Technol. 144, 63–69. https://doi.org/10.1016/j.seppur.2015.01.043.

Okano, K., Miyamaru, S., Yamamoto, Y., Kunisada, M., Takano, H., Toda, M., Honda, K., Ohtake, H., 2016. A mobile pilot-scale plant for in situ demonstration of phosphorus recovery from wastewater using amorphous calcium silicate hydrates. Separ. Purif. Technol. 170, 116–121. https://doi.org/10.1016/j.seppur.2016.06.040.

Okano, K., Uemoto, M., Kagami, J., Miura, K., Aketo, T., Toda, M., Honda, K., Ohtake, H., 2013. Novel technique for phosphorus recovery from aqueous solutions using amorphous calcium silicate hydrates (A-CSHs). Water Res. 47, 2251–2259. https://doi.org/10.1016/j.watres.2013.01.052.

Pavan, F.A., Camacho, E.S., Lima, E.C., Dotto, G.L., Branco, V.T.A., Dias, S.L.P., 2014. Formosa papaya seed powder (FPSP): preparation, characterization and application as an alternative adsorbent for the removal of crystal violet from aqueous phase. J. Environ. Chem. Eng. 2, 230–238. https://doi.org/10.1016/j.jece.2013.12.017.

Peng, L., Dai, H., Wu, Y., Dai, Z., Li, X., Lu, X., 2018. Performance and adsorption mechanism of a magnetic calcium silicate hydrate composite for phosphate removal and recovery. Water Sci. Technol. 578–591. https://doi.org/10.2166/wst.2018.184, 2017.

Pineda-Gómez, P., Rosales-Rivera, A., Rodríguez-García, M.E., 2012. Effect of the thermo-alkaline treatment over the thermal degradation of corn starch. Stärke 64, 776–785. https://doi.org/10.1002/star.201200015.

Qi, L., Tang, X., Wang, Z., Peng, X., 2017. Pore characterization of different types of coal from coal and gas outburst disaster sites using low temperature nitrogen adsorption approach. Int J Min Sci Technol 27, 371–377. https://doi.org/10.1016/j.ijmst.2017.01.005.

Seliem, M.K., Komarneni, S., Abu Khadra, M.R., 2016. Phosphate removal from solution by composite of MCM-41 silica with rice husk: kinetic and equilibrium studies. Microporous Mesoporous Mater. 224, 51–57. https://doi.org/10.1016/j.micromeso.2015.11.011.

Sen Gupta, S., Bhattacharyya, K.G., 2011. Kinetics of adsorption of metal ions on inorganic materials: a review. Adv. Colloid Interface Sci. 162, 39–58. https://doi.org/10.1016/j.cis.2010.12.004.

Thommes, M., Kaneko, K., Neimark, A.V., Olivier, J.P., Rodríguez-Reinoso, F., Rouquerol, J., Sing, K.S.W., 2015. Physisorption of gases, with special reference to the evaluation of surface area and pore size distribution (IUPAC Technical Report). Pure Appl. Chem. 87, 1051–1069. https://doi.org/10.1515/pac-2014-1117.

Torit, J., Phihusut, D., 2019. Phosphorus removal from wastewater using eggshell ash. Environ. Sci. Pollut. Res. 26, 34101–34109. https://doi.org/10.1007/s11356-018-3305-3.

Wongniramaikul, W., Limsakul, W., Choodum, A., 2018. A biodegradable colorimetric film for rapid low-cost field determination of formaldehyde contamination by digital image colorimetry. Food Chem. 249, 154–161. https://doi.org/10.1016/j.foodchem.2018.01.021.

Yu, P., Kirkpatrick, R., Poe, B., McMillan, P., Cong, X., 2004. Structure of calcium silicate hydrate (C-S-H): near-, mid-, and far-infrared spectroscopy. J. Am. Ceram. Soc. 82, 742–748. https://doi.org/10.1111/j.1151-2916.1999.tb01826.x.

Yuh-Shan, H., 2004. Citation review of Lagergren kinetic rate equation on adsorption reactions. Scientometrics 59, 171–177. https://doi.org/10.1023/B:SCIE.0000013305.99473.cf.

Zhang, Z., Wang, X., Zhao, J., 2019. Phosphate recovery from wastewater using calcium silicate hydrate (C-S-H): sonochemical synthesis and properties. Environ. Sci. Water Res. Technol. 5, 131–139. https://doi.org/10.1039/C8EW00643A.

VITAE

Name   Miss Tarawee Taweekarn

Student ID   6030231001

Education Attainment

Degree	Name of Institute	Year of Graduation
Bachelor of Science (Chemistry-Biology)	Prince of Songkla University	2011
Master of Science (Environmental management)	Prince of Songkla University	2015

Scholarship Awards during Enrolment

1. Research assistant from Prince of Songkla University through PSU research funds.
2. Graduate School research support, Prince of Songkla University
3. Research fund for graduate study from Faculty of Technology and Environment, Prince of Songkla University, Phuket Campus.
4. Partial research support from the National Research Council of Thailand (NRCT) through the research grant no. NRCT5–RSA63022–05

List of Publications

Taweekarn, T., Wongniramaikul, W., and Choodum, A. 2022. Removal and recovery of phosphate using a novel calcium silicate hydrate composite starch cryogel. Journal of Environmental Management 301, 113923.

Taweekarn, T., Wongniramaikul, W., Limsakul, W., Sriprom, W., Phawachalotorn C., and Choodum, A. 2020. A novel colorimetric sensor based on modified mesoporous silica. Microchimica Acta 187, 643.

Boonkanon, C., Phatthanawiwat, K., Chuenchom, L., Lamthornkit, N., **Taweekarn, T.,** Wongniramaikul, W., and Choodum, A. 2021. Preparation and characterization of calcium cross–linked starch monolithic cryogel and their application as a cost–effective green filters. Polymers 13, 3975.

Choodum, A., Lamthornkit, N., Boonkanon, C., **Taweekarn, T.,** Phatthanawiwat, K., Sriprom, W., Limsakul, W., Chuenchom, L., and Wongniramaikul, W. 2021. Greener monolithic solid phase extraction biosorbent based on calcium cross–linked starch cryogel composite grapheme oxide nanoparticles for benzo(a)pyrene analysis. Molecules 26, 6163.

Choodum, A., Tiengtum, J., **Taweekarn, T.,** and Wongniramaikul, W. 2020. Convenient environmentally friendly on–site quantitative analysis of nitrite and nitrate in seawater based on polymeric test kits and smartphone application. Spectrochimica Acta Part A: Molecular and Biomolecular Spectroscopy 243, 118812.

Choodum, A., Jirapattanasophon, V., Boonkanon, C., **Taweekarn, T.,** and Wongniramaikul, W. 2020. Difluoroboron-Curcumin Doped Starch Film and Digital Image Colorimetry for Semi-Quantitative Analysis of Arsenic. Analytical Sciences 36, 577-582.

Patents

Petty patent entitled "The process of preparing the nitrite test kit" by Assoc. Prof. Dr. Aree choodum, Ms. Tarawee Taweekarn, Assoc. Prof. Dr. Worawit Wongniramaikul